

(1)

ANNUAL REPORT  
University Research Initiative  
Contract No.: N00014-92-J-1808  
March 1993 - April 1994

AD-A279 814



TH DTIC  
S ELECTE  
G MAY 27 1994 D

---

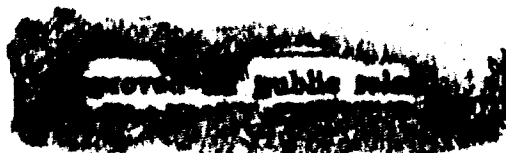
The Processing and Mechanical  
Properties of High Temperature/  
High Performance Composites

by

A.G. Evans & F. Leckie  
University of California,  
Santa Barbara

University of Pennsylvania  
Harvard University  
Washington State University  
Carnegie Mellon University  
University of Virginia

0411591  
166G1



DTIC QUALITY INSPECTED 1

Book 7 of 7:

In-Situ Measurements of Stress and Damage

**SUMMARY**

**OF**

**TABLE OF CONTENTS**

**EXECUTIVE SUMMARY**

Accession For	
NTIS	CRA&I
DTIC	TAB
Unannounced	
Justification	
By _____	
Distribution / _____	
Availability Codes	
Dist	Avail and/or Special
A-1	

**BOOK 1: MECHANISM-BASED CONSTITUTIVE LAWS AND DESIGN**

**BOOK 2: STRESS REDISTRIBUTION AND NOTCH PROPERTIES**

**BOOK 3: FATIGUE AND CREEP**

**BOOK 4: PROCESSING/PROPERTY CORRELATIONS**

**BOOK 5: INTERFACE EFFECTS**

**BOOK 6: DELAMINATION AND COMPRESSIVE BEHAVIOR**

**BOOK 7: IN-SETUP MEASUREMENTS OF STRESS AND DAMAGE**



KJS 4/27/84

**BOOK 7**

**IN-SITU MEASUREMENTS OF STRESS AND DAMAGE**

- |     |   |   |
|-----|---|---|
| 82. | <b>Residual Stress Measurement in Sapphire Fiber Composites: Through-Focus and Transmission Fluorescence Spectroscopy</b> | D. Lipkin<br>D. R. Clarke                                 |
| 83. | <b>Measurement of Residual Stresses in Sapphire Fiber Composites Using Optical Fluorescence</b>                           | Q. Ma<br>D. R. Clarke                                     |
| 84. | <b>Luminescence Sensing of Stress in Ti/Al<sub>2</sub>O<sub>3</sub> Fiber Reinforced Composites</b>                       | H. Hough<br>M. Demas<br>T. O. Williams<br>H. N. G. Wadley |
| 85. | <b>Optical Fluorescence from Chromium Ions in Sapphire: A Probe of the Image Stress</b>                                   | Q. Ma<br>D. Clarke  |
| 86. | <b>Residual Stresses in Al<sub>2</sub>O<sub>3</sub>-ZrO<sub>2</sub> Composites: A Test of Stochastic Stress Models</b>    | Q. Ma<br>W. Pompe<br>D. R. Clarke                         |
| 87. | <b>Stress Measurement Using Optical Fluorescence</b>  | Q. Ma<br>D. Clarke  |

KJB 4/27/94

## EXECUTIVE SUMMARY

The general emphasis for 1994 would be on increased software development, testing of subelements and design calculations. For these purposes, the constitutive law coding and development would be coordinated by Nick Aravas, and implemented in ABAQUS. The initial implementation would be the elastic/plastic model for MMCs with interface debonding developed in 1993 (Leckie). This would be extended in 1994 to include creep and some aspects of thermomechanical cycling. The code would be used for design calculations concerned with MMC rotors, actuators and vanes (Leckie). A plan is being formulated to collaborate with Pratt and Whitney to acquire MMC sub-elements representative of these components during 1994. Experimental tests on these subelements would be capable of providing a direct validation of the code capabilities.

Constitutive law and fatigue life software would be created for CMCs using continuum damage mechanics (CDM) approaches (Leckie, McMeeking). The approach has been motivated by micromechanics models developed in 1993 (Hutchinson, Zok, Evans). These codes would be used to calculate stress redistribution effects and fatigue life on simple sub-elements, such as center notched and pin-loaded plates. Comparison with experimental measurements needed to test the fidelity of the models will be based on moiré interferometry and thermoelastic emission. This effort is coordinated with the NASA EPM program through both General Electric and Pratt and Whitney. A plan for acquiring sub-elements from DuPont Lanxide is being formulated.

A new emphasis for 1994 would be on the transverse properties of CMCs. The measurements and calculations performed in 1993 have indicated a strategy for curved sections and junctions that would establish a consistent design approach. The basic approach for resisting failures from combinations of interlaminar shear and transverse tension involves the use of stitching and angle ply weaving patterns that inhibit major reductions in stiffness when matrix cracks are induced by transverse loads and bending moments. For this purpose, calculations would be performed that combine

the mechanics of delamination cracks with models of bridging by inclined fiber bundles (Hutchinson, Ashby, Evans, McMeeking). The insight gained from these calculations would be used to design and acquire sub-elements, such as C sections and T junctions.

Additional software development will be for creep and creep rupture (McMeeking). The models devised in 1993 and test data relevant to MMCs will be combined into a code that predicts the creep and rupture of unidirectional MMCs subject to multiaxial loads. Some aspects of this code will also be applicable to CMCs.

Two new activities will be introduced in 1994: thermal properties and damping. The thermal properties will be studied on both CMCs and MMCs (Ashby, Hutchinson). Measurements of thermal diffusivity will be made by the laser flash method and related to the properties of the interface and the density of matrix damage in the material. Thermal expansion measurements will also be performed with emphasis on determining hysteresis effects, which can be related to the temperature dependence of the interfaces properties, through cell models. The latter might evolve into a diagnostic for establishing relationships between the interface properties and thermomechanical fatigue.

The processing activities in the program will have newly established goals in 1994. The principal emphasis will be on concepts for affordable manufacturing. The issues selected for investigation will be consistent with manufacturing processes that allow near-net shape consolidation while still yielding reasonable combinations of longitudinal and transverse properties. Performance models developed in the program would be used as an initial test of concept viability.

Beyond these general trends, specific activities are planned for 1994. These are elaborated below. The status of understanding and development in each of these areas is summarized in Table I. Increasing magnitudes between 0 and 1 designate a knowledge range from limited to comprehensive.

**TABLE 1A****Status of Design Knowledge for MMCs**

	[0°] <sub>n</sub> MMC				[0°/90°] <sub>n</sub>	
	LONG.		TRANS.		P            S	
	P	S	P	S		
Tensile Strength	3/4	1	1	1/2	1/4	~ 0
Creep and Creep Rupture	3/4	0	1	0	0	0
Cyclic Flow (Isothermal, TMF)	1/4	0	1	1/2	0	0
Crack Growth (Isothermal Fatigue)	1	1	0	1/2	0	0
Crack Growth (TMF)	1/2	1/2	0	0	0	0
Compressive Strength	3/4	0	0	0	0	0

**TABLE 1B****Status of Design Knowledge for CMCs**

	[0/90]		[45/45]	
	P	S	P	S
Stress/Strain	3/4	1/4	1/2	0
Fatigue	3/4	0	0	0
TMF	1/4	0	0	0
Creep and Rupture	1/2	0	0	0
Compression Strength	3/4	1/4	0	0
Transverse Properties	3/4	1/2	—	—
Thermal Properties	1/4	0	—	—

**P      Primary Structure**

**S      Secondary Structure**

## 2. CONSTITUTIVE LAWS

Two approaches will be used to create a formulation capable of representing the in-plane properties of CMCs. One would be based on Continuum Damage Mechanics (CDM) (Leckie). The other would use concepts analogous to those used in plasticity theory (Hutchinson). The CDM approach uses damage parameters that relate explicitly to micromechanics models. A potential function has already been identified as the state variable which separately represents the strain from the elastic compliance change caused by the matrix cracks and the inelastic strains associated with the debonding and sliding interfaces. Derivatives of the potential with regard to strain and damage give the relationships between variables, such as stress, interface sliding resistance, matrix crack density, etc.

The first version of the CDM model would use the minimum number of damage variables potentially capable of representing the behavior of laminated or woven composites. Cross terms between the damage variables would not be considered at this stage. Moreover, matrix cracks would be introduced normal to the maximum principal tensile stress, consistent with the experimental observations.

The plasticity theory approach would seek a formulation based on matrix cracks occurring normal to the maximum principal tension. It would introduce parameters that reflect the inelastic strain caused by interface sliding upon off-axis loading which would be calibrated from tests performed in tension in 0/90 and 45/45 orientations.

The insight needed to characterize off-axis loading effects will be gained from cell models (Hutchinson) in a manner analogous to that previously used for axial loads. The principal objective will be to understand trends in matrix crack opening and interface debonding/sliding with applied loads. The stress on the fibers will be calculated with the intent of predicting effects of loading orientation on fiber failure. The models will be compared with measurements made in 45/45 tension, using various CMCs (Evans).

Calibration of the damage parameters for each material would be made from hysteresis loop measurements in accordance with procedures developed in 1993. Experimental results obtained in 0/90 tension, 45/45

tension and in-plane shear will be used. In future work, it is hoped that shear tests will not be necessary.

The validation of the constitutive laws will be achieved by comparing calculations with measurements made on sub-elements, especially pin-loaded holes (Evans). The experimental results include residual strains obtained by Moiré interferometry (Fig. 2.1), ultimate loads for either tensile or shear failure and principal strain trajectories delineated by matrix cracking patterns. Acoustic methods will also be developed to probe the local values of the elastic modulus (Clarke, Wadley) which could be compared directly with the CDM predictions.

### 3. FATIGUE LIFING

#### 3.1 CMCs

A software program for isothermal low cycle fatigue (LCF) of CMCs, developed in 1993 (Fig. 3.1) will be extended in 1994. The present program asserts that fatigue is associated with cyclic degradation of the interface sliding resistance,  $\tau$ , which can be characterized by analyzing hysteresis loops measured periodically during a fatigue test. With this methodology, S-N curves have been predicted for both unidirectional and woven 0/90 composites tested in cyclic tension as well as changes in compliance and permanent strain. Some additional effort is required to analyze data on 0/90 laminates in order to validate the model predictions. The extensions envisaged for 1994 include thermomechanical fatigue (TMF), strain controlled LCF and off-axis fatigue (Zok, Evans). Experiments are planned which would assess the effects of temperature cycling and of inclined fibers on  $\tau$  degradation, measured from hysteresis loops. Various cell model calculations (Hutchinson) will be used to interpret the experiments. The results will be used to establish general rules for interface degradation in CMCs.

The off-axis experiments will also give insight into the fiber failure criterion that replaces the global load sharing (GLS) results successfully used for 0/90 loadings. This study will coordinate with the cell calculations described above, and the 45/45 tensile experiments.

Notch fatigue studies will be initiated. These will examine cyclic stress redistribution and notch sensitivity (Evans).

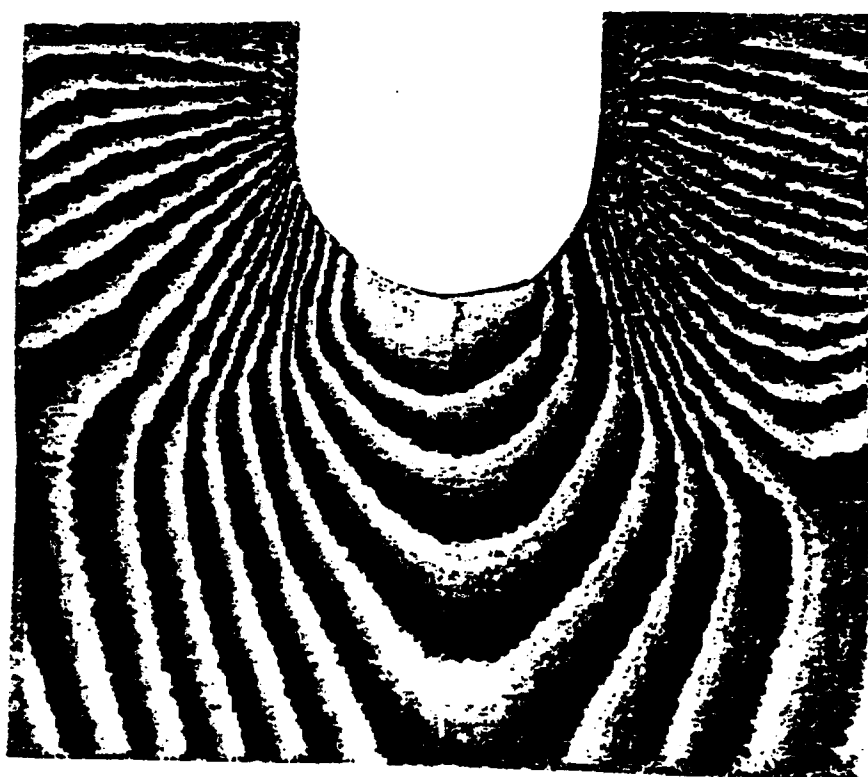
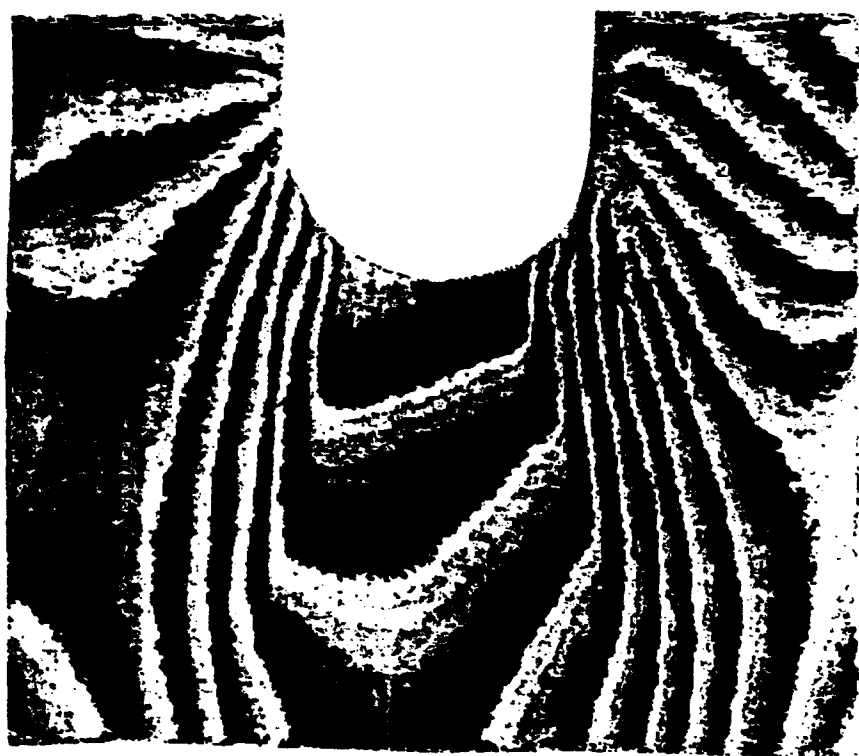


Figure 2.1

# Fatigue Methodology

## CMC Life Program

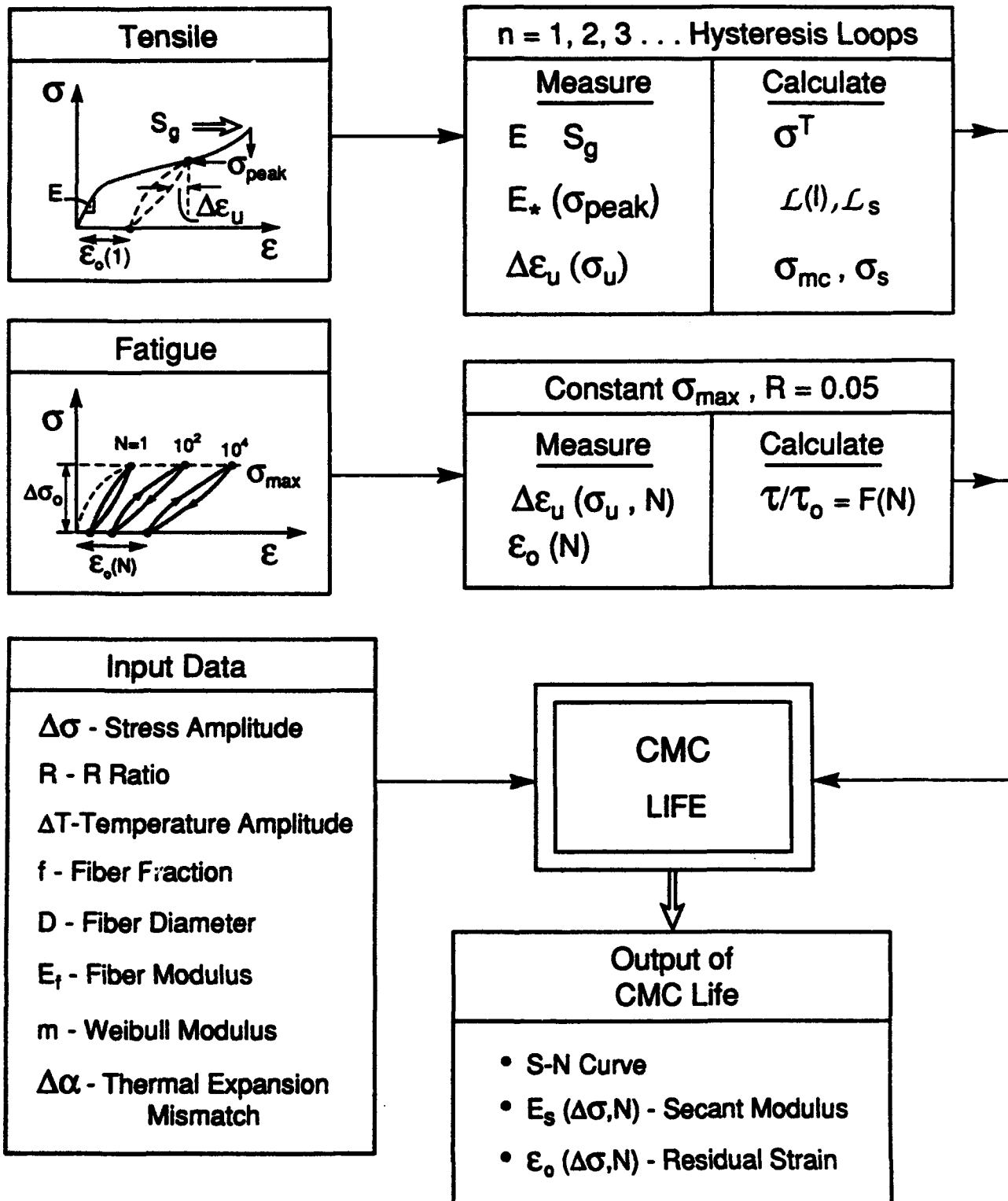


Figure 3.1

### **3.2 MMCs**

Fatigue crack growth and notch strength studies in MMCs will be extended to 0/90 laminates (Zok, Suo). The experiments concerned with crack growth will be interpreted using crack bridging models. The utility of such models has been validated in previous years through studies on unidirectional MMCs. It is envisaged that the fatigue crack growth characteristics of the unidirectional and 0/90 configurations will be related through the volume fraction of fibers aligned with the loading direction. The notch strength behavior will also be interpreted using crack bridging models. Such models have been developed in 1993 and found to be useful in rationalizing the behavior of unidirectional materials (Zok, Suo). In all cases, the mechanical measurements will be augmented by *in-situ* observations to identify changes in damage mechanisms with temperature, fiber architecture, etc. Plans to study the influence of panel thickness on fatigue and fracture resistance are also being developed, as well as tests to understand the potential for crack growth in mixed mode loadings (Hirth, Zok).

Studies of the TMF response of MMCs loaded parallel to the fiber axis will be initiated (Zok, Leckie). Experiments will evaluate both in-phase and out-of-phase loadings. Models of load shedding (matrix-fibers) will be used to interpret the hysteresis loops and to develop fatigue life models applicable to low cycle, high strain TMF.

## **4. CREEP AND RUPTURE**

### **4.1 MMCs**

The considerable progress made in 1993 towards identifying and understanding the mechanisms of creep and rupture in unidirectional MMCs containing non-creeping fibers (McMeeking, Zok) will be used to develop creep rupture software. The longitudinal creep model to be used incorporates stochastic fiber fracture and interface sliding in a format amenable to the prediction of primary and tertiary creep in terms of matrix creep strength, interface sliding resistance, fiber strength, Weibull modulus, etc. The concepts would be visualized in a rupture mechanisms map

(Fig. 4.1). The transverse creep behavior would include interface debonding, which greatly accelerates the creep, leading to marked anisotropy. A constitutive law for creep that includes these effects will be developed (Aravas, McMeeking).

Additional experiments and calculations will be conducted to assess the effects of notches and holes on creep rupture (Zok, Suo). Experience with MMCs at ambient temperature indicates that the notch sensitivity is largely dictated by matrix properties (i.e., strength and ductility). The reduction in matrix properties at elevated temperatures may lead to a substantial elevation in notch sensitivity. However, this behavior may be complicated by the development of alternate damage processes, such as shear bands.

#### 4.2 CMCs

Studies of the creep and rupture of CMCs will continue with emphasis on materials containing creeping fibers. A particular emphasis will be on matrix cracking that arises as fiber creep relaxes fiber bridging tractions (McMeeking, Evans). The experimental studies will be performed on SiC/SiC composites. Hysteresis loop measurements will be used to monitor matrix damage during composite creep, using procedures devised in 1993. Models will be developed based on time dependent fiber bridging concepts (McMeeking, Cox).

It is envisioned that the lifetime of some CMCs will be dictated by time-dependent rupture of the fibers. A lifetime prediction tool for such a composite *must* incorporate the knowledge of fiber strength degradation over time. A new activity will be initiated to address this problem (Suo, Evans). The initial work will involve a survey of data in the existing literature, and a comparison with available models. A new model is being developed for single crystal fibers. This model involves a residual pore inside a fiber which changes shape, under stress, via surface diffusion, to become a crack. These issues will be viewed in the broad context of fiber and composite manufacture.

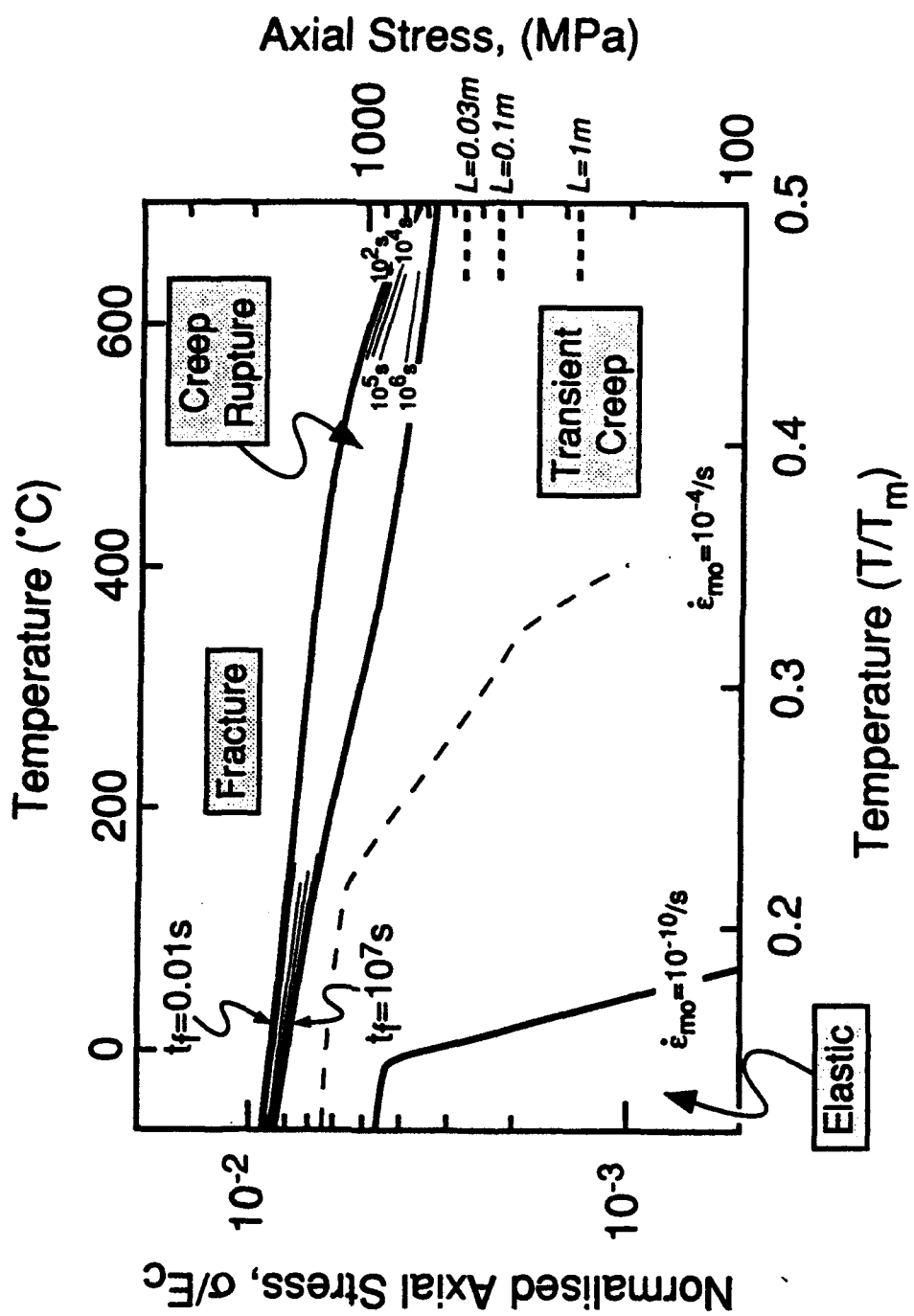


Figure 4.1

## 5. TRANSVERSE PERFORMANCE OF CMCs

Analyses and tests performed in 1993 (Ashby, Hutchinson, Bao) have highlighted the essential issues related to components that experience combinations of transverse tension and interlaminar shear. In both loadings, matrix cracks form at manufacturing flaws at low stresses, of order 10-100 MPa. These cracks extend across the plies and interact minimally with the fibers. Although the crack configurations differ for transverse tension and interlaminar shear loadings, multiple cracks always form. This multiplicity of cracking causes a major reduction in stiffness, which can cause unacceptably large displacements and also redistribute stress into other areas. The formation of the matrix cracks is probabilistic in nature and governed by the size distribution of manufacturing flaws. Design based on the prevention of such transverse cracks must rely on weakest link statistics, usually with a low Weibull modulus. Alternatively, it may be assumed that cracks *inevitably* form and, instead, reliance is placed on controlling the diminished modulus of the material, after matrix cracking has occurred. This approach relies on having 3-D architectures, with transverse fibers introduced locally either by stitching or by using angle plies. To explore this possibility, calculations will be performed (Hutchinson, Evans) to examine fiber architectures that lead to minimum stiffness loss, subject to acceptable in-plane properties. Based on these calculations, sub-elements will be designed that test out the concepts.

## 6. COMPRESSIVE BEHAVIOR

The studies completed in 1993 on the compressive failure of polymer matrix composites by the growth of kink bands (Budiansky, Fleck) will be extended to metal matrix composites, through a coordination with 3M. Compressive failure of Al and Ti MMCs with small diameter fibers has been observed by 3M to occur in accordance with the same kink band mechanism known to operate in PMCs and in C/C composites. The theory should thus extend to the MMCs, with the fiber misalignment, the shear yield strength of the matrix and its work hardening coefficient as the principal variables. A comparison between the theory and experimental

results would provide the basis for specifying the compressive properties of MMCs.

Compression failure of CMCs occurs by different mechanisms (Ashby). The dominant failure modes are similar to those that operate in porous brittle solids such as monolithic ceramics, concrete and rocks. The theory is well established and validated for these materials. Applications of the theory to various CMCs will be made and applied to the understanding of a behavior of pin-loaded holes (Evans, Ashby).

## 7. THERMAL PROPERTIES

A new focus on the thermal properties of CMCs and MMCs will be initiated in 1994. Calculations of the effects of matrix cracks in the thermal expansion of CMCs will be made (Hutchinson). These will be compared with data obtained from TMF testing (Zok). The effects of such cracks on the in-plane thermal conductivity will also be calculated (Hutchinson). Measurements will be performed using the laser flash method (Ashby).

Thermal conductivity measurements will be initiated on Ti MMCs (Ashby). These will be used to understand the effects of the fiber/matrix interphases and of matrix damage on the transverse and in-plane thermal conduction.

## 8. MATERIALS SELECTION

The Cambridge Materials Selector software will be expanded in 1994 to include high temperature creep design with the corresponding data base (Ashby). This expanded version will permit estimates to be made of temperature limits for MMCs based on creep controlled TMF and on the transverse creep of components with unidirectional reinforcements.

## 9. DESIGN CALCULATIONS AND SUB-ELEMENT TESTS

A larger fraction of the effort in 1994 will be on design and sub-element testing, particularly for MMCs. Discussions are now in progress with Pratt and Whitney, Textron and 3M to perform design calculations using the

constitutive equations developed at UCSB and to produce sub-elements for testing.

The design emphasis for MMCs will be on various diffusion bonded joints with Ti matrices and monolithic Ti attachments. Two specific subelements are envisaged. The first involves unidirectionally reinforced rods (or plates), clad with monolithic metal. The purpose of the cladding is to prevent exposure of the fibers to the environment and to mechanical abrasion. The design of clad MMC structures requires consideration of (i) the residual stresses resulting from thermal mismatch between the cladding and the composites section, (ii) the potential for fatigue cracks to initiate and grow through the monolithic material, and (iii) the interaction of such cracks with the composite section and their influence on the strength and life of the structure. The design and testing of such subelements (Zok, Leckie) will be augmented by calculations of crack growth and fracture, incorporating the effects of thermal and elastic mismatch between the cladding and the composite (McMeeking). The clad structures will also be used to initiate studies on the reinforcement of holes in composite sections with monolithic metal patches, as drawn in Fig. 9.1 (Zok, Suo). The second subelement involves the attachment of a MMC actuator rod to a pin-loaded monolithic section (Fig. 9.2). The critical design issues relate to the strength and fatigue resistance of the interfaces between the composite and monolithic matrices. Design studies shall also be completed on rotor rings with special efforts made to produce rule-based design procedures which would be used by industry at the conceptual level of design to determine sizes and the efficient disposition of material.

For CMCs, the sub-element studies would be based on the calculations described above in Section 5. These would include C sections and T junctions (Fig. 9.3) Negotiations for manufacturing these sub-elements will be initiated and tests performed at UCSB.

## 10. AFFORDABLE MANUFACTURING

As our understanding of composite mechanics and its interplay with design and performance has evolved, it has become increasingly evident that cost and reproducibility, are major constraints. Even as processing

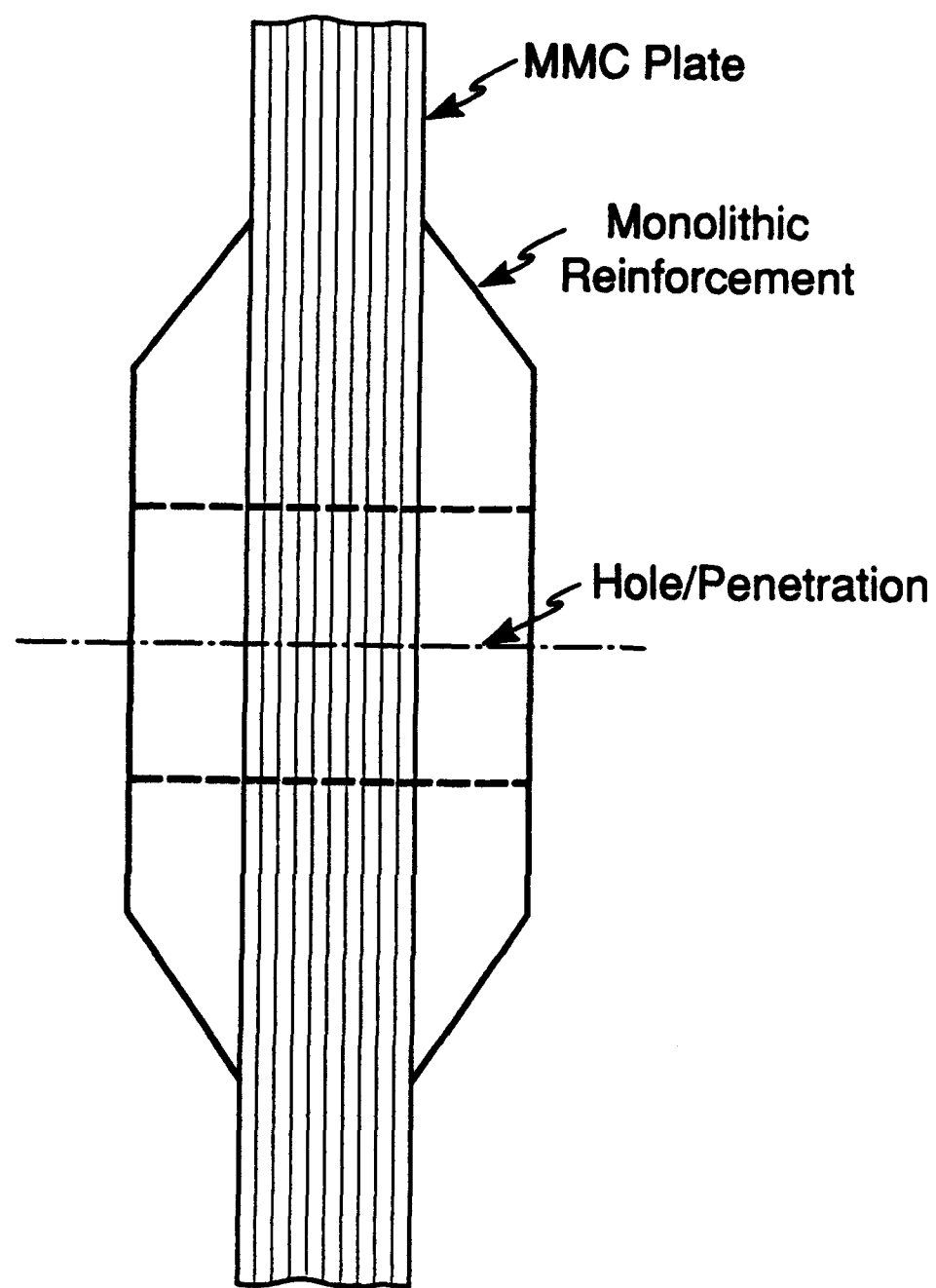


Figure 9.1

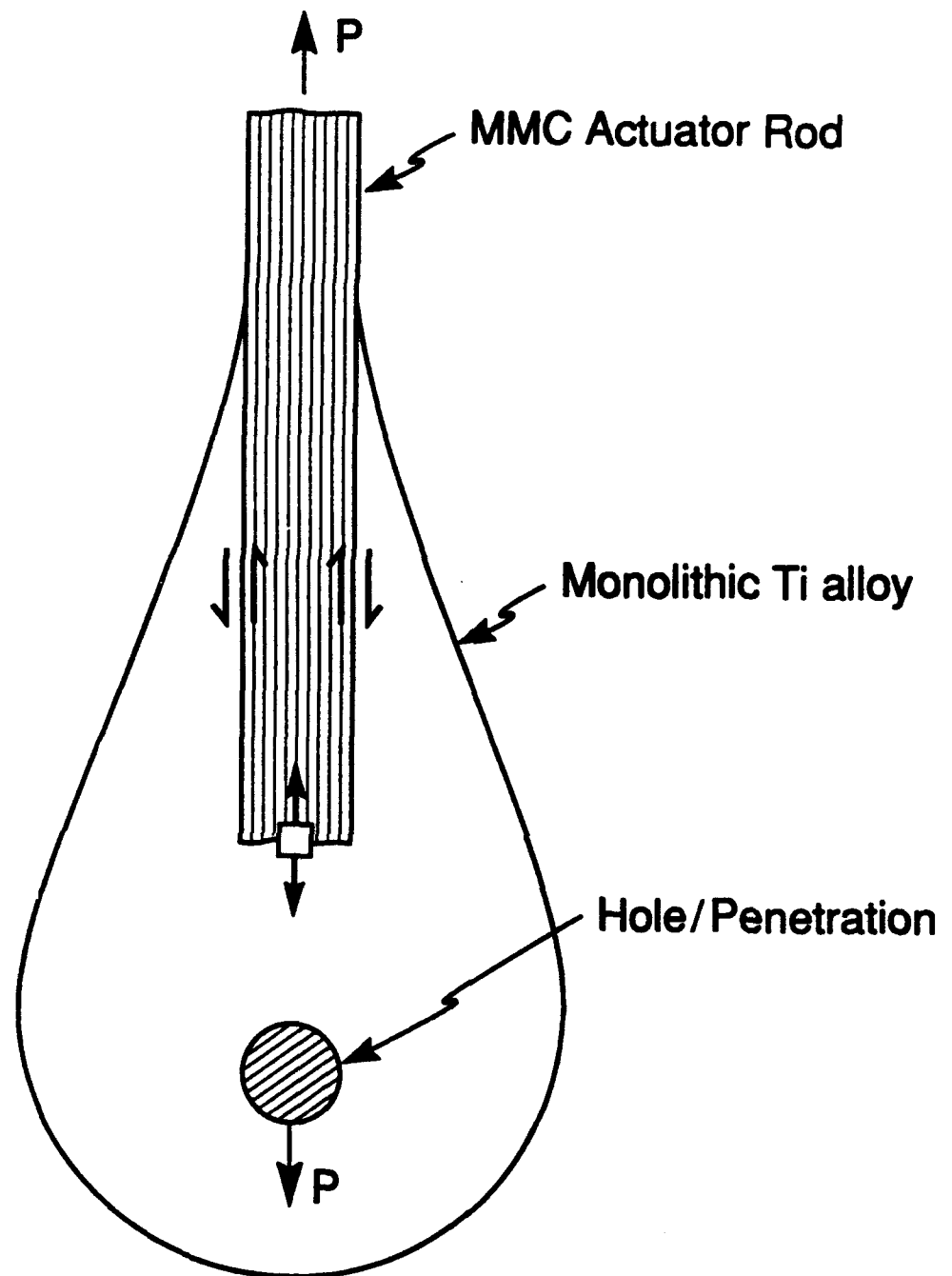


Figure 9.2

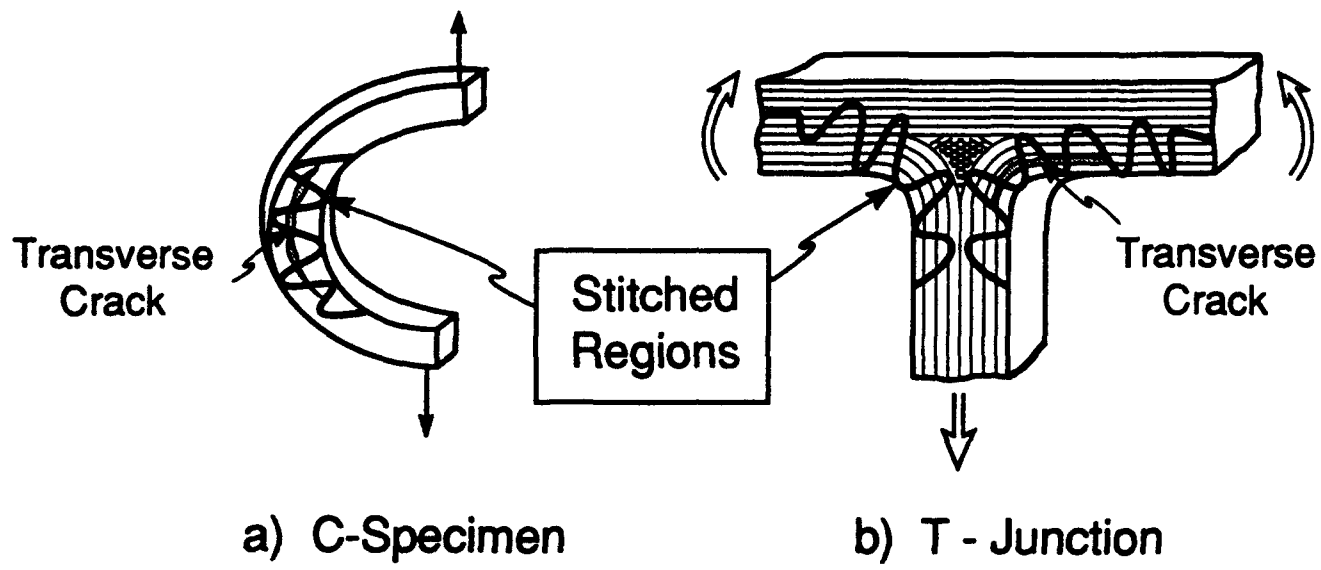


Figure 9.3

developments make the prospect of affordable high temperature fibers more realistic, evolving knowledge on the mechanical and thermochemical functions of interfaces have led to design concepts involving carefully tailored interphase layers, with unfavorable impact on cost. Moreover, if affordable coated fibers were available today, fabrication costs associated with consolidation and pressure densification would often remain prohibitive. Future processing and manufacturing activities are predicated on these issues, especially the need for new ideas, and the related knowledge base.

### 10.1 MMCs

Melt processing methods provide the more affordable options in composite synthesis with the added benefit of near-net shape capability. For continuous fiber composites melt infiltration also enables full density while minimizing the consolidation stresses that typically cause premature reinforcement failure in solid state processes. However, melt processing requires a high degree of thermochemical compatibility between matrix and reinforcement since deleterious diffusional interactions would be accelerated by the liquid phase. Conventional melt processing also exhibits limited ability to control the volume fraction and spatial uniformity of the reinforcements.

Among metal matrices, Ti alloys epitomize unsuitability for direct melt infiltration owing to aggressive reactivity. Fiber clustering is also a concern, even in solid state processes based on powder or foil matrices. Composite consolidation by vapor deposition (PVD) of the matrix on the fibers provides an avenue for improving *homogeneity of fiber spacing*. However, present schemes require expensive pressure densification with its many problems. A potential solution involves a hybrid manufacturing route wherein part of the matrix is first applied to the fibers by PVD. The pre-metallized fibers are then assembled into a preform having the desired shape and then infiltrated with the remaining matrix in liquid form.

Direct infiltration with Ti alloys could be feasible owing to the protection of the fiber by the PVD layer, but the high temperatures involved would exacerbate the diffusional interactions at the fiber-matrix interface. An alternate approach involves depositing the more refractory constituents of

the matrix (e.g., Ti, Nb, Mo, etc.) by PVD and then infiltrating with the lower melting point constituents (e.g. Al). Based on stoichiometric considerations, the latter approach would be suitable for matrices with  $\geq 25$  at.% Al, notably the orthorhombic and  $\alpha_2$  alloys. The obvious problem with this approach is the homogenization of the matrix after consolidation, which may require lengthy high temperature treatments in the solid state. However, a significant part of the matrix synthesis reaction could be effected in the presence of molten Al, followed by a final heat treatment in the solid state. While this lower temperature infiltration approach is evidently desirable from a manufacturing viewpoint, it is not clear that matrix homogenization can be achieved.

A program involving modeling and experimental work will be initiated in 1994 to generate the knowledge base appropriate to hybrid approaches for Ti matrix composites (Levi, Evans). Cell models (single fiber environment) would be developed to study diffusional interactions and remelting/solidification phenomena as a function of processing cycle (temperature-time history). Experiments would be performed to elucidate the relevant aspects of microstructural evolution and provide the reaction and interdiffusion kinetics needed to calibrate the models. Initial experiments would be performed by infiltrating pure Ti-wire preforms with molten Al and subjecting the "composite" to different treatments in the semi-solid state. Subsequent experiments would focus on developing a metallization route for Ti-Nb alloys on SiC fibers and on the relevant interactions with infiltrated Al. Larger scale modeling issues would be tackled in 1995 if the proposed approach appears promising.

Ongoing activities on the understanding of microstructure evolution and its relationship to properties in *in-situ* TMC systems based on TiB reinforcements would be continued (Levi). These are by nature affordable composites which exhibit inherent thermochemical stability and may be cast into shapes using conventional Ti processing techniques. A potential application of these materials would be in joints with unidirectionally reinforced composites, wherein their higher modulus and creep resistance combined with acceptable toughness and isotropic properties could be advantageous. It is also anticipated that these materials could be used for cladding in PVD or plasma-sprayed form, thereby reducing the potential for fatigue crack initiation in the cladding. Since TiB is thermochemically stable

with practically all Ti matrices of interest in fiber composites, such strengthening concepts may be readily implemented.

## 10.2 CMCs

Measurements and observations in 1993 have shown that strong, high strain to failure CMCs can be fabricated using an inexpensive method that involves a) packing a powder around fibers within a fiber preform using pressure filtration and b) making the powder matrix strong by heat treatment followed by infiltration with a liquid precursor that decomposes to an inorganic material. A composite made this way, with polycrystalline alumina fibers in a silicon nitride matrix, demonstrated that the matrix deflects the crack. This observation is significant since it suggest that a class of CMCs can be processed without needing weak fiber/matrix interfaces. The potential of this observation will be explored (Lange, Evans), by processing a composite with strong, polycrystalline alumina fibers in a mullite matrix because the thermomechanical properties of mullite minimize thermal stresses and resist creep. In addition, the thermal expansion mismatch is relatively small. Mixed Al, Si metal alkoxide precursors which can be gelled *in-situ*, prior to decomposition, will be used to strengthen the matrix.

Manufacturing studies would initiate with understanding the precursor infiltration into mullite power compacts. The densification of the matrix would be determined as a function of the cyclic infiltration. Microstructure changes would be controlled to avoid flaw populations during densification. The fracture toughness and the strength of the matrix would be determined as a function of the number of precursor infiltration cycles. Composite processing would initiate with precursor infiltration into alumina fiber preforms by pressure filtration, with emphasis on the colloidal aspects of this processing step. The goal would be to determine the processing conditions needed to produce a matrix that optimizes the ability to deflect cracks without degrading fiber strength. To optimize composite processing, panels for testing under conditions of both strain and stress control would be manufactured.

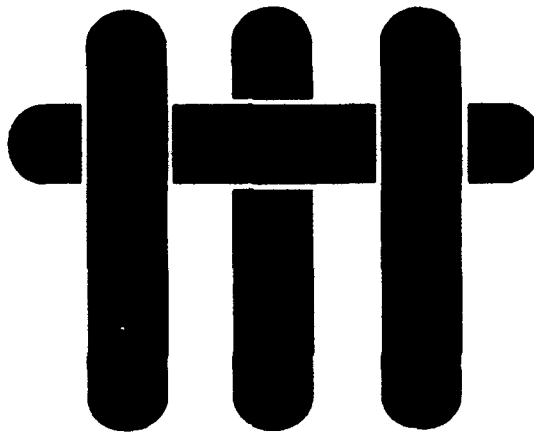
## 11. STRESS AND DAMAGE SENSORS

The extensive exploitation of the optical fluorescence method of measuring stresses in sapphire fiber and alumina-containing ceramic composites begun in 1993 will be continued in 1994 (Clarke, Wadley). The emphasis is on using the method to understand basic, unresolved issues in stress redistribution in composites by the direct measurement, with high spatial resolution, of the stresses themselves. Particular attention will be paid to determining the stress distribution associated with interfacial sliding. One of the problems to be addressed relates to new concepts for oxidation resistant interfaces within MMCs and CMCs, particularly the concomitant roles of fiber roughness and sintering on interface sliding and debonding, after exposure to high temperatures and cyclic loadings. For this purpose, fibers with fugitive, low modulus coatings will be explored and fluorescence measurements used to understand stress evolution and its connection with fiber durability within the composite. A second problem relates to the distinction between the line spring and large scale sliding models for fiber bridging (Budiansky, Hutchinson), so as to determine the range of applicability of the two models. The two competing models predict different distributions of stresses in the fibers within the bridging zone and hence are amenable to validation on the basis of the measured stress distribution.

Two approaches to measuring local damage are under development and will be the focus of the sensor activities. One is the use of acoustic methods (Wadley) to probe local variations in the elastic modulus of CMCs as a function of load. This should provide a means of mapping the distribution of damage which can be compared directly with the predictions of continuum damage mechanics models. The second approach (Clarke) is to detect the third harmonic signal generated by the presence of local damage. Preliminary experimental results obtained in 1993 concerned with the detection of crack-like voids in thin metal lines, together with computer simulation studies, have demonstrated the viability of the technique. This work will be extended in order to detect damage accumulation in CMCs and MMCs.



## M A T E R I A L S



**Residual Stress Measurement in Sapphire Fiber  
Composites: Through-Focus and Transmission  
Fluorescence Spectroscopy**

Don M.Lipkin and David R.Clarke

Materials Department, University of California  
Santa Barbara, CA 93106

Don M. Lipkin and David R. Clarke<sup>1</sup>

**RESIDUAL STRESS MEASUREMENT IN SAPPHIRE-FIBER COMPOSITES:  
THROUGH-FOCUS AND TRANSMISSION FLUORESCENCE SPECTROSCOPY**

---

**Reference:** Lipkin, D.M. and Clarke, D.R., "Residual Stress Measurement in Sapphire-Fiber Composites: Through-Focus and Transmission Fluorescence Spectroscopy," Fracture Mechanics: 25th Volume, ASTM STP 1220, F.Erdogan and R.J.Hartranft, Eds., American Society for Testing and Materials, Philadelphia, 1994.

**Abstract:** A method to non-intrusively measure stresses both at and below the surface of structural components is developed. Based on the piezo-spectroscopic effect in optical fluorescence, this technique affords high-accuracy stress measurement with spatial resolution on the order of one micron. The theoretical basis for the piezo-spectroscopic effect is reviewed, and several concepts relevant to its application are established. The applicability of fluorescence spectroscopy to stress measurement is demonstrated on two sapphire-fiber reinforced composites, one with  $\gamma$ -TiAl and the other with  $\alpha$ -Ti as the matrix. The residual stress distributions along the fibers are measured using a through-focusing procedure, and a mean volume stress is determined using a transmission fluorescence configuration. The effective temperature below which residual stresses can no longer be relieved by creep and yielding is determined using an elastic model. In the TiAl-matrix composite, this temperature is approximately 400°C below the processing temperature, indicating extensive stress relaxation during cooling. The elastic solution fails to provide a reasonable estimate of the stress-free temperature for the Ti-matrix system. This is attributed to extensive matrix yielding, and a complete treatment will require incorporation of inelastic constitutive behavior into the model.

**Keywords:** stress measurement, residual stress, piezo-spectroscopy, fluorescence, sapphire, ruby, TiAl matrix, Ti matrix

---

**1. Introduction**

The need to study microscale properties of materials has led to the development of various high-resolution microscopic techniques, such as scanning electron, transmission electron, scanning-tunneling, and

---

<sup>1</sup>Graduate student researcher and professor, respectively, Materials Department, University of California, Santa Barbara, CA 93106.

atomic force microscopy. However, advances in morphological and crystallographic evaluation have not been complemented with a corresponding development in techniques for measuring micromechanical properties. Although such techniques as microfocus X-ray diffraction [1] and high-accuracy strain-field mapping (HASMAP) [2] have made possible the evaluation of surface strains with improved spatial resolution, these methods are inherently limited to superficial measurements. In the present study, a recently-developed technique based on the piezo-spectroscopic effect in optical fluorescence is employed to obtain stress information well below the sample surface [3,4,5]. This technique has been shown to routinely combine micron-scale spatial resolution with a corresponding stress resolution to approximately 10 MPa.

One of the goals of the spectroscopic stress measurement technique is to provide the means for experimentally determining spatial stress distributions in residually-stressed or externally-loaded components. Such data is not only crucial in validating finite element predictions, but can be integrated into on-line quality control and evaluation procedures requiring the precise knowledge of stress levels within structural components. In the present study, we determine the residual stress distribution along sapphire fibers in two composites, one with a  $\gamma$ -TiAl matrix and the other an  $\alpha$ -Ti matrix. The stresses develop upon cooling from the fabrication temperature as a result of the difference in thermoelastic properties between matrix and reinforcement. These stresses are only partially relieved by creep at high temperatures and dislocation plasticity at low temperatures. Because of these relaxation processes, particularly near the fiber ends, the stress distribution along the fibers is not amenable to computational analysis and has to be measured directly. To determine the stress distribution, we have employed the fluorescence spectroscopy technique and applied it in two configurations: one, in which successively deeper regions are probed by focusing an optical lens down the axis of the reinforcing fibers, and the second, in which the whole fiber is probed simultaneously in transmission. The two procedures are detailed following a description of the physical basis of the piezo-spectroscopic technique.

## 2.1 Piezo-Spectroscopic Effect

The piezo-spectroscopic (PS) effect is based on the sensitivity of electronic transitions of substitutional ions, or phosphors, to stress-induced changes in the local crystal field of the host lattice. A common example is ruby, in which  $\text{Cr}^{3+}$  ions substitute for  $\text{Al}^{3+}$  ions on the corundum lattice. When ruby is excited with ultraviolet or sufficiently energetic visible-wavelength radiation, the  $\text{Cr}^{3+}$  ions undergo an electronic transition from the  $^4\text{A}_2$  ground state to the broad  $^4\text{T}_1$  and  $^4\text{T}_2$  bands, followed by a rapid non-radiative decay to one of two components of the  $^2\text{E}$  level (Fig.1). The subsequent decay from  $^2\text{E}$  to the  $^4\text{A}_2$  ground state is accompanied by the radiation of photons having frequencies within the visible spectrum, a phenomenon called optical fluorescence. In a stress-free single crystal of sapphire, the fluorescence lines corresponding to the  $2\bar{\text{A}} \rightarrow ^4\text{A}_2$  transition ( $R_2$ ) and the  $\bar{\text{E}} \rightarrow ^4\text{A}_2$  transition ( $R_1$ ) are separated by approximately  $29 \text{ cm}^{-1}$  and occur at frequencies of 14448 and  $14419 \text{ cm}^{-1}$ , respectively [6]. However, as the crystal field about the  $\text{Cr}^{3+}$  ion is perturbed, its electronic states are displaced with respect to one another, resulting in a systematic frequency shift of the fluorescence signal. Although the crystal field can be affected by external electric fields or in the vicinity of

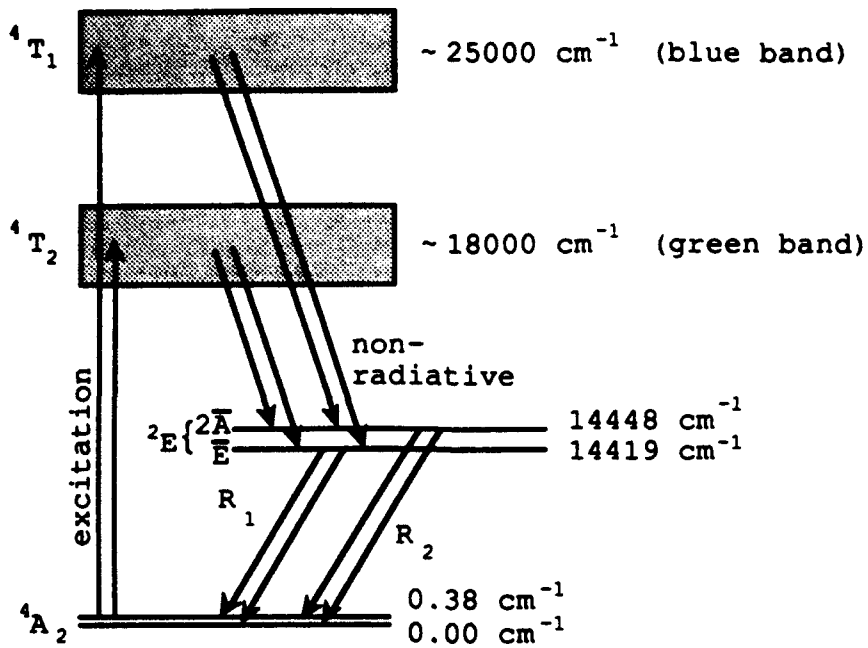


Fig.1 Electronic transitions for a  $\text{Cr}^{3+}$  ion in a sapphire host lattice, illustrating the origin of the  $R_1$  and  $R_2$  fluorescence lines.

lattice defects, the present emphasis is on the fluorescence frequency shifts caused by tractions imposed upon the host lattice -- the piezo-spectroscopic effect.

## 2.2 Application of the PS Effect to Stress Measurement

As mentioned above, the piezo-spectroscopic effect can be employed to relate fluorescence frequency shifts to the local stress tensor. This constitutive relationship is usually described through the piezo-spectroscopic tensor,  $\Pi$ :

$$\Delta v(\sigma_{ij}) = \Pi_{ij}\sigma_{ij} \quad (1)$$

where  $\Delta v$  refers to the frequency shift,  $\Pi_{ij}$  is the  $ij$ -th component of the piezo-spectroscopic tensor, and  $\sigma_{ij}$  is the corresponding component of the stress tensor (in the crystallographic basis of the host lattice). The higher-order terms in the expansion of the frequency shift have been confirmed to be negligible for most purposes [7,8] and are therefore excluded from Eqn.(1).

In addition to stress dependence, the fluorescence frequency has varying degrees of sensitivity to temperature, applied electric field, and dopant concentration. To a first-order approximation, the various contributions to the fluorescence line shift are taken to be linearly superposable [9], such that the net frequency shift can be described as:

$$\Delta v = \Delta v(\sigma_{ij}) + \Delta v(E_i) + \Delta v(T) + \Delta v(c), \quad (2)$$

where the individual components correspond to the stress, applied

electric field, temperature, and concentration dependence, respectively.

For our investigations, no external electric fields are applied and it is assumed that the dopants are homogeneously distributed on the host lattice, so that Eqn.(2) reduces to the stress- and temperature-dependent terms. The temperature dependence of frequency can be described through a scalar correction factor:

$$\Delta\nu(T) = \beta(T) T \quad (3)$$

where  $\beta$  is experimentally found to have a weak dependence on temperature over small excursions, and varies slightly between the  $R_1$  and  $R_2$  lines [10-12].

The piezo-spectroscopic tensor is a physically-measurable material parameter that reflects the symmetry of the host lattice. For the case of sapphire as the host, the site symmetry of  $\text{Cr}^{3+}$  ( $D_{3d}$ ) reduces the piezo-spectroscopic tensor to the form:

$$\Pi = \begin{bmatrix} \Pi_a & 0 & 0 \\ 0 & \Pi_a & 0 \\ 0 & 0 & \Pi_c \end{bmatrix} \quad (4)$$

where  $\Pi_a$  and  $\Pi_c$  refer to the components oriented along the  $a$ - and  $c$ -axes of the sapphire unit cell, respectively. By uniaxially stressing single crystals of ruby, He and Clarke found  $\Pi_a$  and  $\Pi_c$  to be 3.45 and  $1.51 \text{ cm}^{-1}/\text{GPa}$  for the  $R_1$  line and 2.75 and  $2.11 \text{ cm}^{-1}/\text{GPa}$  for the  $R_2$  line, respectively [7]. For the case of a reinforcing sapphire fiber having its axis oriented along the crystallographic  $c$ -axis of sapphire, the frequency shift is obtained directly from Eqns.(1) and (4):

$$\Delta\nu(\sigma_{ij}) = \Pi_a(\sigma_{rr} + \sigma_{\theta\theta}) + \Pi_c\sigma_{zz}, \quad (5)$$

where  $\sigma_{rr}$ ,  $\sigma_{\theta\theta}$ , and  $\sigma_{zz}$  are the radial, tangential, and axial components of the stress tensor, respectively.

Although Eqn.(5) is adequate for providing a semi-quantitative measure of the stress state within the reinforcing fiber, it is insufficient when a full stress tensor solution is required. The problem arises due to the lack of a universal relationship between the individual components of the stress tensor. In most situations, such relationships can only be determined from numerical (e.g., finite element) calculations. However, there exists a limited number of simplified geometries and constitutive models for which the relationship between stress tensor components can be found analytically. One such configuration is a cylindrical fiber embedded in an infinite matrix having dissimilar but isotropic thermoelastic properties. With the assumptions that both components are linear-elastic and that no displacement is allowed at the fiber/matrix interface (fixed boundary conditions), the components of the residual stress tensor can be rigorously related using elasticity theory:

$$\begin{aligned} \sigma_{\theta\theta} &= \sigma_{rr} \\ \frac{\sigma_{zz}}{\sigma_{rr}} &= K_{eff} + 1, \end{aligned} \quad (6)$$

where:

$$\mathfrak{R}_{\text{eff}} = \frac{\int_{T_0}^{T_{\text{eff}}} \mathfrak{R} E_i^{\text{eff}} \Delta a dT}{\int_{T_0}^{T_{\text{eff}}} E_i^{\text{eff}} \Delta a dT}, \quad \mathfrak{R} = \frac{E_f}{E_m} \left( \frac{1 + v_m}{1 + v_f} \right), \quad \text{and} \quad E_i^{\text{eff}} = \frac{E_f}{(2v_f - 1) - \mathfrak{R}}.$$

$E_{f,m}$  and  $v_{f,m}$  are the fiber and matrix elastic moduli and Poisson's ratios, respectively, and are allowed to have a temperature dependence from room temperature,  $T_0$ , to the effective stress-free temperature,  $T_{\text{eff}}$ .<sup>a</sup> Combining Eqns. (5) and (6), the frequency shift measured within the bulk of a fiber composite can be uniquely related to the thermal residual stress state.

### 3.1 Through-Focus Stress Measurement

In the through-focus technique, the spatially-resolved stress distribution is obtained by incrementally focusing a laser beam along the fiber axis and collecting the fluorescence that is excited about the focal point (Fig. 2). Both the excitation and collection of the fluorescence signal are implemented using a conventional optical microscope; as a consequence, the spatial resolution of the technique is limited only by the aberrations of the optical components, and ultimately by the Rayleigh resolution limit.

Although the through-focus measurement is nominally straightforward, the optical lenses that are used for the excitation and collection of the fluorescence signal have a finite depth of field. Consequently, the signal collected from any depth,  $z_0$ , below the surface is a spatial convolution of the true signal distribution,  $f(z)$ , with a system response function,  $r(z)$ , which acts to spread out the collected information over a finite volume in space [13]. Typically, the collection volume has dimensions of approximately 30 microns along the  $z$ -axis (Fig. 2) and 5 microns in the  $x-y$  plane, although the exact values depend strongly upon the collection optics, including lenses, slits, and apertures. As a result of the finite collection volume, the measured frequency distribution may need to be numerically deconvoluted in order to determine the true spatial frequency distribution. Although the data in the following experiments were not deconvoluted, such a procedure becomes increasingly important in cases where large stress gradients exist within the sample.

The collected signal,  $c(z)$ , from position  $z$  along the fiber, can be described mathematically as a convolution of  $f(z)$  and  $r(z)$ :

$$c(z) = f(z) \otimes r(z) = \int_{-\infty}^{\infty} f(\xi) r(z - \xi) d\xi, \quad (7)$$

where the integral describes the passing of a function  $f(z)$  through  $r(z)$ . The response function can be experimentally measured if the integrated intensity under the  $R_1$  and  $R_2$  fluorescence peaks is taken to be the system function,  $c(z)$ . Assuming that the integrated fluorescence intensity is only dependent on the geometry of the sample (e.g., the intensity is zero outside the sample and has a constant value,  $A$ , within

<sup>a</sup> If the temperature dependence of  $E_{f,m}$ ,  $v_{f,m}$ , and  $\alpha_{f,m}$  is ignored,

Eqn. (6) degenerates to:  $\frac{\sigma_{zz}}{\sigma_{rr}} = \mathfrak{R} + 1 = \frac{E_f}{E_m} \left( \frac{1 + v_m}{1 + v_f} \right) + 1$ .

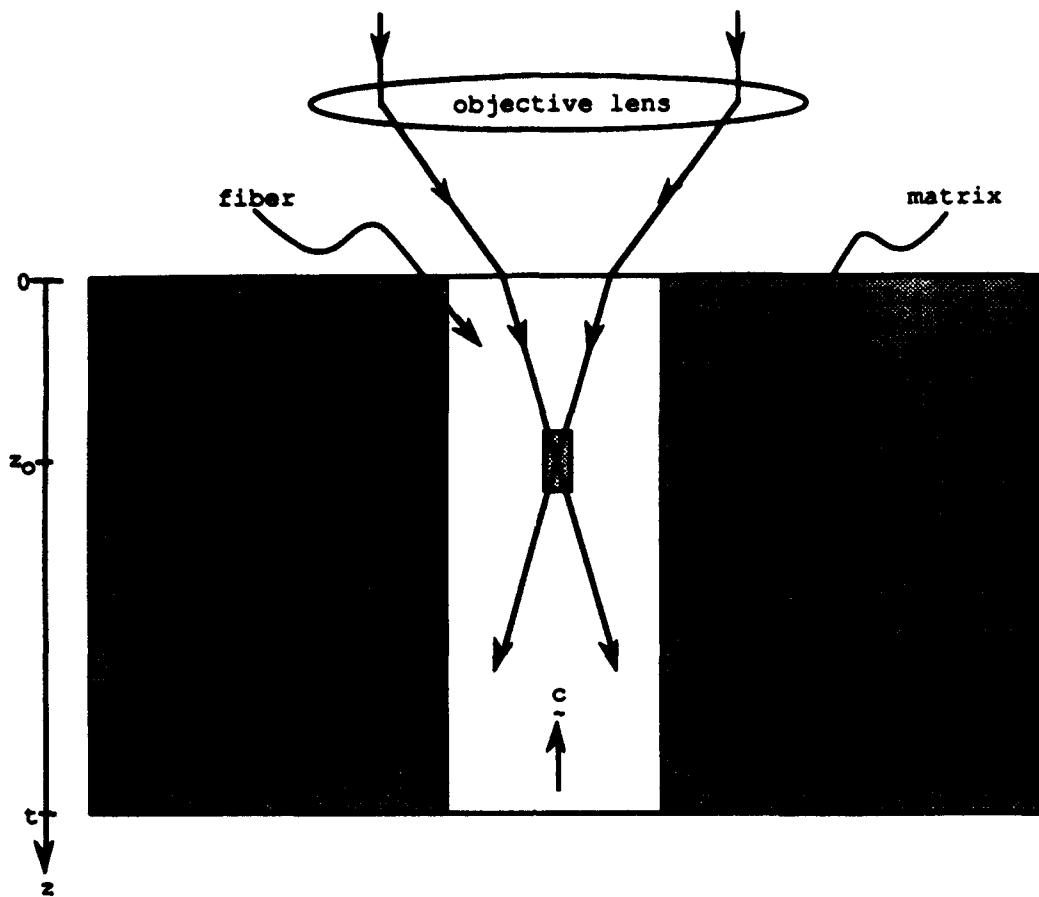


Fig.2 Through-focus fluorescence configuration illustrating that the signal is collected from a finite volume. The fiber axis is oriented parallel to the sapphire c-axis.

the sample), Eqn. (7) can be solved explicitly for the response,  $r(z)$ :

$$r(z) = \frac{1}{A} \frac{dc(z)}{dz}. \quad (8)$$

Once the response function is known, the true function can be recovered through the application of the convolution theorem of Fourier transforms:

$$f(z) = \mathcal{F}^{-1} \left[ \frac{C(u)}{R(u)} \right]. \quad (9)$$

Ultimately, the experimental measurement of the stress distribution using the through-focus technique consists of a two-step process: collection of the frequency data at incremental depths below the component surface and, if needed, numerical deconvolution of the frequency profile using a pre-calibrated response function. However, the technique becomes increasingly cumbersome to apply as the component size increases, motivating the development of the transmission fluorescence technique.

### 3.2 Transmission Stress Measurement

Although the through-focus technique provides a powerful tool for microscale stress profiling, it suffers from several practical limitations. First, the technique relies on the collection of a large data set. In general, the spatial resolution scales in direct proportion to the number of data points collected. Thus, when the region of interest is large, the time required to collect a sufficient amount of data to provide the prescribed spatial resolution may be prohibitive. The second drawback derives from the physical limitations imposed by the probing optics and sample geometry. When the focal plane reaches a critical depth below the surface of the sample (usually related to some characteristic sample dimension, such as grain size or fiber diameter), the system response function broadens dramatically, resulting in a rapid loss of resolution. Finally, a thorough mapping of the stress distribution may require an involved numerical deconvolution procedure to correct for the system response. All of the above limitations can be circumvented by resorting to the transmission fluorescence technique, wherein the whole sample volume is simultaneously excited into fluorescence by an external illumination source.

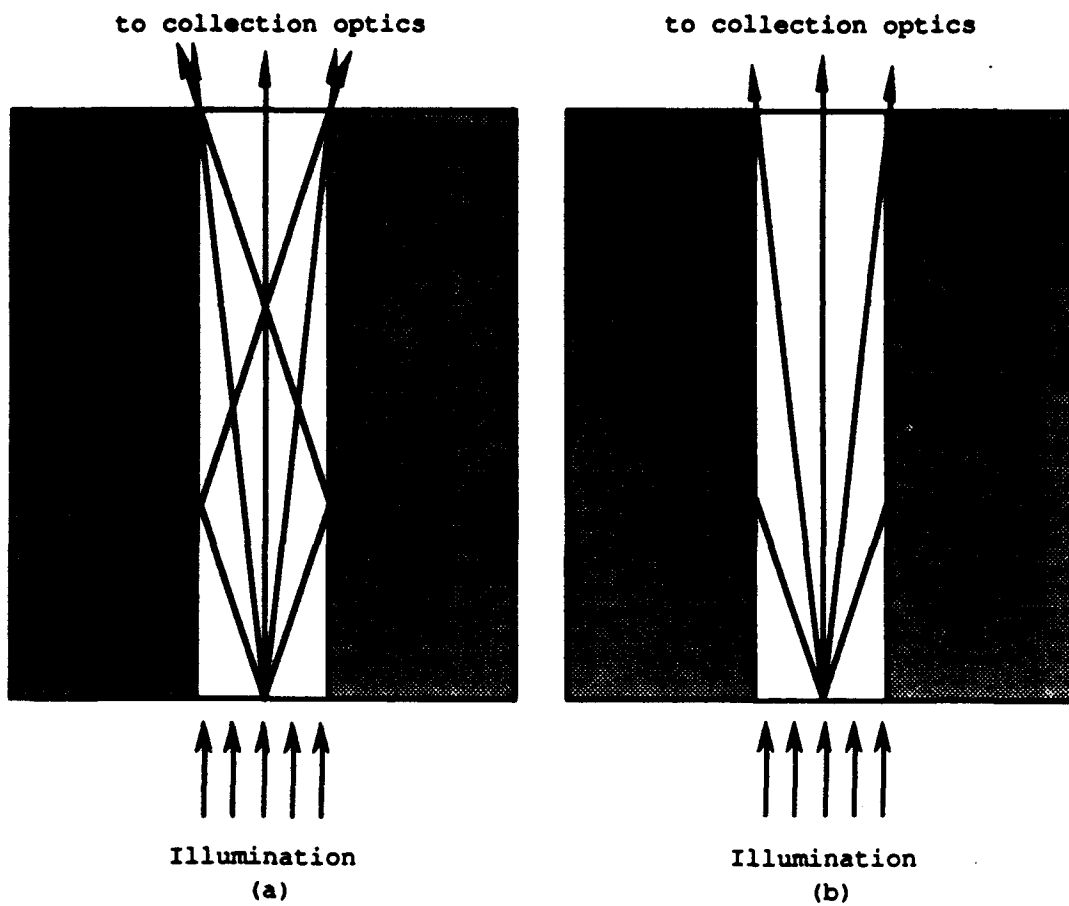


Fig.3 Transmission fluorescence configurations for a fiber embedded in an opaque matrix: (a) total internal reflection and (b) complete absorption at the fiber/matrix interface.

In the transmission fluorescence technique, the excitation source is placed at one end of the sample and the fluorescence signal is collected from the other end using a low-magnification objective lens (Fig. 3). This configuration is not only simple to implement, but has the additional advantage over the through-focusing technique of allowing components of indefinite length to be probed.

In general, the transmitted frequency,  $\bar{v}$ , at which the fluorescence line is located can be described using a geometrical signal-weighting function,  $w$ :

$$\bar{v} = \frac{\int_v w v dv}{\int_v w dv}, \quad (10)$$

where  $v$  is the frequency of the fluorescence line within an infinitesimal fiber volume element,  $dv$ . In analyzing stresses within embedded fibers using the transmission fluorescence geometry, two extreme conditions are possible: total internal reflection and complete absorption at the fiber/matrix interface (Fig. 3). Neglecting the effects of absorption within the bulk of the fiber, it can be shown that for the case of complete reflection at the fiber/matrix interface, the weighting function is independent of position and the transmitted signal is simply the volume-averaged frequency over the illuminated region of the sample:

$$\bar{v} = \frac{1}{V} \int_v v dv. \quad (\text{reflection}) \quad (11)$$

In contrast to the above situation, for the case of complete absorption at the fiber interface, the weighting function is sensitive to the numerical aperture of the collection optics. The full treatment of this problem is too extensive to provide physical insight; however, with a few simplifying assumptions, a useful approximation for the transmitted frequency can be made. It is assumed that, for the case of a cylindrical fiber embedded in a continuous matrix, there is no radial or angular dependence of frequency (or equivalently, of stress). This assumption is expected to hold well within the bulk of the sample (Eqn. (6)), where the fiber can be treated as an equivalent inclusion using the Eshelby formulation [14]. (The premise that the fiber stress state is constant is known to fail near the fiber ends, where surface relaxation distorts the stress field.) Additionally, the sample thickness,  $t$ , is assumed to be simultaneously greater than the fiber diameter and less than a characteristic length,  $t_0$ , defined by the system geometry:

$$t_0 \equiv R/\theta_2, \quad (12)$$

where  $R$  is the fiber radius and  $\theta_2$  is the angle the refracted beam makes with the fiber axis.  $\theta_2$  can, in turn, be related to the numerical aperture,  $NA$ , of the collection lens and the refractive index,  $n_{fiber}$ , of the fiber:  $\theta_2 = \sin^{-1}(NA/n_{fiber})$ . Under the former assumptions, the transmitted frequency can be calculated:

$$\bar{v} = \frac{\int_{t_0-t}^{t_0} \chi(z) v dz}{1 - \int_0^{t_0-t} \chi(z) dz}, \quad (\text{absorption})$$

where

$$\chi(z) = \frac{1}{t_0} \left\{ \frac{33}{49} + \frac{18}{49} \left( \frac{z}{t_0} \right) + \frac{21}{49} \left( \frac{z}{t_0} \right)^2 \right\}. \quad (13)$$

It is interesting to note that even for the case of complete absorption of the signal at the fiber/matrix interface, the weighting function has only a weak polynomial dependence on depth. As a result, for very short fibers ( $t=t_0$ ), Eqns. (11) and (13) predict very similar frequencies in transmission, making the determination of the exact extent of reflection at the interface unnecessary. However, for long fibers, the assumptions behind Eqn. (13) fail, and it can be easily shown that reflection at the interface is crucial to obtaining a signal in transmission.

#### 4. Experimental Procedure

The characteristics of the two composites used in the evaluation of fiber stress distributions are summarized in Table 1. The samples were machined to orient the free surfaces normal to the fiber axes, and the exposed ends were metallographically polished to a one-micron finish to remove machining stresses and attain an optically smooth surface.

The details of the through-focus and transmission fluorescence experiments are described in Sections 3.1 and 3.2, respectively. The general data collection and analysis procedures for both configurations were similar. The fluorescence spectra were collected using a triple-grating Raman spectrometer.<sup>b</sup> The line frequencies, widths, and intensities of the fluorescence signals were obtained by fitting the spectra to a double pseudo-Voigtian function, one for each of the R-lines, using a commercial curve-fitting software package.<sup>c</sup> With each fluorescence spectrum, a characteristic neon line was recorded as a spectral reference to correct for possible mechanical drift in the spectrometer. The sample temperature was monitored to correct for the temperature dependence of the fluorescence shift (Eqn. (3)).

The two composite samples exhibited a relatively wide range of thermoelastic and mechanical properties. The titanium aluminide was not expected to undergo extensive plastic deformation far below the processing temperature, whereas the titanium matrix was considered susceptible to plastic yielding under the thermal residual stresses. In

TABLE 1--Composite systems used for residual stress measurements

Sample	Fiber	Coating	Matrix	Consolidation
IMC	sapphire	Mo/Al <sub>2</sub> O <sub>3</sub>	γ-TiAl	HIP* at 1070°C
MMC	ruby	none	α-Ti	UHP# at 900°C

\*HIP = hot isostatic press

#UHP = uniaxial hot press

<sup>b</sup> Raman Microprobe Model T64000, Instruments SA.

<sup>c</sup> Spectra Calc, Galactic Industries Corporation.

addition, to ensure that the transmission configuration could be applied to arbitrary specimen sizes, both a thin and a thick sample were examined; the titanium-matrix composite was approximately 15 millimeters thick (corresponding to a fiber aspect ratio of 70:1), compared to 0.7 millimeters for the aluminide sample (aspect ratio of 5.5:1).

## 5. Results and Discussion

Figures 4a and b show the frequency distributions along the fiber axes in the TiAl- and Ti-matrix composites, respectively. Marked differences in the residual stress distributions are immediately apparent between the two composites. For the case of the intermetallic-matrix composite, the stress state (related to frequency through Eqns. (5) and (6)) builds up rapidly from the surface-relaxed to the bulk state. The stress reaches a plateau value within approximately one fiber diameter, indicating complete load transfer via the interface and full plane-strain constraint.

In contrast to the TiAl matrix, the more compliant titanium matrix exhibits much longer load transfer lengths, as evidenced by the steadily-increasing stress at depths up to three times the fiber diameter (Fig. 4b). In fact, the depth corresponding to complete constraint was beyond the maximum possible probing depth (approximately 600 microns, or three fiber diameters). To measure the transfer length, it was necessary to rely on transmission fluorescence data. Once the bulk stress state was measured in transmission, the load transfer length was estimated from the slope of the frequency curve of Fig. 4b to be nine times the fiber diameter.

The frequency corresponding to the signal obtained in transmission is superimposed onto the vertical axis in Figs. 4. In order to verify the validity of the transmitted frequency, signals were collected from

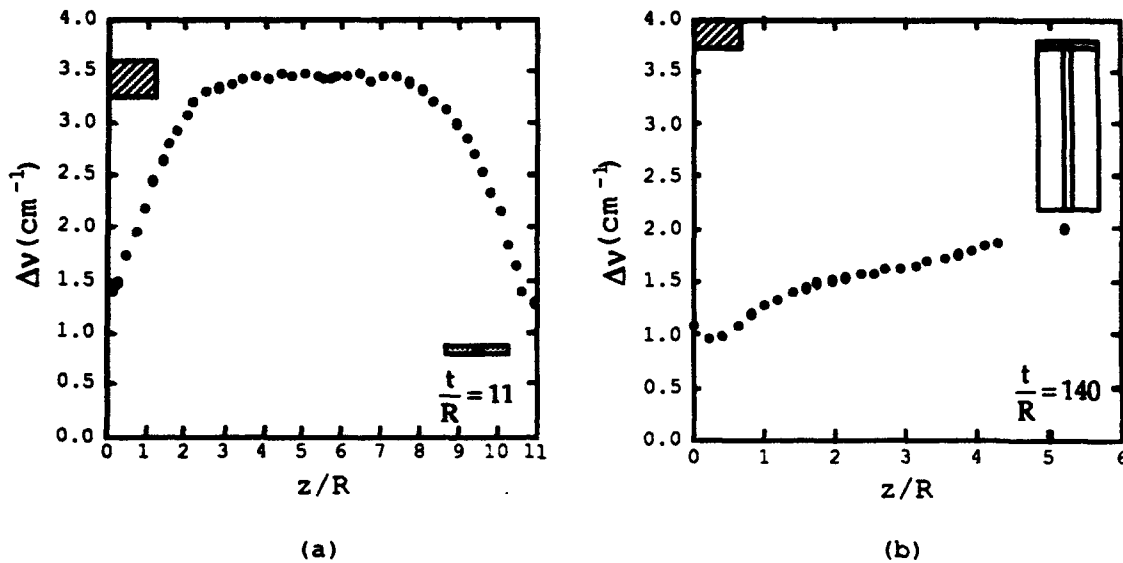


Fig. 4  $R_1$  frequency shift distribution along the reinforcing sapphire fiber in (a) TiAl-matrix and (b) Ti-matrix composites. The transmitted frequency is indicated by the shaded box in the upper left corner. The total fiber lengths for the TiAl and Ti composites were 0.7 and 15 mm, respectively.

TABLE 2--Thermoelastic properties of TiAl- and Ti- matrix composites\*

Sample	$E_f$ (GPa)	$E_m$ (GPa)	$v_f$	$v_m$	$\Delta\alpha \times 10^{-6} \text{ } ^\circ\text{C}^{-1}$
Ti/Al <sub>2</sub> O <sub>3</sub>	380	110	0.26	0.32	2.35
TiAl/Al <sub>2</sub> O <sub>3</sub>	380	160	0.26	0.24	3.55

\*Values for  $E$ ,  $v$ , and  $\Delta\alpha$  are room temperature quantities.  $\Delta\alpha = \alpha_m - \alpha_f$ .

both ends of the specimens to assure invariance. For the thick Ti/Ruby sample, the signal was collected from several focal planes. Invariance of these signals guarantees that extensive reflection at the interface obtains, in accordance with Eqn.(11). In all cases, the transmitted signals were consistent to within experimental accuracy. As expected, the frequency shift determined from transmission falls slightly below the plateau value for the TiAl composite (Fig. 4a). For the Ti-matrix composite, the transmitted frequency is almost twice the maximum value measured using the through-focus technique (Fig. 4b). Extrapolation of the spatially-resolved data to the transmitted value reveals that the bulk stress state is not reached until 9 fiber diameters below the surface, as mentioned above.

The residual stress components within the bulk of each fiber were calculated from the plateau (i.e., fully-constrained) frequency shift using Eqns.(5) and (6) in conjunction with the appropriate thermoelastic constants (Table 2) and their known temperature dependencies. The results are presented in Table 3. Using these values in the elasticity solution for the thermal residual stress,<sup>d</sup> the effective elastic cooling range,  $\Delta T_{eff}$ , was calculated for the two composites (Table 3). This range corresponds to the effective freezing, or stress-free, temperature, below which creep and dislocation plasticity mechanisms become ineffective (i.e., material is essentially linear-elastic) and above which the residual stresses are fully relaxed. For the TiAl-matrix composite, the effective stress-free temperature is found to be approximately 670°C (400°C below the peak processing temperature), indicating that extensive relaxation had occurred via high-temperature creep, as well as possible microcracking and interfacial slippage at lower temperatures.

When the residual stresses were used to calculate  $T_{eff}$  for the Ti/ruby composite, the resulting temperature was found to exceed the melting temperature of titanium. This apparent discrepancy suggests that the degree of yielding in this composite is so extensive that the

TABLE 3--Residual stresses and effective freezing temperatures of TiAl- and Ti- matrix composites based on linear-elastic model

Sample	$\bar{\sigma}_{zz}$ (MPa)	$\bar{\sigma}_{rr}$ (MPa)	$\Delta T_{eff}$ (°C)
Ti/Al <sub>2</sub> O <sub>3</sub>	-1325	-285	N/A
TiAl/Al <sub>2</sub> O <sub>3</sub>	-955	-290	650

<sup>d</sup> Solutions, derived using boundary conditions set forth in section 2.2, are:  $\sigma_{rr} = \int_{T_0}^{T_{eff}} E_f^{eff} \Delta\alpha dT$  and  $\sigma_{zz} = \int_{T_0}^{T_{eff}} (\lambda + 1) E_f^{eff} \Delta\alpha dT$ .  $\Delta T_{eff} = T_{eff} - T_0$ .

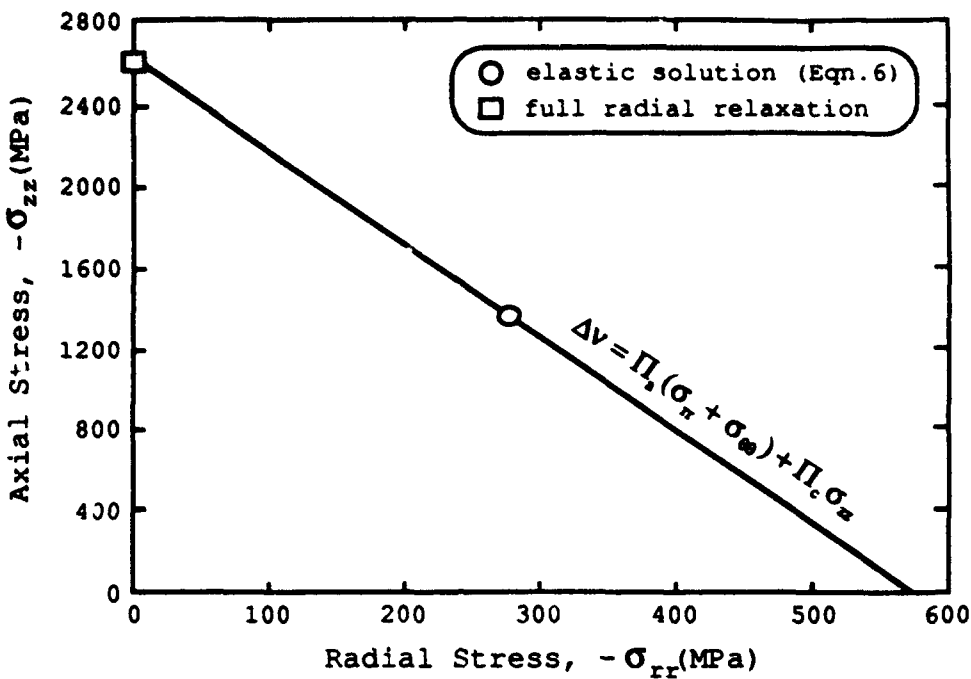


Fig. 5 Graphical solution of the piezo-spectroscopic equation for Ti/ruby. The stress states corresponding to the elastic model, as well as to the extreme case of complete radial relaxation are indicated.  $\Delta v = 3.95 \text{ cm}^{-1}$ ,  $\Pi_a = 3.45 \text{ cm}^{-1}/\text{GPa}$ ,  $\Pi_c = 1.51 \text{ cm}^{-1}/\text{GPa}$ , and  $\sigma_{zz} = \sigma_{rr}$ .

elastic model used to relate the axial and radial stress components within the fiber (Eqn. (6)) is not applicable. As described in Section 2.2, the piezo-spectroscopic relation given by Eqn. (5) does not uniquely define the full stress tensor. For the axisymmetrical case of a cylindrical fiber embedded in a matrix, an additional relation between the axial and radial components is necessary to determine the stress tensor uniquely. A graphical representation of the piezo-spectroscopic solution for the Ti/ruby composite defines a one-dimensional surface in stress space (Fig. 5). The elastic model defines one possible solution, but it is clear that other solutions may be indicated by amending the constitutive model to include matrix plasticity and cracking [15]. In all cases, however, the piezo-spectroscopic data provides the necessary physical constraint upon the solution.

## 6. Conclusions

The applicability of fluorescence spectroscopy to stress measurements in both the through-focus and transmission configurations has been experimentally established in two sapphire-fiber composites. For the case of the metal-matrix composite, the load transfer length was found to be several times greater than that for the intermetallic-matrix composite. This trend is ascribed to the lower stiffness and yield strength of the titanium compared to titanium aluminide. Experiments on the 800-micron thick TiAl composite confirmed the validity of the transmission fluorescence method through the strong correlation between

the axial stress profile and the stress measured in transmission. The applicability and utility of the method were demonstrated on a long metal-matrix composite ( $t/R=70$ ), for which transmission fluorescence was found to be the only means by which to estimate the bulk stress state and load transfer length.

Having established the fluorescence method as a viable technique for micromechanical measurements, current emphasis is being directed toward a strong correlation between frequency shift measurements and the full stress tensor, as applied to components of arbitrary geometry and loading conditions. This involves the relation of both frequency shifts and line shapes to the local stress tensor using finite element and analytical constitutive calculations.

**Note:** Since preparation of this manuscript, He and Clarke [7] have confirmed that the piezo-spectroscopic coefficients of ruby are distinct for the  $R_1$  and  $R_2$  lines. As a result, an independent relation is obtained from the frequency shift of each of the two fluorescence lines (Eqn. (5)). This should allow the principal stress components in an axisymmetrical system to be uniquely determined without the need for a constitutive law.

**Acknowledgments:** We would like to thank Heather Hough of the University of Virginia for providing the Ti/ruby sample. This research is being funded by a DARPA-URI grant under contract number N00014-86-K-0793. DML is supported by an Office of Naval Research Fellowship.

## 7. References

- [1] Halmshaw, R., "Microfocus X-Rays," *British Journal of Non-Destructive Testing*, Vol.27, No.4, 1985, p.220.
- [2] James, M.R., Morris, W.L., and Cox, B.N., "A High Accuracy Automated Strain-Field Mapper," *Experimental Mechanics*, Vol.30, 1990, pp.60-68.
- [3] Grabner, L., "Spectroscopic Technique for the Measurement of Residual Stresses in Sintered  $\text{Al}_2\text{O}_3$ ," *Journal of Applied Physics*, Vol.49, No.2, 1978, pp.580-583.
- [4] Molis, S.E. and Clarke, D.R., "Measurement of Stresses Using Fluorescence in an Optical Microprobe: Stresses around Indentations in a Chromium-Doped Sapphire," *Journal of the American Ceramic Society*, Vol.73, No.11, 1990, pp.3189-3194.
- [5] Ma, Q. and Clarke, D.R., "Stress Measurements in Single-Crystal and Polycrystalline Ceramics Using Their Optical Fluorescence," *Journal of the American Ceramic Society*, Vol.76, No.6, 1993, pp.1433-1440.
- [6] Nelson, D.F. and Sturge, M.D., "Relation between Absorption and Emission in the Region of the R Lines of Ruby," *Physical Review*, Vol.137, No.4A, 1965, pp.A1117-A1130.
- [7] He, J. and Clarke, D.R., "Determination of Piezo-Spectroscopic Coefficients in  $\text{Cr}^{3+}$ -Doped Sapphire," to be published, 1994.
- [8] Liu, H., Lim, K.-S., Jia, W., Yen, W.M., Buoncristiani, A.M., and Byvik, C.E., "Effects of Tensile Stress on the R Lines of  $\text{Cr}^{3+}$  in a Sapphire Fiber," *Optics Letters*, Vol.13, No.10, 1988, pp.931-933.

- [9] The approximation that temperature/stress, concentration/stress, and concentration/temperature contributions to the frequency shift are linearly superposable has been experimentally validated [7,16,17]. Although there has been no confirmation of the superposability of the remaining terms, the assertion is expected to be an adequate first-order approximation.
- [10] McCumber, D.E. and Sturge, M.D., "Linewidth and Temperature Shift of the R Lines in Ruby," *Journal of Applied Physics*, Vol.34, No.6, 1963, pp.1682-1684.
- [11] Yen, J. and Nicol, M., "Temperature Dependence of the Ruby Luminescence Method for Measuring High Pressures," *Journal of Applied Physics*, Vol.72, No.12, 1992, pp.5535-5538.
- [12] Ragan, D.R., Gustavsen, R., and Schiferl, D., "Calibration of the Ruby R<sub>1</sub> and R<sub>2</sub> Fluorescence Shifts as a Function of Temperature from 0 to 600 K," *Journal of Applied Physics*, Vol.72, No.12, 1992, pp.5539-5544.
- [13] Warren, B.E., *X-Ray Diffraction*, Dover Publications, New York, 1990, pp.257-262.
- [14] Eshelby, J.D., "The Determination of the Elastic Field of an Ellipsoidal Inclusion, and Related Problems," *Proceedings of the Royal Society of London*, Vol.A241, No.1226, 1957, pp.376-396.
- [15] Arnold, S.M. and Wilt, T.E., "Influence of Engineered Interfaces on Residual Stresses and Mechanical Response in Metal Matrix Composites," NASA TM-105438, 1992.
- [16] Shimomura, O., Yamaoka, S., Nakazawa, H., and Fukunaga, O., "Application of a Diamond-Anvil Cell to High-Temperature and High-Pressure Experiments," *High Pressure Research in Geophysics*, S. Akimoto and M.H. Manghnani, eds., *Advances in Earth and Planetary Sciences (AEPS)*, Reidel, Boston, Vol.12, 1982, pp.49-60.
- [17] Hess, N.J. and Schiferl, D., "Pressure and Temperature Dependence of Laser-Induced Fluorescence of Sm:YAG to 100 kbar and 700°C and an Empirical Model," *Journal of Applied Physics*, Vol.68, No.5, 1990, pp.1953-60.

## MEASUREMENT OF RESIDUAL STRESSES IN SAPPHIRE FIBER COMPOSITES USING OPTICAL FLUORESCENCE

QING MA and D. R. CLARKE

Materials Department, University of California, Santa Barbara, CA 93106, U.S.A.

(Received 4 November 1992)

**Abstract**—The residual stresses in *c*-axis sapphire fibers in a  $\gamma$ -TiAl matrix and in a polycrystalline  $\text{Al}_2\text{O}_3$  matrix as a function of distance below a surface are determined. They are obtained from the shift in frequency of the characteristic  $R_2$  fluorescence line of chromium in sapphire obtained by focusing an optical probe at different depths in a sapphire fiber intersecting the surface of the composite. The method is described together with its calibration. Both the axial and radial components of the residual stress in the fiber are observed to vary over a depth of approximately the fiber diameter and are then almost independent of depth.

### 1. INTRODUCTION

When a composite material is cooled down from its fabrication temperature, thermal mismatch residual stresses develop, which can have a profound influence on the mechanical properties of the composite. For example, in many ceramic fiber reinforced metal matrix or glass matrix composites the thermal expansion coefficient of the matrix  $\alpha_m$  is considerably larger than that of the fiber  $\alpha_f$  and so large compressive stresses can develop in the fiber. The axial compressive stress creates a large stress difference between debonded and bonded regions of the interface when the material is under applied tension, facilitating interfacial crack growth [1, 2], a pre-requisite for fiber pull-out. On the other hand, the large radial compressive stress produces large friction forces in the debonded region, which retards fiber sliding and consequently shortens fiber pull-out length [2, 3]. It is therefore possible to optimize the mechanical properties of such composites by tailoring the residual stresses through appropriate processing conditions and the use of interfacial coatings [4].

Unfortunately, accurate information about the residual stresses in embedded fibers is usually unavailable since their measurement is particularly difficult. As a result, estimations based on the thermal and elastic properties of the individual material components are usually used in various analyses. This approach requires accurate knowledge of the effective temperature change  $\Delta T$ , which is usually an unmeasurable quantity, and is difficult to estimate without detailed knowledge of the stress relaxation mechanisms, especially near the interface. Furthermore, such estimates can not take into account the variations from fiber to fiber due to irregularities in coatings and interfacial roughness: details which are important in understanding individual fiber pull-out/push-

out tests. Direct measurement of the residual stresses in fibers is, in principle, possible by a variety of diffraction techniques. For instance, X-ray diffraction using ultra-fine beams can provide strain information of individual fibers. However, it suffers from having a relatively small penetration depth ( $\sim 50 \mu\text{m}$ ) [5, 6] and can therefore only measure stresses near the surface, which could be significantly different from those deeper inside the composite. Neutron scattering, whilst capable of probing fiber stresses throughout the composite [7, 8], has insufficient spatial resolution to study individual fibers or to ascertain stress distributions along the fibers.

An alternative method of measuring stresses in fibers is by using piezo-spectroscopic effects. The basis of such methods is that the characteristic luminescence lines (Raman or fluorescence) of the material shift with stress. By utilizing an optical microscope to define a probe, it is relatively easy to select regions of interest with spatial resolution of only a few microns [9] either on the surface of a composite, or if the matrix is transparent, within the composite. For example, in the case of polydiacetylene fibers embedded in an optically transparent epoxy [10], Raman spectra were collected from different positions along a fiber to obtain the stress distribution along it. Since optical spectra can be collected and analyzed with relative ease compared to most diffraction methods, such measurements can be performed routinely.

In this paper, we present a new method of measuring residual stresses in embedded transparent fibers, one that utilizes optical fluorescence, and illustrate its application to determining the residual stresses in sapphire fibers in  $\gamma$ -TiAl and  $\text{Al}_2\text{O}_3$  matrices. The theoretical basis of the fluorescence method was described in detail in an earlier work [11]. Briefly, the frequency shift of a characteristic

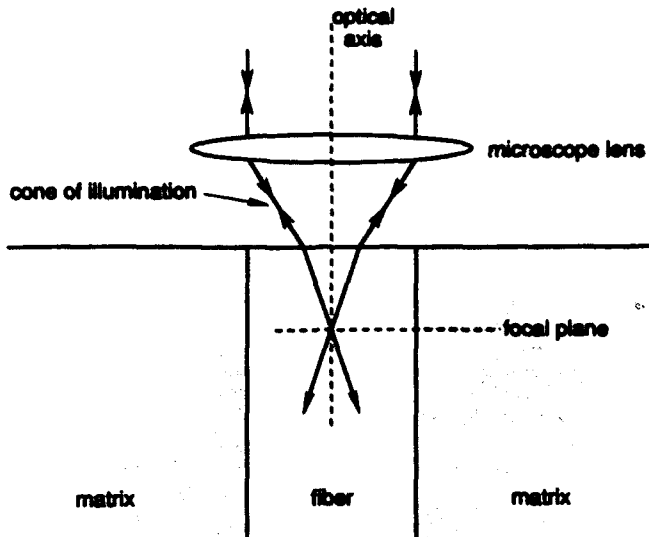


Fig. 1. Schematic diagram of the optical arrangement used to collect fluorescence from a region in an embedded, transparent fiber below its surface. The stress induced shift in frequency of a characteristic luminescence line is used to determine the stress in the probed region.

fluorescence line is stress dependent and is given by

$$\Delta\nu = \Pi_{ij}\sigma_{ij}^*$$
 (1)

where  $\Pi_{ij}$  are the piezo-spectroscopic coefficients relating frequency shift to stress, and  $\sigma_{ij}^*$  is the stress tensor represented in the crystallographic frame of reference.

The method is to use an optical microscope to focus a light beam on the end of an exposed sapphire fiber (Fig. 1), measure the frequency shift of a characteristic luminescence line and then repeat the measurement at successively deeper points of focus into the fiber. Using the lenses of the microscope to form an optical probe enables the luminescence to be collected, for any particular point of focus, from a relatively small depth of field. This facilitates high spatial resolution [12, 13] along the fiber but at the same time means that the observed frequency shifts have to be deconvoluted using a previously established calibration of the microscope convolution function (the depth of field function). This is described in the following section. Also described is a test of the accuracy of the stress profiling method in which the stress through the thickness of a ruby beam under four-point loading is measured and compared with the known elastic solution.

To illustrate the application of the technique we have measured the residual stresses in Saphikon sapphire fibers. They have sufficient levels of chromium impurity to produce sufficiently intense fluorescence lines  $R_i$  and  $R_c$  of ruby when excited by argon

ion laser. Because the fibers are single crystal with their  $c$ -axis along the fiber axis, the residual stresses inside the fibers are expected to have cylindrical symmetry. As a result, there are only two independent stress components, the radial component  $\sigma_r$  and the axial component  $\sigma_z$ . This simplifies equation (1) to be

$$\Delta\nu = 2\Pi_a\sigma_r + \Pi_c\sigma_z$$
 (2)

where  $\Pi_a$  and  $\Pi_c$  are the piezo-spectroscopy coefficients for the  $a$  and  $c$  directions. They have been measured to have values of 2.70 and  $2.15 \text{ cm}^{-1} \text{ GPa}^{-1}$ , respectively [14]. A positive shift implies tension and a negative one implies compression. In Section 3, measurements of line shifts along fibers in both  $\gamma$ -TiAl and  $\text{Al}_2\text{O}_3$  matrices as a function of depth are made. Since the frequency shifts are dependent on both the axial and radial stress components, their separation requires the solution of the appropriate elastic equations. This is described, using the results of a finite element computation in Section 4. From this, the stresses as a function of depth are determined.

## 2. THE THROUGH-FOCUS DEPTH PROFILING METHOD†

### 2.1. Depth of field function

The depth resolution of the optical microprobe used for the fluorescence measurements is determined by the numerical aperture of the objective lens and the size of the collection aperture used [12, 13]. As illustrated in Fig. 2, when the excitation laser is focused at a distance  $z$  below the top surface of a transparent material with uniform concentration of fluorescing species, only the signal generated in a small volume above and below the focal plane is

†The general procedures for optical fluorescence measurement and analysis were described in detail in [11] and therefore not included in this work.

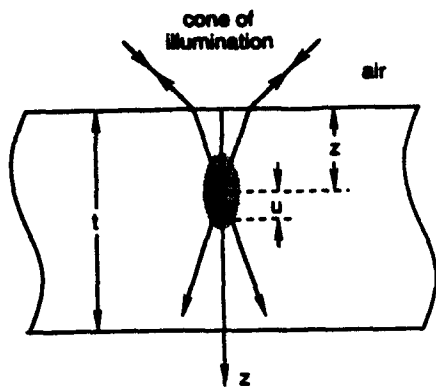


Fig. 2. Illustration of the effect of the finite depth of field of the optical system used. When the excitation laser is focused at a distance  $z$  below the top surface, only the signal generated in a small volume above and below the focal plane is effectively collected.

collected. The total signal collected is then the integral of the fluorescence from different depths

$$I(z) = \int_{-z}^{t-z} g(u) du \quad (3)$$

where  $g(u)$  is the depth of field function of the lens used to describe the relative collection efficiency as a function of  $u$ , the distance from the focal plane.

By moving the focal plane from a position above the top surface to a position below the surface of a thick sapphire disk ( $t \rightarrow \infty$ ) containing adequate chromium concentration, and recording the fluorescence line intensity as a function of depth  $z$ , the depth resolution function  $g$  is obtained from equation (3), namely

$$g(z) = \frac{dI(z)}{dz}. \quad (4)$$

The depth resolution function for our optical microprobe using a 50/0.55 objective lens and a  $50 \mu\text{m}$  collection aperture was measured using the above method and is shown in Fig. 3. As can be seen, the collection efficiency is maximum at the focal plane, and decrease rapidly with distance on either side of the focal plane.

## 2.2. Measurement of the frequency shift depth profile

We now suppose that there exists a stress field that only varies with depth  $z$ . From equation (2), the shift of a fluorescence line associated with the increment in signal from a narrow slice of material at depth  $z + u$  is

$$\Delta v(z + u) \approx 2\Pi_e \sigma_r(z + u) + \Pi_c \sigma_z(z + u). \quad (5)$$

The measured shift with focal point positioned at depth  $z$  is then a weighted average of the signals from all depths

$$\overline{\Delta v(z)} = \frac{\int_{-z}^{t-z} \Delta v(z + u) g(u) du}{\int_{-z}^{t-z} g(u) du}. \quad (6)$$

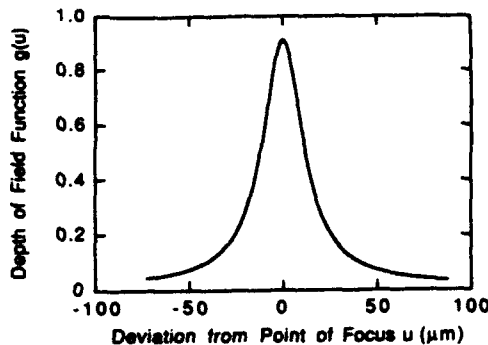


Fig. 3. The depth of field function of the microprobe used. It describes the relative collection efficiency as a function of distance from the focal plane. Details are given in the text.

Provided the depth of field function  $g(z)$  is known, the real depth profile  $\Delta v(z)$  can be deconvoluted from equation (6).

To establish that the foregoing methodology is correct, the stress field through the thickness of a dilute ruby beam in 4-point loading was measured and compared with the elastic solution for the stress. A number of fluorescence spectra were taken as the laser beam was focused at different depths from the top, tension surface to the bottom, compression surface of the beam. The measured shifts are plotted in Fig. 4 as the solid dots. The deconvoluted data is shown by the solid line. The deconvolution was obtained by assuming that the real shift  $\Delta v(z)$  is a linear function of depth  $a + bz$  since it is known that the stress distribution varies linearly with the depth  $z$  for a rectangular beam under 4-point loading. This function is then convoluted with the depth of field function  $g(z)$ . By fitting the resulting convoluted function to the measured shifts, the coefficients  $a$  and  $b$  are obtained. The initially assumed function, with the coefficients obtained by fitting, is then regarded as the deconvoluted shift  $\Delta v(z)$  directly related to the stress distributions by equation (2). The straight solid line in Fig. 4 therefore represents the real shifts. As

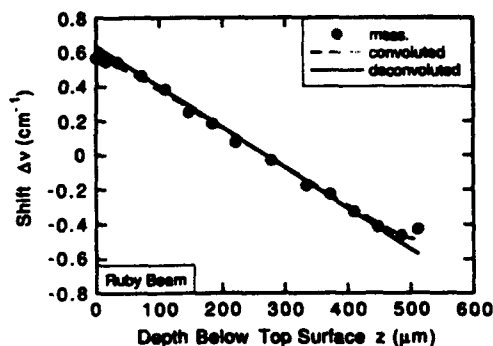


Fig. 4. The fluorescence line shift in the region between the tension surface ( $z = 0$ ) and the compression surface ( $z = 513 \mu\text{m}$ ) of a ruby beam under 4-point bending. The solid line representing the true shift is obtained by deconvoluting the measured shift with the depth of field function.

expected, and required, the zero shift position coincides with the neutral plane of the beam. The stress distribution calculated by using equation (2) is also in good agreement with that obtained from beam theory and loading conditions. As a further check, the convoluted shift, obtained by convoluting the derived values of the real shift with the instrument function  $g(z)$  is shown by the dashed curve. It has excellent fit with the measured data except for the slight deviation near the compression surface which, we believe, is due to the fact that the focus deteriorates after light has passed all the way through the ruby beam. These observations thus confirm that the through-focus method can indeed accurately measure the depth profile of the stresses.

### 3. MEASURED FREQUENCY SHIFTS FROM EMBEDDED SAPPHIRE FIBERS

The depth profiling method has been applied to two different sapphire fiber composites: the first, a  $\gamma$ -TiAl matrix composite with carbon black/alumina double fiber coatings on the sapphire fibers and, the second, a polycrystalline  $\text{Al}_2\text{O}_3$  matrix with a thin molybdenum coating on the fibers. In each case, the fiber diameter is about 120  $\mu\text{m}$ . Thin slices of composite with parallel surfaces perpendicular to the sapphire fibers were cut to about 450  $\mu\text{m}$  and 600  $\mu\text{m}$  thick for the  $\gamma$ -TiAl matrix and the  $\text{Al}_2\text{O}_3$  matrix composites respectively. The top surface of the specimens were then polished to obtain an optical finish at the fiber ends.

The measured and the deconvoluted frequency shift as a function of depth into a sapphire fiber in  $\gamma$ -TiAl matrix, as well as the convoluted function are plotted in Fig. 5. Since  $\gamma$ -TiAl has considerably larger thermal expansion coefficient than sapphire (Table I), the residual stress developed by thermal mismatch in the fiber should be compressive in both radial and axial directions. This is consistent with the large negative shifts observed when the probe is focused deep in the interior of the specimen. Near the surface, the axial stress approaches zero as required by force balance. The deconvoluted shift becomes positive near the surface indicating that the radial stress

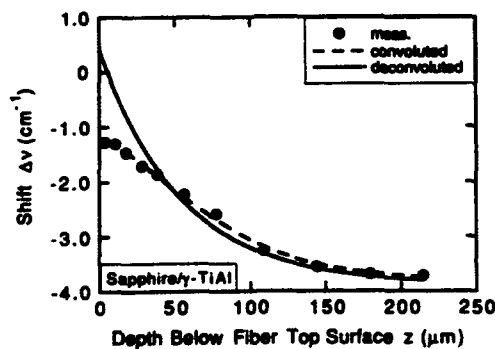


Fig. 5. The line shift depth profiles ( $z = 0$  at the surface) in a  $c$ -axis sapphire fiber embedded in the  $\gamma$ -TiAl matrix.

Table I

Property	Sapphire	$\gamma$ -TiAl	$\text{Al}_2\text{O}_3$
$E$ (GPa)	434	173	250
$\nu$	0.27	0.33	0.27
$a$ ( $10^{-6}$ /°C)	8.3(a), 9.0(c)	11-13	$8.3 < a < 9.0$

becomes tensile near the surface. In the case of the sapphire fibers in polycrystalline  $\text{Al}_2\text{O}_3$ , the residual stress is mainly caused by the anisotropy of the thermal expansion coefficient of sapphire. As shown in Fig. 6, the relatively large negative shifts near the surface indicate that the radial stress near the surface is compressive, since the axial stress must approach zero due to force balance requirement, and thus does not contribute to the shift. The magnitude of the negative shift becomes progressively smaller with increasing depth implying that the negative shift associated with radial compressive stress is partially compensated by the positive shift resulting from the build up of the axial tensile stress. These observations are consistent with the fact that the thermal expansion coefficient of polycrystalline  $\text{Al}_2\text{O}_3$  is larger than that of the sapphire in the  $a$ -direction, but smaller than that in the  $c$ -direction. A notable feature of the depth profile of the shift, in both systems, is the near exponential dependence. This is indicative of the fibers being fully bonded to the matrices and the fiber/matrix systems being elastic.

### 4. ANALYSIS

The residual stresses in the sapphire fibers are related to the observed frequency shifts presented in the previous section by equation (2). In order to obtain actual values of the two stress components, an additional relationship between the two components is evidently required. Two difficulties are associated with establishing such a relationship. First, the residual stresses originate from thermal expansion mismatch but the temperature on cooling at which stress relaxation no longer is effective, and stresses begin to build up, is not known. Secondly, existing equations relating the residual stresses in a fiber embedded in an infinite matrix [2] to the thermal mismatch strain

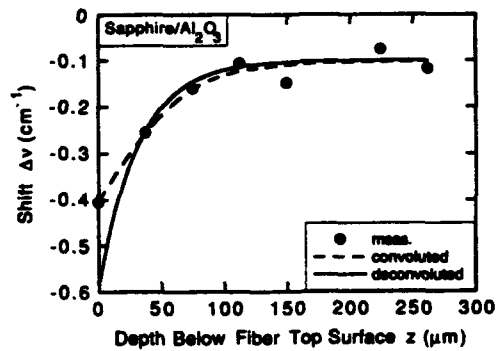


Fig. 6. The line shift depth profiles ( $z = 0$  at the surface) in a  $c$ -axis sapphire fiber embedded in a polycrystalline  $\text{Al}_2\text{O}_3$  matrix.

$\Delta\alpha\Delta T$  are unfortunately not valid for the thin specimens used in this work. Furthermore, rigorous analytical solutions for the residual stress field are not available and the approximate models used in analyzing stresses in fibers, e.g. those in analyzing fiber pull-out/push-out tests [15-17] breakdown near the fiber end. We have therefore had to resort to finite element calculations of the residual stress field for the sapphire/ $\gamma$ -TiAl and sapphire/ $\text{Al}_2\text{O}_3$  systems and use an iterative, self consistent procedure to calculate the residual stresses and the temperature at which the stresses become frozen in. This is described in the following paragraphs. First, however, it should be noted that the stresses can be estimated directly from equation (2). For the  $\gamma$ -TiAl matrix system, the residual stresses in the fiber are expected to be compressive. If it is assumed that the magnitude of the radial component is similar to the axial component in the interior of the composite, then using the shift from deep in the fiber we have from equation (2)

$$\sigma_r^{\text{int}} \sim \sigma_z^{\text{int}} \sim \frac{\Delta v^{\text{int}}}{2\Pi_e + \Pi_c} \sim 500 \text{ MPa.}$$

For the  $\text{Al}_2\text{O}_3$  matrix system, due to the anisotropy of the thermal expansion coefficient of sapphire, the fiber should be under axial tension and radial compression. If we assume that the radial compression stress is about the same in the interior and near the surface, we again can estimate that

$$\sigma_r^{\text{int}} \sim \sigma_z^{\text{int}} \sim \frac{\Delta v^{\text{int}}}{2\Pi_e} \sim -100 \text{ MPa}$$

and

$$\sigma_z^{\text{int}} \sim \frac{\Delta v^{\text{int}} - 2\Pi_e \sigma_r^{\text{int}}}{\Pi_c} \sim 200 \text{ MPa.}$$

Quantitative stress distributions can be obtained by comparing in detail the measured shifts with those calculated from the elastic field in the fiber/matrix system. Since the fiber coatings are relatively thin in both composites, we expect their effects on the elastic field to be negligible compared to those of the fiber and matrix. Therefore, in the calculations, the elastic system is simplified as consisting solely of an isotropic matrix of modulus  $E_m$  and Poisson's ratio  $v_m$  and a fiber of modulus  $E_f$  and Poisson's ratio  $v_f$  (Table I). The specimen was represented by a thin disk of the same thickness as the corresponding specimen with one cylindrical fiber sitting at the symmetry axis. The diameter of the disk was chosen to be about ten times that of the fiber in order to be consistent with the low fiber volume fraction of both composite systems. The thermal expansion coefficients of the sapphire fiber in both the radial direction  $\alpha_r$  and axial direction  $\alpha_z$  are also listed in Table I. The mean thermal expansion coefficient for  $\gamma$ -TiAl is known to be  $11-13 \times 10^{-6}/^\circ\text{C}$  depending on the stress frozen-in temperature. However, that of the polycrystalline  $\text{Al}_2\text{O}_3$  is expected to vary from sample to sample depending on the residual matrix porosity. As a result of the complicated

stress relaxation processes that occur during cooling, particularly near the interface, the effective thermal expansion coefficient  $\alpha_m$  for both matrices and the effective temperature change  $\Delta T$  were adjusted in the computation to obtain the best agreement with the experimental frequency shift data. The following procedure was adopted. First, reasonable estimates for the matrix thermal expansion coefficient and temperature change  $\alpha_m^{\text{est}}$  and  $\Delta T^{\text{est}}$  were used in the finite element calculation. The resulting stresses  $\sigma_r^{\text{est}}(z)$  and  $\sigma_z^{\text{est}}(z)$  were then used in equation (2) to calculate the shift as a function of  $z$ ,  $\Delta v_{\text{cal}}^{\text{est}}(z)$ . This function and the measured shifts are then normalized by their values in the interior of the material

$$\Delta v^{\text{norm}} = \frac{\Delta v}{\Delta v^{\text{int}}}. \quad (7)$$

By comparing the calculated and measured normalized shifts for a series of values of  $\alpha_m^{\text{est}}$ , the value that gives the best agreement is considered as the true  $\alpha_m$ . Then, by requiring that the calculated shift be equal to the measured shift in the interior, the effective temperature difference is proportionally scaled

$$\Delta T = \Delta T^{\text{est}} \frac{\Delta v_{\text{meas}}^{\text{int}}}{\Delta v_{\text{cal}}^{\text{int}}}. \quad (8)$$

Finally, the stress distributions are obtained

$$\sigma_r = \sigma_r^{\text{est}} \frac{\Delta T}{\Delta T^{\text{est}}} \quad (9)$$

$$\sigma_z = \sigma_z^{\text{est}} \frac{\Delta T}{\Delta T^{\text{est}}}.$$

Since the thermal expansion coefficient of  $\gamma$ -TiAl is considerably larger than  $\alpha_e$  and  $\alpha_z$  of sapphire, the difference between  $\alpha_e$  and  $\alpha_z$  was unimportant. As a result, it was observed that the fitting of the normalized shift was not sensitive to the actual value of  $\alpha_m$ . Figure 7 illustrates the fitting between the measured and the calculated normal shifts for  $\alpha_m = 12$ . The effective temperature drop  $\Delta T$  calculated from equation (8) is  $\sim 750^\circ\text{C}$ , which agrees with  $\alpha_m - T$  curve for  $\gamma$ -TiAl [18]. This temperature change is about  $300^\circ\text{C}$  smaller than the difference between the

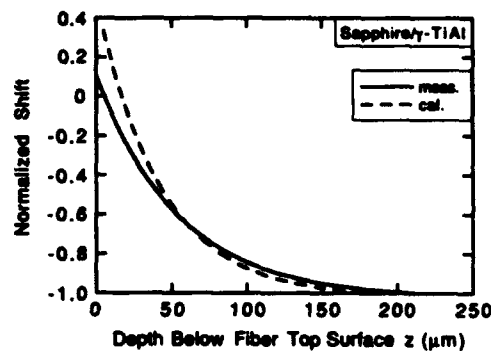


Fig. 7. A comparison of the calculated and the measured normalized shifts as a function of depth for the sapphire/ $\gamma$ -TiAl system.

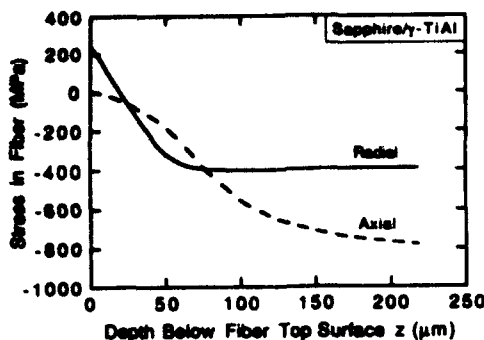


Fig. 8. The radial and axial stresses as a function of depth in the sapphire/γ-TiAl system determined from the fluorescence data.

processing temperature and the room temperature indicating significant stress relaxation occurring during cooling. The stress distributions along the fiber calculated from equation (9) are plotted in Fig. 8. The axial stress approaches zero as expected and the radial component is positive at the surface as was indicated by the frequency shift measurement. The differences between the calculated and the measured normalized shifts as shown in Fig. 7 are due to the simplifications used in the model, e.g. neglecting the effects of coatings and assuming perfect interfacial bonding. However, the finite element calculations show that the stress distributions in the interior of the specimen are not sensitive to small changes in the value of the elastic modulus and the thermal expansion coefficient of the matrix. This is because the values of the stresses are bounded by the measured shifts through equation (2) and scaled by equations (8) and (9). These observations suggest that the stress distributions deduced from the fluorescence data and illustrated in Fig. 8 are relatively accurate especially in the interior of the specimen. The possibility of some interfacial debonding will be discussed in more detail in the next section.

As expected, the normalized shift calculated for the Al<sub>2</sub>O<sub>3</sub> matrix system depends much more sensitively on the value of  $\alpha_m$  used in the computation. As shown in Fig. 9,  $\alpha_m = 8.73$  gives the best fit between the calculated and the measured normalized shifts. The effective temperature difference obtained using equation (8) is about 1300°C, which is about 200°C lower than the processing temperature again as indication of stress relaxation occurring during cooling. The stress distributions in the sapphire fiber are plotted in Fig. 10. The observation that the calculated stress distributions in the interior are not sensitive to changes of  $E_m$  also applies in this system. The values of stress in the interior differ less than 5% for the three  $\alpha_m$ 's shown in Fig. 9. Since the shape of the shift profile depends sensitively to the change of  $\alpha_m$ , the fitting in Fig. 9 also provides means of estimating the local thermal expansion coefficient of the Al<sub>2</sub>O<sub>3</sub> matrix, which could be different from the average

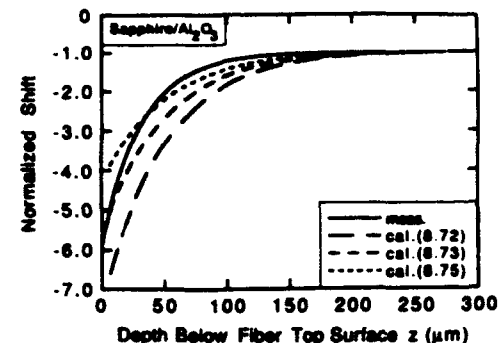


Fig. 9. A comparison of the calculated and the measured normalized shifts as a function of depth for the sapphire/Al<sub>2</sub>O<sub>3</sub> system.

value of the whole sample because the density of the matrix is slightly lower near the fibers. The resulting value of  $\alpha_m$  can then be used in other analyses, such as for push-out tests.

### 5. DISCUSSION

The analysis in the last section is based on the assumption that the fiber/matrix systems are elastic without any debonding occurring at the interface. This requires that the interfacial shear strength be larger than the maximum interface shear stress. To examine this assumption, the interfacial shear stress is also calculated in the finite element computation. The results corresponding to the best fit conditions determined in the last section are plotted for the sapphire/γ-TiAl and the sapphire/Al<sub>2</sub>O<sub>3</sub> systems in Fig. 11. In both systems, the magnitude of the shear stress has a maximum at the surface and decreases to zero with increasing depth. This is expected from the stress distributions in Figs 8 and 10 and the force balance requirement

$$\tau = \frac{R_f d\sigma_z}{2 dz}. \quad (10)$$

Whilst the calculated interfacial shear stress for the sapphire/Al<sub>2</sub>O<sub>3</sub> system is smaller than the interfacial

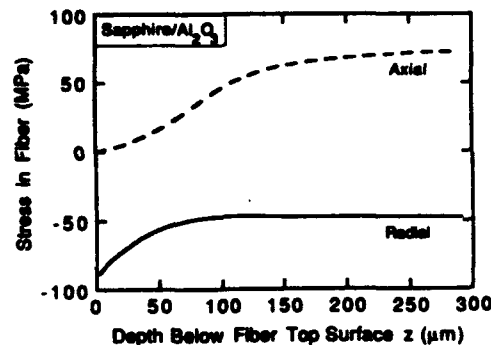


Fig. 10. The radial and axial stresses as a function of depth in the sapphire/Al<sub>2</sub>O<sub>3</sub> system determined from the fluorescence data.

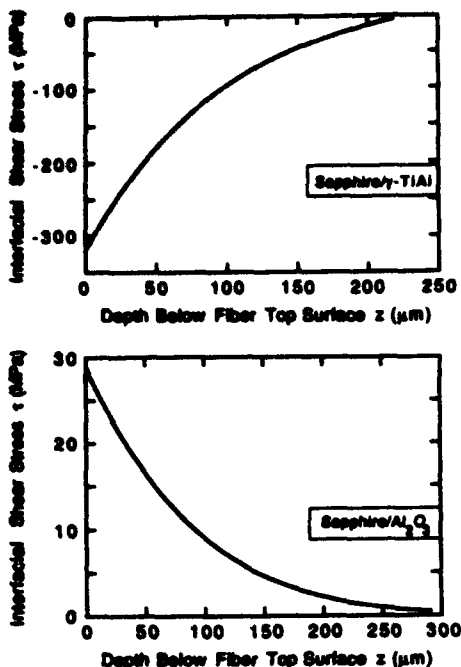


Fig. 11. The interfacial shear stresses in the sapphire/γ-TiAl and the sapphire/Al<sub>2</sub>O<sub>3</sub> systems calculated from the finite element computation and the fluorescence data.

shear strength for the molybdenum/sapphire interface ( $\sim 100\text{--}300$  MPa) [19] and therefore insufficient to produce any debonding, the shear stress calculated for the sapphire/γ-TiAl system is considerably larger than any reasonable value for the carbon/sapphire interface ( $\sim 100\text{--}150$  MPa) [4, 18]. It is likely that the thin carbon coating on this fiber is not continuous so that the sapphire fiber has direct contact with the polycrystalline Al<sub>2</sub>O<sub>3</sub> outer coating to form a strongly bonded interface. This has been often observed in the same composite specimen during push-out tests [18]. As mentioned in the last section, the fitting between the calculated and measured frequency shifts near the surface is not perfect. As shown in Fig. 7, the calculated shift changes more rapidly than that measured within one fiber diameter from the surface. Therefore, the change of the axial stress and consequently the magnitude of the interfacial shear [equation (10)] in the real system should be smaller than that calculated. This further suggests that the interface may be debonded for a distance about one fiber diameter from the surface. However, this debonding does not seem to change the stress field significantly, so that the fiber/matrix system still behaves in an elastic manner. This is consistent with the fact that the friction is sufficiently large in this system, due to asperities at the interface [4, 20], that the stress distribution is similar to a system with a perfect bonding [3]. Therefore, we believe that the residual stresses determined for the sapphire/γ-TiAl system, especially in the interior of the composite, are

not significantly affected by possible debonding near the surface.

## 6. CONCLUSIONS

By utilizing the optical fluorescence from chromium impurities in sapphire fibers, we have determined the residual stress distributions in embedded fibers in both a γ-TiAl matrix and a polycrystalline Al<sub>2</sub>O<sub>3</sub> matrix composite. The axial and radial components of the residual stress, produced by differential thermal contraction on cooling after fabrication, in the fibers are determined as a function of depth below the composite surface. For both composites, the two stress components vary over a distance of about the fiber diameter from the surface and then are almost independent of distance further into the composite.

**Acknowledgements**—This work was supported by the Office of Naval Research under grant N00014-91-J-1875 (QM) and the DARPA URI program at UCSB under contract N00014-92-J-1808 (DRC). The authors are grateful to Dr T. J. Mackin and J. Davis, UCSB, for providing the composite samples used in this work.

## REFERENCES

- J. W. Hutchinson and H. M. Jensen, *Mech. Mater.* **9**, 139 (1990).
- R. J. Kerans and T. A. Parthasarathy, *J. Am. Ceram. Soc.* **74**, 1585 (1991).
- K. T. Faber, S. H. Advani, J. K. Lee and J. T. Jinn, *J. Am. Ceram. Soc.* **69**, C-208 (1986).
- T. J. Mackin, J. Y. Yang, C. G. Levi and A. G. Evans, *Mater. Sci. Engng.*, in press.
- P. Predecki, A. Abuhassan and C. S. Barrett, *Adv. X-ray Anal.* **31**, 231 (1988).
- A. Abuhassan, C. Balasingh and P. Predecki, *J. Am. Ceram. Soc.* **73**, 2474 (1990).
- S. Majumdar, D. Kupperman and J. Singh, *J. Am. Ceram. Soc.* **71**, 858 (1988).
- A. J. Allen, M. A. M. Bourke, S. Dawes, M. T. Hutchings and P. J. Withers, *Acta metall. mater.* **40**, 2361 (1992).
- S. E. Molis and D. R. Clarke, *J. Am. Ceram. Soc.* **73**, 3189 (1990).
- I. M. Robinson, R. J. Young, C. Gallois and D. N. Batchelder, *J. Mater. Sci.* **22**, 3642 (1987).
- Q. Ma and D. R. Clarke, *J. Am. Ceram. Soc.*, in press.
- M. Pluta, *Advanced Light Microscopy I*. Elsevier, Amsterdam (1988).
- F. Adar and D. R. Clarke, in *Microbeam Analysis* (edited by K. F. J. Heinrich), pp. 307–310. San Francisco Press, San Francisco (1982).
- R. G. Munro, G. J. Piermarini, S. Block and W. B. Holzapfel, *J. appl. Phys.* **57**, 165 (1985).
- A. Takaku and R. G. C. Arridge, *J. Phys. D* **6**, 2038 (1973).
- D. K. Shetty, *J. Am. Ceram. Soc.* **71**, C-107 (1988).
- Y. C. Gao, Y. W. Mai and B. Cotterell, *J. appl. Math. Phys.* **39**, 550 (1988).
- T. J. Mackin, private communication.
- J. Davis and A. G. Evans, to be published.
- T. J. Mackin, P. D. Warren and A. G. Evans, *Acta metall. mater.* **40**, 1251 (1992).

*Luminescence Sensing of Stress  
in Ti/Al<sub>2</sub>O<sub>3</sub> Fiber Reinforced Composites*

**H. Hough, J. Demas<sup>1</sup>, T. O. Williams<sup>2</sup> and H. N. G. Wadley**

**Department of Materials Science and Engineering  
University of Virginia  
Charlottesville, VA 22903**

- (1) Department of Chemistry**
- (2) Department of Civil Engineering**

### *Abstract*

The high temperature processing of fibrous metal matrix composites has been predicted to result in the development of large residual stresses because of a difference between the coefficients of thermal expansion (CTE) of the fibers and matrix. Efforts to measure the stresses and verify this explanation for their development have been hampered by the lack of a convenient measurement methodology. We have used a fiber optically coupled method to measure both the R1 and R2 optical luminescence line shifts of single crystal  $\alpha\text{-Al}_2\text{O}_3$  fibers embedded in a CP titanium matrix composite. The line shifts depend linearly upon weighted sums of the fiber's principle stresses, and we find the average measured shifts for all the fibers in a composite sample to be roughly in agreement with concentric cylinder residual stress model predictions. However, significant fiber to fiber variability is also observed. Using both the R-line measurements and the constraining relation that within the fiber the radial and hoop stresses are equal, we have been able to independently estimate the fiber's axial and radial stress components. The axial stress is found to be more than twice that predicted by a CTE difference model, whilst the radial (and hoop) direction stresses are smaller than expected. We propose that the stress in these composites is affected by two presently unmodelled effects: an elevation of composites residual stress due to the CTE difference between the tooling used for (hot isostatic) processing of the composite, and a relaxation of the transverse stress components for some fibers by radial matrix cracking. The result has important consequences for the manufacture of metal matrix composites and for efforts to predict their mechanical properties.

## 1.0 Introduction

Metal matrix composites (MMC's) reinforced with continuous ceramic fibers have been the subject of much recent research and development due to their favorable combination of mechanical properties (e.g., high specific stiffness, ambient and high temperature strength, etc.) [1]. These traits, together with potentially superior creep resistance, make this class of materials promising candidates for high temperature structural applications such as aircraft engines or the leading edges of proposed hypersonic vehicles [2,3]. Several issues must, however, be resolved before MMC's can be put into high temperature service. One, of interest here, relates to the usually large residual stress that forms on cooling from the high temperatures used for composite processing and/or during the thermal cycling that accompanies their subsequent use [3].

It is normally assumed that thermal stresses arise in MMC's because of a coefficient of thermal expansion (CTE) mismatch between a composite's matrix and fiber. Because the fibers exhibit a lower CTE than the matrix, they impede matrix contraction near the fiber surface on composite cooling, resulting in the development of stress both in the fiber and the surrounding matrix. For some fiber-matrix systems, the CTE difference can be a factor of two or more, and the matrix stresses are sufficiently large that they exceed the matrix yield strength, or, in less ductile materials, its fracture strength resulting in matrix plasticity and/or radial and axial matrix cracking on cooling [1,2,3].

These internal stresses and their associated damage can be responsible for premature failure in service, and are a significant source of quality loss during manufacturing. Even in the event that the thermal stresses alone are not large enough to cause damage on first cooling, the thermal component adds to that applied mechanically during thermal-mechanical cycling and results in a short

thermomechanical fatigue life [3]. Understanding, measuring, and learning how to minimize these thermal stresses is essential as we seek reliable ways of manufacturing MMC's and extending their high temperature capability.

Many models have been proposed for calculating the residual stresses of MMC's due to the CTE mismatch [2,7-9]. They range from the simplest: an elastic analysis of two concentric cylinders [7], up to the finite-element method using a matrix constitutive behavior that includes both elastic and the inelastic deformation due to matrix plasticity and creep [8]. Recently, Pindera and Freed have developed an elastic-plastic multiple concentric cylinders model capable of calculating both fiber and matrix stresses [9]. It has been implemented on a personal computer allowing the rapid convenient calculation of stresses.

Figure 1 schematically shows a Pindera and Freed model predicted stress field in and around a single crystal aluminum oxide fiber embedded in a titanium matrix after cooling from a stress-free (processing) temperature of 900°C. (The assumptions and physical properties used to make this calculation are presented later.) We note that the model predicts (1) the stress components in the fiber are all compressive, (2) the fiber's hoop ( $\sigma_{\theta\theta}^f$ ) and radial ( $\sigma_{rr}^f$ ) stresses are equal, (3) the fiber's axial stress is significantly larger than its other components, (4) the matrix hoop ( $\sigma_{\theta\theta}^m$ ) stress is equal in magnitude but of opposite sign to that of the fiber, and (5) none of the fiber's stress components vary with position in the fiber, whereas both the matrix radial and hoop stresses decay with distance from the fiber-matrix interface.

It has been difficult to experimentally verify these models and to confirm that the fiber/matrix CTE difference is the explanation for residual stress development. X-ray diffraction can be used to measure residual strains in the matrix (by detecting the change in lattice parameter), but x-rays normally penetrate only a few microns in metals, so it is necessary to remove successive

layers of material from the surface (measuring the strains at each newly created surface) in order to measure the strain as a function of position in the composite [1]. However, removing layers is both destructive and changes the strains at the newly created free surface. Substituting neutrons for x-rays solves the penetration and sample destruction problems, but requires a volume large enough ( $10\text{-}30 \text{ mm}^3$ ) to provide sufficient diffracted neutron intensity to reliably detect the small diffraction peak shifts due to strain [11]. Since the strain measured by this method is an average over the probe volume, it does not provide information about the matrix stresses as a function of position near fibers. Energy dispersive x-ray diffractometry [12], which uses high energy synchrotron x-radiation instead of neutrons, has the needed penetration capability, reasonable spatial resolution ( $\sim 50 \mu\text{m}$ ) and precision ( $\pm 50 \text{ MPa}$ ) provided the matrix grain size is small ( $< 10 \mu\text{m}$ ), and has been used to measure matrix stress in SCS-6 reinforced  $\text{Ti}_3\text{Al}+\text{Nb}$  alloys. However, neither Neutron or Synchrotron diffraction techniques are convenient solutions to the measurement problem because most researchers do not have convenient access to these facilities, nor the resources to mount, what quickly becomes, a very significant measurement campaign. Thus, there still exists a need for a convenient, accurate method for measuring residual stresses deep within metal matrix composites.

Ma and Clarke [13] and Hough, et al [14] have sought to exploit the natural luminescence of  $\alpha\text{-Al}_2\text{O}_3$  fibers in order to do this.  $\alpha\text{-Al}_2\text{O}_3$  of the purity used for composite fibers (both single and polycrystalline forms) contain sufficient chromium that a detectable optical luminescence can be observed following illumination with green wavelength light. In composite grade single crystal fibers, Hough, et al [14] have shown that reasonably efficient light piping occurs, and thus luminescence can potentially be excited and detected from deep within the composite using fiber optic methods of coupling. The luminescence

peak wavelength (which can be precisely measured with a modern spectrometer) depends linearly upon a weighted combination of the stress components in the fiber, and since the fiber stress is in mechanical equilibrium with that of the matrix, a measurement of the luminescence line shift affords the opportunity to infer the matrix residual stress. However, care must be taken with luminescence measurements and their interpretation because factors other than stress (e.g. temperature) can affect the measured line shift.

Here we review the underlying mechanisms responsible for the luminescence of Cr(III) doped (to intensify the luminescent response)  $\alpha\text{-Al}_2\text{O}_3$ , and identify the best values for the (piezospectroscopic) constants that relate the luminescence line shift to stress, and other factors that are responsible for (anomalous) line shifts due to temperature and chromium ion concentration variations. The design of a fiber optically coupled spectroscopic system with sufficient peak position resolution for residual stress measurement is next described. We then explain our composite fabrication method for producing samples with embedded Cr(III) doped single crystal  $\text{Al}_2\text{O}_3$  fibers. The measured peak shifts for the fibers in the "as processed" condition are compared with those predicted from fiber stresses calculated using the Pindera-Freed thermal stress model, and the validity of the model's predictions for realistic MMC's discussed. It will be shown that the containment used to consolidate composites introduces a large additional residual stress in composite components that is not included in the current models, and this could adversely affect composite quality.

## 2.0 Principles of Luminescence

### 2.1 Luminescence in the Cr(III) Doped Al<sub>2</sub>O<sub>3</sub> System

Luminescence arises from the radiative (emission of a photon) transition between two energy states of an atomic or molecular system. The conditions for luminescent emission are rather stringent and only a relatively small percentage of molecules luminesce. The two types of luminescence (fluorescence and phosphorescence) are characterized by the multiplicities of the ground and the emitting states. Fluorescence is characterized by initial and final states of the same multiplicity, and the transition is thus not forbidden by spin selection rules. It is a "highly allowed" and therefore a short lived process (typically requiring only nanoseconds to depopulate the excited state). Phosphorescence, on the other hand, involves a spin flip or change of multiplicity between the excited and ground states. Formally, such transitions are forbidden, but in practice, various mechanisms relieve the forbiddenness of the transition and make it somewhat allowed. This forbiddenness causes phosphorescence to have a long lifetime (i.e., a long time is required to depopulate the excited state) ranging from hundreds of microseconds to even seconds. The free Cr(III) ion (with three outer d electrons designated d<sup>3</sup>) has a quartet ground state and quartet and doublet excited states. For this case fluorescence accompanies the quartet-quartet process and phosphorescence is seen from the doublet-quartet transition.

The incorporation of Cr(III) in the near octahedral sites of the  $\alpha$ -Al<sub>2</sub>O<sub>3</sub> (trigonal symmetry) lattice is responsible for the luminescence of aluminum oxide fibers. The octahedral crystal field of the unstrained lattice splits the 5-fold degenerate d-orbitals of the free ion, into a (lower energy) 3-fold degenerate t<sub>2g</sub> orbital and an upper e<sub>g</sub> orbital. The notation, from group theory, is for an octahedral point group, where the "g" subscript denotes an orbital that is

symmetric with respect to inversion (gerade); all d-electron derived excited states will be g in a centrosymmetric point group. The d<sup>3</sup>-electrons of Cr(III) occupy the three t<sub>2g</sub> orbitals in the unstrained lattice.

The description of the optical spectroscopy of ruby builds on the orbital and state diagram of an ion in such an octahedral site, Figure 2 [15]. This d<sup>3</sup> configuration gives rise to a <sup>4</sup>A<sub>2g</sub> ground state. Excited states arise from spin flips within the t<sub>2g</sub> orbital and promotions with or without spin flips of a t<sub>2g</sub> to an e<sub>g</sub> orbital. The excited t<sub>2g</sub> configuration yields doublet excited states including a <sup>2</sup>E<sub>g</sub> state, which is the lowest excited state in the ion; ruby phosphorescence arises from the <sup>2</sup>E<sub>g</sub> → <sup>4</sup>A<sub>2g</sub> transition. Since this transition is formally spin forbidden, the ruby phosphorescence is also forbidden and is therefore long-lived (several milliseconds). Similarly, direct absorption to this state (<sup>2</sup>E<sub>g</sub> ← <sup>4</sup>A<sub>2g</sub>) is forbidden, and the transition is too weak to be optically pumped effectively. Two quartet excited states (<sup>4</sup>T<sub>1g</sub> and <sup>4</sup>T<sub>2g</sub>) arising from the t<sub>2g</sub><sup>2</sup>e<sub>g</sub> configuration give rise to allowed absorptions (<sup>4</sup>T<sub>1g</sub> ← <sup>4</sup>A<sub>2g</sub> and <sup>4</sup>T<sub>2g</sub> ← <sup>4</sup>A<sub>2g</sub>) (shown as shaded regions in Figure 2). These allowed transitions occur in the blue and green parts of the spectrum and give ruby its red color. They absorb intensely enough to be pumped efficiently by a variety of lasers including ionized Ar, HeCd, and green HeNe. Once excited, the <sup>4</sup>T<sub>1g</sub> and <sup>4</sup>T<sub>2g</sub> states decay nonradiatively with unit efficiency to the lower <sup>2</sup>E<sub>g</sub> state, which then emits the luminescence of interest with near 100% quantum efficiency.

In reality, the picture is a little more complicated than presented above. The Cr(III) ion is located in an octahedral lattice site with a slight trigonal distortion. The notation for its energy levels must then switch to that used for spin orbit states in a noncentrosymmetric trigonal crystal field. This distortion, together with spin-orbit coupling, splits the <sup>2</sup>E<sub>g</sub> state into an  $\overline{E}$  and a  $2\overline{A}$  state separated in wavenumber (energy) by about 30 cm<sup>-1</sup>. The  $\overline{E}$  and  $2\overline{A}$  states

give rise to a doublet in the phosphorescence spectrum, designated R1 and R2. In the absence of an externally imposed lattice strain, these states are  $14400\text{ cm}^{-1}$  and  $14430\text{ cm}^{-1}$  above the ground state [15]. Decay, via radiative transitions, thus results in luminescence with two spectral lines (the R1 and R2 lines, respectively) with wavelengths of approximately 693 nm and 694 nm (Figure 2).

## 2.2 Luminescence and Stress

Schawlow [16], during development of the first ruby lasers, was the first to observe that a compressive stress altered both the R peak positions, and subsequently was able to predict this phenomenon using a quantum mechanics approach [17, 18]. At about the same time, Forman et al at the Institute of Standards and Technology (formerly the National Bureau of Standards) also observed a systematic change in the emission wavelength with pressure from a small ruby chip placed in a diamond anvil cell (DAC) used for studies of high pressure phase equilibria [19, 20]. The NBS group examined the responses of many other luminescing crystals and determined that the very intense peak emission, low background intensity, and moderate line width of the ruby signal made it the best material for measuring stress [20]. They calibrated the hydrostatic stress-wavelength relationship of the R1 line up to 20 GPa and reported it to be linear [21]. Bell et al have extended the calibration to 550 GPa in order to measure the pressure in DAC's of improved design [22-24]. They reported that the calibration only exhibited measurable nonlinearities for pressures above 29 GPa [24]. (Recent unpublished studies by Clarke, et al indicate a small nonlinearity may be present in the R1 peak shift for stresses less than 3GPa.)

The fibers in a composite are not under purely hydrostatic loading. Grabner [25] has developed a relationship between the tensor components of stress in a multiaxially loaded crystal to the scalar line shift:

$$\Delta\bar{v} = \Pi_{ij}\sigma_{ij}^c \quad (1)$$

where  $\Delta\bar{v}$  is the line shift due to the application of stress (in  $\text{cm}^{-1}$ ),  $\sigma_{ij}^c$  is the applied stress defined in the crystal coordinates, and  $\Pi_{ij}$  are the components of the crystal's piezospectroscopic coefficient tensor. This can be rewritten in terms of principle applied stresses using the standard transformation convention:

$$\sigma_{ij}^c = a_{im}\sigma_{mn}a_{jn} \quad (2)$$

where  $a_{im}$  and  $a_{jn}$  are coordinate transformation matrices and  $\sigma_{mn}$  is the stress tensor in the coordinates of the principle applied stresses. Applying (1) and (2) to a residually stressed ruby fiber like that in Fig. 1 with its c-axis aligned with the  $\sigma_{zz}$  (axial) principle stress yields:

$$\Delta\bar{v} = \Pi_{11}(\sigma_{rr} + \sigma_{\theta\theta}) + \Pi_{33}\sigma_{zz} \quad (3)$$

Schawlow, et al [16, 17] reported that  $\Pi_{11}$  and  $\Pi_{33}$  for the R1 line have values of  $3.0 \text{ cm}^{-1}\text{GPa}^{-1}$  and  $1.8 \text{ cm}^{-1}\text{GPa}^{-1}$ , respectively. Different values of the  $\Pi_{ij}$  for the R1 peak shift have since been reported and these, together with the piezospectroscopic constants for the R2 line, are summarized in Table 1. The values presented in Table 1 were first measured by Schawlow in 1961 [17], and shortly thereafter (1962) by Kaplyanskii and Przhevuskii [26]. Feher and Sturge [27] later reported average (i.e.  $[R1 + R2]/2$ ) values that were lower than the separate R1, R2 values of other studies. Recently Lipkin and Clarke have reported new measurements of piezospectroscopic constants [28, 29] that are similar to those of [26].

**Table 1: Values of  $\Pi_{11}$ ,  $\Pi_{33}$  and hydrostatic loading constants reported by various studies.**

Source	Piezospectroscopic Coefficient					
	$\Pi_{11}$ (cm <sup>-1</sup> /GPa)		$\Pi_{33}$ (cm <sup>-1</sup> /GPa)		$2\Pi_{11} + \Pi_{33}$ (cm <sup>-1</sup> /GPa)	
	R1	R2	R1	R2	R1	R2
Schawlow [17]	3.0	2.8	1.8	2.3	7.8	7.9
Kaplyanskii/Przhevuski [26]	3.2	2.8	1.4	1.9	7.8	7.5
Lipkin & Clarke, et al [28, 29]	3.5	2.8	1.5	2.1	8.4	7.6
Feher and Sturge [27]		2.7		2.15		7.55

It is interesting to note that if line shifts for the R1 and R2 peaks are accurately measured, and the  $\Pi_{ijj}$  values for the two R lines are sufficiently different (and accurately known) one could construct two equation (3)'s and use the constraining relation  $\sigma_{rr} = \sigma_{\theta\theta}$  in the fiber to independently calculate  $\sigma_{zz}$  and  $\sigma_{rr}$  ( $= \sigma_{\theta\theta}$ ).

Using a Raman microprobe measurement system [30], Ma and Clarke have recently reported a stress variation close to the polished surface of a sapphire fiber embedded both in poly-crystalline alumina and  $\gamma$ -TiAl [13]. They were able to confirm Liang and Hutchinson's recent prediction [31] that the residual stress in the fiber (for fibers oriented perpendicular to the free surface) is significantly perturbed near the sample's free surface because of the traction-free conditions at the newly created free surface. They observed that the axial component of the fiber stress decreases from the bulk value at about a fiber diameter below the surface, to zero at the free surface. They also found that the radial stress varied strongly along the fiber length, and even became tensile within about 25  $\mu\text{m}$  (a fifth of the fiber diameter) of the fiber surface end. Thus, if measurements of interior stresses are to be obtained with a fiber optic coupling approach, it is

important that the interrogated fiber have reasonably good light piping capabilities and that care is taken to efficiently couple (align) with the interrogated fiber so that guided optical wave modes are excited, and the resulting luminescence excited originates from deep within the composite.

### 2.3 Temperature Effects

The R lines of ruby are also shifted by temperature. Recent reports of the temperature effect have been made in the context of the DAC. Wunder and Schoen [32] report that the wavenumber shift of the R1 peak due to applied stress has a linear temperature dependence of  $-0.149 \text{ cm}^{-1}/^\circ\text{C}$  near room temperature. It is usually assumed that stress and temperature shifts are additive, thus equation (3) becomes:

$$\Delta\bar{v} = \Pi_{11}(\sigma_{11} + \sigma_{22}) + \Pi_{33}\sigma_{33} - 0.149(T_{\text{str}} - T_{\text{ref}}) \quad (4)$$

where  $T_{\text{ref}}$  is a reference temperature (e.g.,  $25^\circ\text{C}$ ) and  $T_{\text{str}}$  is the temperature of the stressed sample when its line shift was measured.

More recent work by Munro et al [33], has thoroughly addressed the issue of accurate R1 and R2 peak position determination for hydrostatic loading when the measurement temperature also varies. They propose that the peak positions are given by:

$$\bar{v}_k = \alpha_{k1} + \alpha_{k2}P + \alpha_{k3}(T - T_{\text{ref}}) \quad (5)$$

where  $\bar{v}_k$  is the peak position ( $\text{in cm}^{-1}$ )  $k=1,2$ , represents the R1 and R2 peaks,  $\alpha_{ki}$ , with  $i=1-3$ , are constants for the two R peaks, and P and T are the hydrostatic pressure and sample temperature, respectively. Table 2 lists the  $\alpha_{ki}$  constants proposed by Munro et al.

**Table 2: Constants  $\alpha_{ki}$  proposed by Munro's et al for hydrostatic loading [33].**

Peak	$\alpha_{k1} (\text{cm}^{-1})$	$\alpha_{k2} (\text{cm}^{-1}/\text{GPa})$	$\alpha_{k3} (\text{cm}^{-1}/\text{K})$
R1	$14402.5 \pm 0.4$	$-7.59 \pm 0.04$	$-0.130 \pm 0.006$
R2	$14432.1 \pm 0.4$	$-7.615 \pm 0.004$	$-0.122 \pm 0.006$

Hence, the change in peak position between a strained ( $\bar{v}^s$ ) and unstrained ( $\bar{v}^0$ ) sample when the measurements are made at different temperatures (provided  $T_{\text{ref}}$  is the same for the stressed and unstressed measurements) is:

$$\begin{aligned}\Delta\bar{v} = \bar{v}_k^s - \bar{v}_k^0 &= \alpha_{k2}(p_{\text{str}} - p_0) + \alpha_{k3}[(T_{\text{str}} - T_{\text{ref}})(T_{\text{unstr}} - T_{\text{ref}})] \\ &= \alpha_{k2}(p_{\text{str}} - p_0) + \alpha_{k3}(T_{\text{str}} - T_{\text{unstr}})\end{aligned}\quad (6)$$

where  $p_{\text{str}}$  is the pressure in the stressed sample,  $p_0$  is the pressure in the "unstressed" sample,  $T_{\text{str}}$  is the temperature of the stressed sample, and  $T_{\text{unstr}}$  is the temperature of the unstressed piece, and the  $\alpha_{k2}(p_{\text{str}} - p_0)$  term would be equivalent to equation (3). Note equation (6) indicates that for  $T_{\text{str}} - T_{\text{unstr}} = -0.5^\circ\text{C}$  there would be a temperature adjustment to the line shift of only  $-0.06 \text{ cm}^{-1}$ , which is on the order of other experimental errors.

## 2.4 Chromium Concentration Effects

There is also a shift in R peak position with chromium ion concentration when the temperature and applied stress are both held constant [34]. It has been found that the line shift data fit an equation of the form:

$$\Delta\bar{v} = 99[\text{Cr}] \quad (7)$$

where  $\Delta\bar{v}$  is the line shift (in  $\text{cm}^{-1}$ ) and  $[\text{Cr}]$  is the chromium concentration (in weight percent). Ma and Clarke [13] have examined the fundamental origin of this relation and conclude that it arises from the strain field created by substituting a Cr(III) ion for an Al atom in the  $\alpha\text{-Al}_2\text{O}_3$  lattice. Because the

dilational strain sensed by luminescence is only a third of that measured by x-ray diffraction, they argue that it is the "image" component of the Cr(III) strain field that is responsible for the concentration dependent frequency shift.

The practical consequence of this is that for a system in which there is a difference in stress, temperature, and concentration between measured and reference states, the observed shift in R line frequency is:

$$\Delta\bar{v} = \alpha_{k2}(P_{str} - P_0) + \alpha_{k3}[(T_{str} - T_{unstr}) + 99([Cr]_{str} - [Cr]_{unstr})] \quad (8)$$

where  $[Cr]_{str}$  is the chromium concentration of the stressed sample and  $[Cr]_{unstr}$  is the chromium concentration of the unstressed sample.

To summarize, the predicted fiber stresses in MMC's due to cooling after consolidation processing are in the 500 MPa range. From equation (3), a stress of this magnitude results in an approximate peak shift of  $\sim 3.8 \text{ cm}^{-1}$  (i.e.  $\sim 1.8 \text{ \AA}$  change in wavelength). For the shift to be detected spectroscopically a high resolution ( $<0.2 \text{ \AA}$ ) spectrometer must be used, and temperature corrections should be made if there is more than a  $0.5^\circ\text{C}$  difference in measurement temperature. It is also important that the composition of the stressed and (unstressed) reference fibers be the same (or independently measured) if potential errors from equation (7) are to be avoided. Finally, an experimental approach is required that interrogates fibers deeply within the composite so that the end effects reported by Ma and Clarke [13] and Liang and Hutchinson [31] do not dominate the measurement.

### 3.0 Experimental

#### 3.1 Sample Preparation

Two composite samples were fabricated by the foil-fiber-foil method from five sheets of 0.25 mm thick CP titanium foil (supplied by Alfa, Johnson Matthey Products) and three Cr(III)-doped single-crystal  $\text{Al}_2\text{O}_3$  fibers. The fibers for one

composite sample (COMP3) were nominally doped with 0.03wt% Cr(III) and were supplied by Saphikon, Inc. They were grown by the edge defined film fed growth (EFG) technique [35]. The attenuation coefficient of this fiber was measured by the cutback technique. Using the 632.8 nm line of a HeNe laser, the attenuation coefficient of a bare fiber was measured to be about  $0.52\text{ cm}^{-1}$ . Fibers for a second composite sample (COMP5) were nominally doped with 0.05 wt% Cr(III). These were manufactured using the laser pedestal growth (LPG) method by Lasergenics Corporation [36]. The linear attenuation coefficient of this fiber was found to be  $0.04\text{ cm}^{-1}$ .

Figure 3 shows the arrangement used for the composite layups. Square foil-fiber-foil layups were placed between two 0.75 mm thick, 10.16 cm diameter 307 stainless steel disks. The fibers were colinearly positioned approximately 5 mm apart. They were then shipped to Kin-Therm, Inc. where they were evacuated in a millitorr range vacuum and sealed by electron beam welding. The resulting can was then placed in a hot isostatic press (HIP) (Asea Brown Boveri Autoclave Systems, Inc., Minihipper), heated to  $900^\circ\text{C}$ , pressurized at 100 MPa for one hour, cooled at  $4.3^\circ\text{C}/\text{min}$ . down to  $250^\circ\text{C}$ , and air cooled to room temperature (about  $25^\circ\text{C}$ ). The can ends were then cut away to expose the transverse section of the fibers. Some loss of fiber alignment was noted to have accompanied the consolidation process.

The samples were mounted in epoxy and the exposed fiber ends polished to a  $0.05\text{ }\mu\text{m}$  alumina finish, and examined by scanning electron microscopy. Near some of the fibers radial matrix cracks had formed on cooling, Figure 4. The number of these radial cracks varied from fiber to fiber (and from one end of the fiber to the other) but were present to a greater or lesser extent on at least one end of each of the fibers in the composite. A ring of reaction product was also

seen at the fiber-matrix interface. It has been reported to be Ti<sub>3</sub>Al [37]. The reaction product thickness varies with consolidation conditions; for those used here it was 3  $\mu\text{m}$  thick. A debond crack had also formed between the fiber and the reaction product. This presumably formed (during sectioning) in response to the tensile radial stress that has been predicted to develop within ~25  $\mu\text{m}$  of the freshly exposed free surface [13, 31].

### 3.2 Spectroscopic Measurements

The spectroscopic measurements reported here were conducted using a fiber optically coupled set-up shown in Figure 5. An Omnichrome model 532-MAP air-cooled argon laser, set to lase at 514.5 nm, was used to excite fluorescence in the  $\alpha$ -Al<sub>2</sub>O<sub>3</sub> fibers. The laser beam was filtered through a CuSO<sub>4</sub> solution filter to eliminate laser plasma lines, particularly the one at 696.543 nm. The laser beam was then focused onto one arm of a bifurcated fiber optic bundle (supplied by Electro Fiberoptics Corp.) by a 5 cm focal length convex lens. The (1.6 mm diameter) common end of the fiber optic bundle was placed as close as possible to the end of the ruby fiber to be interrogated in order to obtain the maximum luminescence signal.

In practice, it was found that the fiber's axis was sometimes not perpendicular to the polished composite surface, and so was not always aligned with the fiber optic bundle. This prevented the efficient coupling of the exciting light into the ruby fiber and reduced the luminescence signal detected. By rotating the composite, it was usually possible to align the ruby fiber's axis with the axis of the fiber bundle which allowed for a much improved signal. Further signal improvements were achieved by focusing the laser beam onto only a single fiber in the fiber optic bundle and positioning this over the ruby fiber.

The second arm of the bifurcated fiber optic bundle transmitted the luminescence signal to a 0.64 m single grating monochromator (Instruments SA, model HR-640). Interfacing the fiber bundle to the monochromator was achieved by transmitting the luminescence signal from the fiber bundle through 20 mm and 60 mm focal length lenses and then focusing upon the monochromator slit. The slit used here was 20 mm in height and about 11  $\mu\text{m}$  in width. The monochromator was equipped with a 110 x 110 mm flat grating with 1200 grooves/mm. The resolution at the R line luminescence wavelength using this grating/slit combination was about 0.17  $\text{\AA}$ .

A Spectraview-2D CCD array was attached to the monochromator as a detector. The liquid nitrogen cooled array had a spectral response from 400 to 1000 nm. The signal from this array was then transmitted to a personal computer equipped with PRISM, a collection of computer programs and routines that have been developed by Instruments, SA, for the purpose of acquiring and analyzing spectroscopic data collected with their equipment. The PRISM program was used to position the monochromator to the desired region of the spectrum, to average and smooth peaks, and to make a preliminary determination of peak position wavelength. For more precise peak position determinations, a Simplex program was used to fit a double Lorentzian intensity curve to the R1, R2 line spectrum. The standard deviation of this measurement was  $0.1 \text{ cm}^{-1}$  (corresponding to about a 50 MPa stress error).

### 3.3 Spectroscopic Experiments

Spectra were obtained from each of the three fibers in the two composite samples. Two unstressed reference samples from the same original fiber used in each of the composites were also measured and used to find the peak shifts associated with compositing. At least three spectra were collected from each end of each composited fiber. The Simplex method was used to determine the

position of the R peaks, and the position values reported were then averaged for each fiber end. The average for each fiber end was then subtracted from the average for the appropriate unstressed fiber to provide  $\Delta\bar{v}$ . The temperature was recorded with each spectrum taken, and the appropriate temperature correction made using equation (6).

#### 4.0 Results

Figure 6 shows two representative luminescence spectra that include both R peaks. One corresponds to the signal from a composited fiber and the other to that of an uncomposited fiber. Shifts due to compositing can be seen for both peaks. In order to measure the R line shifts associated with the compositing process, luminescence spectra were obtained from both ends of each fiber in the COMP3 and COMP5 samples and from uncomposited fibers from the same fiber batches used to produce the composites. The peak positions and measurement temperatures were measured three times for all fibers in both samples, together with the reference fibers.

The average R1 and R2 temperature corrected peak shifts ( $\Delta\bar{v}_1$  and  $\Delta\bar{v}_2$ ) are given for both ends of each COMP3 sample fiber in Table 4 and for the COMP5 sample in Table 5.  $T_{str} - T_{unstr}$  ranged from  $-0.37^{\circ}\text{C}$  to  $+0.1^{\circ}\text{C}$  so that the temperature correction varied from  $-0.05$  to  $+0.01 \text{ cm}^{-1}$ . Compositing can be seen to have resulted in a red shift associated with the development of a predominantly compressive stress in the fiber.

**Table 4:** R line peak shifts from the composite containing fibers doped with 0.03wt% Cr(III): (i) end A, and (ii) end B.

(i) End A			(ii) End B		
Fiber	$\Delta\bar{v}_1$ (cm <sup>-1</sup> )	$\Delta\bar{v}_2$ (cm <sup>-1</sup> )	Fiber	$\Delta\bar{v}_1$ (cm <sup>-1</sup> )	$\Delta\bar{v}_2$ (cm <sup>-1</sup> )
1	-2.43±0.10	-2.99±0.10	1	-2.19±0.12	-2.83±0.10
2	-4.62±0.09	-6.24±0.10	2	-5.06±0.10	-6.58±0.11
3	-2.65±0.10	-3.26±0.10	3	-2.51±0.11	-3.34±0.10
Average	-3.23	-4.16	Average	-3.25	-4.26

**Table 5:** R line peak shifts from the composite containing fibers doped with 0.05wt% Cr(III): (i) end A, and (ii) end B.

(i) End A			(ii) End B		
Fiber	$\Delta\bar{v}_1$ (cm <sup>-1</sup> )	$\Delta\bar{v}_2$ (cm <sup>-1</sup> )	Fiber	$\Delta\bar{v}_1$ (cm <sup>-1</sup> )	$\Delta\bar{v}_2$ (cm <sup>-1</sup> )
1	-2.69±0.15	-3.51±0.16	1	-2.89±0.11	-4.08±0.10
2	-3.88±0.10	-5.16±0.10	2	-4.09±0.10	-5.33±0.10
3	-4.35±0.10	-5.90±0.10	3	-4.63±0.10	-6.43±0.10
Average	-3.64	-4.86	Average	-3.87	-5.28

The errors in Tables 4 and 5 include contributions associated with the temperature correction. These arise from uncertainty in the temperature correction coefficient ( $\pm 0.006 \text{ cm}^{-1}/\text{K}$ , shown in Table 2), and uncertainty in the two measurement temperatures ( $\pm 0.5^\circ\text{C}$ ). The tables have root mean errors calculated using the equation:

$$\Delta(\Delta\bar{v}) = \{(\Delta\bar{v}^s)^2 + (\Delta\bar{v}^{\text{ref}})^2 + (T_{\text{str}} - T_{\text{unstr}})^2(\Delta\alpha_{k3})^2 + (\alpha_{k3})^2[(\Delta T_{\text{str}})^2 + (\Delta T_{\text{unstr}})^2]\}^{1/2} \quad (10)$$

where  $\Delta(\Delta\bar{v})$  is the error in the peak shift (in  $\text{cm}^{-1}$ ),  $\Delta\alpha_{k3}$  is the error in the temperature coefficient, and  $\Delta T_{\text{str}}$  and  $\Delta T_{\text{unstr}}$  are the estimated uncertainties in the temperature measurements [38].

## 5.0 Discussion

Large R1 and R2 peak shifts have been observed to accompany the incorporation of  $\alpha$ -Al<sub>2</sub>O<sub>3</sub> fibers in a CP titanium matrix. They can be compared to predicted peak shifts by combining the expected state of fiber stress (from a residual stress model) and equation (3) using previously reported values for the piezospectroscopic constants. We have chosen to use the residual stress model of Pindera and Freed [9] to calculate the residual stress in the fibers because it can accommodate fibers with either isotropic, transversely isotropic, or orthotropic elastic and CTE constants (c-oriented sapphire fibers can be reasonably approximated as transversely isotropic), and because it allows the matrix to be either elastic or elastic-plastic. Because the residual stresses calculated by the Pindera and Freed model are based on the local/global stiffness matrix method of Bufler [39], it facilitates the analysis of problems with many concentric cylindrical layers. Thus, the effects of an interfacial reaction product (Ti<sub>3</sub>Al) layer in the samples used here could also be incorporated into the stress predictions.

To calculate the stress, we assumed the fiber to be an infinite cylinder with transversely isotropic, temperature dependent elastic and CTE components. Values for these have been obtained from the literature (Table 6). The matrix has been modelled as a concentric cylinder with either isotropic elastic, or elastic plastic with a linear-hardening constitutive behavior. The expansion coefficients ( $\alpha$ ), Young's moduli (E), yield stresses ( $\sigma_y$ ), and linear strain hardening parameters (SHP) of the matrix cylinder were all allowed to be dependent upon temperature. For one case, a 3  $\mu\text{m}$  thick matrix shell was included and given the thermo-physical and mechanical properties of Ti<sub>3</sub>Al (the reaction product). The model assumed continuity of displacements at the layer interfaces (no debonding) and a uniform temperature throughout the body at any moment during cooling. Both

are reasonable for the interior of the composite studied here (but not for the free surface of the sectioned composite because of radial debonding). It computes the axial, radial, and hoop (=radial) fiber stress components, and those of the matrix as a function of radial position.

**Table 6:** Physical properties used in model: (a) for sapphire, (b) for titanium, and (c) for Ti<sub>3</sub>Al.

(a) Sapphire\*

Temperature (°C)	$\alpha \times 10^6 \text{ } ^\circ\text{C}^{-1}$		$\alpha' \times 10^6 \text{ } ^\circ\text{C}^{-1}$		$\alpha'' \times 10^6 \text{ } ^\circ\text{C}^{-1}$	
	c-axis	a-axis	c-axis	a-axis	c-axis	a-axis
24	6.26	5.51	7.14	6.70	5.74	5.10
100	6.26	5.51	7.43	6.98	6.30	5.17
300	7.25	6.47	8.16	7.68	6.82	5.58
500	7.90	6.78	8.84	8.31	7.31	6.10
700	8.26	7.43	9.47	8.88	7.69	6.43
900	8.60	7.76	10.00	9.38	8.24	7.04

T (°C)	E <sub>11</sub> (GPa)	E <sub>33</sub> (GPa)	v <sub>12</sub>	v <sub>13</sub>
24	423	460	0.305	0.169
100	420	457	0.308	0.168
300	413	451	0.316	0.167
500	405	445	0.323	0.166
700	398	439	0.331	0.165
900	391	433	0.338	0.165

$$\sigma_y = 68 \text{ GPa}$$

(b) Titanium\*

T (°C)	E (GPa)	SHP (GPa)	$\sigma_y$ (MPa)	$\alpha \times 10^6 \text{ } ^\circ\text{C}^{-1}$
24	107	2.0	571	8.66
100	101	1.9	396	9.02
300	86	1.7	190	9.34
500	71	1.5	117	9.52
700	56	1.4	116	10.10
900	40	1.2	116	10.74

$$v=0.361$$

(c) Ti<sub>3</sub>Al\*\*

T (°C)	E (GPa)	$\sigma_y$ (MPa)
24	147	532
100	143	508
300	132	444
500	120	163
700	109	163
900	97	116

$$v=0.3 \quad SHP=3 \text{ GPa} \quad \alpha=10.4 \times 10^{-6} \text{ }^{\circ}\text{C}^{-1}$$

\* Sapphire moduli calculated from [40]. Titanium elastic moduli and yield stress taken from [41].  $\alpha$  taken from (i) for titanium from [42] (recommended values used), and (ii) for sapphire, [43].  $\alpha'$  and  $\alpha''$  for sapphire taken from [44] (for  $\alpha'$ : values obtained by differentiating the equation recommended for calculating strain as a function of temperature; for  $\alpha''$ : curve 127 used for room temperature a-axis value, curve 58 used for other a-axis values; curve 126 used for room temperature c-axis value, curve 59 used for other c-axis values).

\*\*Elastic modulus and Poisson's ratio for Ti<sub>3</sub>Al are from [45].  $\sigma_y$  for Ti<sub>3</sub>Al at T≥500°C is from [46]. Remaining data are for Ti-24Al-11Nb (at%), which has low temperature properties similar to those of Ti<sub>3</sub>Al, taken from [47].

The stresses predicted by the model are only as valid as the thermophysical constants (Table 6) that go into the calculations. The elastic constants, E<sub>33</sub> and E<sub>11</sub>, in Table 6 are axial and transverse Young's moduli for c-oriented sapphire fibers whilst v<sub>13</sub> and v<sub>12</sub> are the axial and transverse Poisson's ratios, respectively. They were calculated from compliance constant data using a transverse isotropy approximation [41].

The residual stresses for several different cases, (see Fig. 7) have been analyzed using various assumptions (presence or absence of a reaction product, elastic or elastic/plastic matrix behavior, and variation of fiber volume fraction). Three different reported values for the thermal expansion coefficients of the sapphire fiber have been examined since this property dominates the predicted shifts, and there exists significant variability in the reported values.

The ratio of fiber to sample area is 0.2% for the samples studied here, and so we have begun our stress analysis (Case I in Fig. 7) by taking a fiber volume fraction of 0.2%. The stress-free temperature of 900°C (the consolidation condition) was used and the sample was allowed to cool to 25°C. Transversely isotropic elastic and CTE properties (the values denoted by  $\alpha$  in Table 6) were used for the fiber. The CTE values were those recommended for the Saphikon fiber by its producer. The matrix was assumed elastic with no reaction product present. It was also assumed that stresses began to develop immediately upon cooling (i.e., there was no range of temperatures for which creep was able to relax the stress). The resulting stresses and their distribution are those shown earlier in Figure 1. The stress components in the fiber were independent of position and calculated to be  $\sigma_{rr}=\sigma_{\theta\theta}=-194$  MPa and  $\sigma_{zz}=-869$  MPa. Substituting these (position independent) fiber stresses into equation (3) and using the values of Feher and Sturge for the piezospectroscopic constants [25], the predicted R line shift:

$$\begin{aligned}\Delta\bar{v} &= (2.7 \text{ cm}^{-1}/\text{GPa})(2)(-0.194 \text{ GPa}) + (2.15 \text{ cm}^{-1}/\text{GPa})(-0.869 \text{ GPa}) \\ &= -2.92 \text{ cm}^{-1}\end{aligned}$$

This predicted line shift is in the range of the measured values (see Tables 4 and 5) but somewhat smaller than the average values - a conclusion that is independent of the choice of  $\Pi_{ij}$  values in Table 1.

The residual stress model predictions are sensitive to changes in the fiber fraction and the thermophysical parameters of the model. Since there is some uncertainty regarding the best choices for each of these, the model has been used to investigate the stability of the predicted shifts for the range of possible values for these parameters.

The first change (Case II) was made to the fiber volume fraction ( $V_f$ ). For the  $\Delta\bar{v}$  values calculated above, the fiber volume fraction was ~0.2% since this

was the ratio of fiber to sample cross sectional areas. However, only three fibers were present, and it could be argued that the central fibers may have "seen" a different volume fraction to the outer ones. To obtain a measure of the model's sensitivity to this, the fiber fraction was arbitrarily increased to 1.5%. The stress components were (Fig. 7) similar to the first case run, and the peak shift was  $-2.82 \text{ cm}^{-1}$  (within the error of the experiments, the same as Case I). Thus, for the very low volume fractions considered here, variability in fiber fraction can be discounted as a contributor to the discrepancies between model-predicted and measured line shifts and to the variability in the line shifts between individual fibers.

The issue next addressed (Case III) was that of matrix plasticity, which can relax the residual stresses. The residual stress calculations of Case I were reperformed, but this time matrix plasticity was allowed. The stress components calculated were  $\sigma_{rr}=\sigma_{\theta\theta}=-193 \text{ MPa}$  and  $\sigma_{zz}=-869 \text{ MPa}$ . If these are compared with Case I, it is clear that no significant plastic relaxation occurred, and this can also be eliminated as a source of the differences in predicted and measured line shift.

The next consideration (Case IV) was the observation that a  $\text{Ti}_3\text{Al}$  reaction zone had formed around the fiber during processing (prior to cooling), as observed in Figure 4. The effect of this can be incorporated by introducing a concentric ring with the properties of  $\text{Ti}_3\text{Al}$  (Table 6c) into the model. When this was performed, the model again predicted similar fiber stresses to Case I and a line shift of  $-2.93 \text{ cm}^{-1}$ , and we conclude that reaction products do not significantly affect the stress.

The final consideration (Case V) was that of uncertainty in literature values for the CTE. There is a significant range of CTE values reported in the literature, and so we have calculated the peak shift using two other CTE values. For one

case, the  $\alpha'$  values of Table 6 were used [44]. Otherwise, the physical properties are the same as in Case I. These CTE values are significantly larger than those used in the cases previously presented, resulting in a reduced stress and a peak shift of only  $-1.41\text{cm}^{-1}$ . This is approximately half the value calculated for the previous cases and significantly less than any of the measurements. No plasticity was predicted to have occurred in this case. The lowest reported CTE's were also used (the  $\alpha''$  values are given in Table 6) to calculate the stress. The resulting stress components were predictably much larger (Fig. 7) and result in a peak shift of  $-3.59\text{ cm}^{-1}$ . A small amount of matrix plasticity was also predicted to have occurred, but enforcing an elastic matrix response in the model did not significantly change the predicted stress.

From these residual stress calculations we conclude that the predicted peak shift lies in the range of  $-1.41$  and  $-3.59\text{ cm}^{-1}$ , depending on the values taken for the expansion coefficient of sapphire. Tables 4 and 5 show that these predicted values of  $\Delta\bar{v}$  overlap the lower end of the values measured in COMP3 and COMP5. The troubling issues are the significant, reproducibly measured variability in  $\Delta\bar{v}$  values between the fibers within both composites and, for some fibers, measured shifts that were significantly larger than any of the predictions. The line shift values observed here have recently been independently verified by Lipkin and Clarke [28] and cannot be attributed to a systematic measurement error. The variability is also significantly larger than the random experimental error. The calculations above show that it cannot be accounted for by different amounts of matrix plasticity, fiber volume fraction variations or interfacial reaction product layer effects.

The most obvious reason for measured  $\Delta v$  that are smaller (and more variable) than predicted is the radial matrix cracking seen in the micrographs of Figure 4. Highly variable amounts of crack(s) observed for all the fibers in

COMP3 and COMP5. Since a radial crack provides a mechanism to elongate the matrix in the hoop direction, this can relax both the fibers' hoop (and the mechanically coupled radial) stress, and thus reduce the peak shift. The variability in cracking (which may extend along the fiber) would then account for the variability in line shift observed.

A second possibility is that, for some fibers, the luminescence signal was obtained from the end of the fiber (where free surface effects result in lower stresses than an infinite fiber residual stress model would predict) due to inefficient optical coupling/transmission in the fiber. Ma and Clarke have shown that significant relaxation of the stresses does occur, and within a fiber diameter or so of the fiber end, the radial stress can even be tensile [13, 28]. Lipkin and Clarke [28] confirm that similar relaxations occurred in these samples. Indeed, metallography of the samples indicated that radial debonding of the fiber-matrix interface had occurred at the free surface, consistent with this hypothesis. Furthermore, we note that the COMP3 sample with fibers of poorer transmissivity gave slightly smaller peak shift. Thus, it is possible that for some (misaligned or highly attenuating) fibers, signals were more heavily weighted by end effects which contributed to a smaller than expected peak shift.

It is not so straightforward to explain why the measured  $\Delta\bar{v}$  values were sometimes greater than the predicted values. One possibility could have been a variation in the concentration of Cr(III) in the fibers. Ma and Clarke have reported that changes in the Cr(III) concentration creates different amounts of strain in an Al<sub>2</sub>O<sub>3</sub> matrix which can be observed as a shift in the ruby luminescence peaks [13]. Thus, enhanced concentrations of Cr(III) in a composited fiber compared to an unstressed reference could give an "anomalous" increase in the apparent compressive stress. EDAX analysis on the fiber ends of the COMP3 sample indicated this not to be the case here. The second possibility

is that stress existed in the pre-composited fiber. Though small stresses can develop in fibers grown by the EFG or LPG processes, the small temperature differences [48] make it unlikely that these are sufficient to account for the anomalous shift observed here, especially since all the fiber segments came from a single original piece of fiber.

Further insight into this anomalous shift can be gained by recalling that equation (4) for the two measured ( $R_1$  and  $R_2$ ) line shifts is really two linear equations in three unknowns ( $\sigma_{rr}$ ,  $\sigma_{\theta\theta}$  and  $\sigma_{zz}$ ) and a constraining relation ( $\sigma_{rr} = \sigma_{\theta\theta}$ ) exists between two of the unknowns. Thus, in principle, one can determine both of the unknown components of stress. Using the Lipkin and Clarke [28] piezospectroscopic constants of Table 1, and the average line shifts of Tables 4 and 5, we find the stress components shown in Table 7.

Table 7: Stress components recovered from  $R_1$  and  $R_2$  line shift data.

(a) 0.03wt% Cr doped fibers

(i) End A			(ii) End B		
Fiber	$\sigma_{zz}$ (GPa)	$\sigma_{rr}=\sigma_{\theta\theta}$ (GPa)	Fiber	$\sigma_{zz}$ (GPa)	$\sigma_{rr}=\sigma_{\theta\theta}$ (GPa)
1	1.14	0.099	1	1.19	0.058
2	2.81	0.055	2	2.80	0.120
3	1.26	0.108	3	1.48	0.041

(b) 0.05wt% Cr doped fibers

(i) End A			(ii) End B		
Fiber	$\sigma_{zz}$ (GPa)	$\sigma_{rr}=\sigma_{\theta\theta}$ (GPa)	Fiber	$\sigma_{zz}$ (GPa)	$\sigma_{rr}=\sigma_{\theta\theta}$ (GPa)
1	1.50	0.062	1	1.96	-0.008
2	2.27	0.065	2	2.28	0.095
3	2.68	0.046	3	3.02	0.012

Even though the stress values obtained are obviously sensitive both to error in line shift measurement and in the piezospectroscopic constants, it is clear from

Table 7 that 1) significantly lower than expected radial (and hoop) stresses are present in these fibers and 2) the axial stresses are much greater than predicted by a concentric cylinder's analysis of the fiber-matrix CTE mismatch.

The lower than expected radial stress values can be attributed to the radial matrix cracks, but the high axial stress cannot. One explanation for the anomalous high axial stress result is the existence of a second source of compressive stress in the composite. Such a stress could arise from a CTE mismatch with the stainless can used for consolidation (Fig. 3). Since the coefficient of thermal expansion of the circular stainless steel canister used for sample preparation ( $17.3 \times 10^{-6} \text{ }^{\circ}\text{C}^{-1}$ ) was more than twice that of titanium ( $8.7 \times 10^{-6} \text{ }^{\circ}\text{C}^{-1}$ ), the entire composite would be subjected to an additional compressive stress on cooling. At high temperatures during the cooling, the matrix would creep or plastically deform in response to this, and this would transfer a significant fraction of the can load onto the fibers (particularly in the axial direction).

To gain additional insight into this, we have incorporated into the concentric cylinder's analysis, an additional ring with the properties of the stainless steel tooling. Using a volume fraction of 50% for the can and relaxing the pressure used for consolidation monotonically, the concentric cylinder analysis predicts an axial (compressive) fiber stress of -2730 MPa and a radial stress of -280 MPa after cooling. Some of this would be relaxed when the can material is removed, but the inelastic matrix deformations incurred during cooling ensure that an additional compressive fiber stress would be present, and a larger than otherwise predicted peak shift for both R lines occurs.

We propose that the stress in the fibers of HIP consolidated composites arises from a combination of fiber/matrix and composite/tooling CTE mismatch in conjunction with a relaxation of the transverse stress components by radial matrix cracking. It is interesting to note that the large measured compressive stress that

remains in the fibers studied here would have a significant effect upon the apparent insitu strength of the fiber and thus the composite's strength in tension. Compressive strength would also be adversely impacted due to fiber buckling at lower applied loads. The additional stress would also affect the extent of fiber-matrix debonding, and thus pullout behavior, during crack growth. These tooling associated stresses are ignored in the modelling of mechanical properties, and this needs to be addressed, since mechanical properties are likely to depend upon the material used for HIP tooling. In the extreme case where tooling materials are used whose expansion coefficients are much less than that of the composite, the fiber could even suffer a tensile axial residual stress with the risk of fiber fragmentation during cooling and a resulting composite of very poor quality.

## 6.0 Summary

The underlying principles of a luminescence method for measuring stress have been reviewed and applied to the problem of residual stress determination in metal matrix composites. It has been shown that the change in residual stress associated with the compositing of Cr doped  $\alpha$ -Al<sub>2</sub>O<sub>3</sub> fibers in a titanium matrix can be detected via a fiber optically coupled luminescence measurement. The luminescence peak shifts are smaller in magnitude than those predicted from thermal stress models, and a reproducible variability in the line shifts for different fibers in the composite has been observed. Using both R1 and R2 line data, the axial and transverse stress contributions to the line shifts have been separated, we find the axial stresses to be more than two times that of the predictions whilst those in the radial (and hoop) directions are significantly smaller. We attribute the large axial stress to a CTE difference between the HIP containment and the composite which is not included in most residual stress analyses. The low measured radial/hoop fiber stress components are proposed to result from radial

matrix cracking. These two "unmodelled" phenomena have offset one another in the R1 or R2 luminescence measurement and resulted in the fortuitous rough agreement between concentric model predictions and individual peak shift measurements. The stress developed because of the HIP tooling could significantly affect the quality of metal matrix composites and introduces an additional dependence of mechanical properties upon the detailed manner of composite manufacture.

### Acknowledgments

We are grateful to D. G. Backman for encouraging this work, G. Fitzgibbon of Saphikon for the donation of fiber, D. R. Clarke for helpful comments concerning our luminescence measurements and for confirming our observations, and to J. Hutchinson for discussions of the interpretation of data. This work has been supported by an ARPA-URI grant under contract number N0014-86-K0753 (managed by S. Fishman and W. Coblenz), a NASA-ARPA program (NAGW-1692 (directed by W. Barker and R. Hayduk) and by the University of Virginia's Academic Enhancement Program.

## References

1. M. Taya and R.J. Arsenault, *Metal Matrix Composites: Thermomechanical Behavior*, p. 1-8, Pergamon Press (1989).
2. T.W. Clyne and P.J. Withers, *An Introduction to Metal Matrix Composites*, Cambridge University Press, 470 (1993).
3. J.M. Larsen, W.C. Revelos and M.L. Gambone, "An Overview of Potential Titanium Aluminide Composites in Aerospace Applications," *Mater. Res. Soc. Proc.*, v. 273, p. 3, MRS (1992).
4. H. Poritsky, *Physics*, 5, 406 (1934).
5. P.K. Brindley, P.A. Bartolotta and R.A. MacKay, "Thermal and Mechanical Fatigue of SiC/Ti<sub>3</sub>Al+Nb," *Proceedings HIGHTEMP Review*, NASA CP 10039, p.52-1 to 52-14 (1989).
6. T.C. Lu, J. Yang, Z. Suo, A.G. Evans, R. Hecht and R. Mehrabian, *Acta Met. Material.*, 39(8) 1883 (1991).
7. K.K. Chawla, *Composite Materials: Science and Engineering*, p. 186-96, Springer-Verlag (1987).
8. R.P. Nimmer, *J. Comp. Tech. Res.*, 12(2), 65 (1990).
9. M-J. Pindera and A.D. Freed, "The Effect of Multiple Compliant Layers at the Fiber-Matrix Interface on Residual Thermal Stresses on Metal Matrix Composites," *Proc. of the 3rd Intl'l Conference on Eng., Constr., and Op. in Space* (1992).
10. B.N. Cox, M.R. James, D.B. Marshall and R.C. Addison, Jr., *Met. Trans.*, 21A, 2701 (1990).
11. P.K. Wright, D. Kupperman and H.N.G. Wadley, *Proceedings of 4th Annual HIGHTEMP Review*, NASA Conf. Publication, 10082, 45.1 (1991).
12. T.A. Kuntz, H.N.G. Wadley and D.R. Black, *Met Trans A*, 24A, 1117 (1993).
13. Q. Ma and D.R. Clarke, *Acta Met. Mater.*, 41(6), 1817 (1993).
14. H.J. Hough, J.N. Demas and H.N.G. Wadley, "Luminescence Sensing of Stress in Composite Structures," *Proc. of Review of Quantitative Nondestructive Evaluation*, Vol. 12, Eds. D. O. Thompson and D. E. Chimenti, Plenum, (New York), p. 1337, 1993.
15. J. H. Eggert, K.A. Goettel and I.F. Silvera, *Phys. Rev. B*, 40(8) 5724 (1989).
16. A.L. Schawlow, "Fine Structures and Properties of Chromium Fluorescence in Aluminum and Magnesium Oxide," *Advances in Quantum Electronics*, pp. 50-64, ed. J.R. Singer, Columbia University Press (1961).
17. A.L.. Schawlow, A.K. Piksis and S. Sugano, *Phys. Rev.*, 122, 5, 1469 (1961).

18. W.A. Bassett, T. Takahashi and M.K. Mao, *J. Appl. Phys.*, **39**, 319 (1968).
19. R.A. Forman, G.F. Piermarini, J.D. Barnett and S. Block, *Science*, **176**, 284, (1972).
20. J.D. Barnett, S. Block and G.J. Piermarini, *Rev. Sci. Instr.*, **44**, 1,1 (1973).
21. G.J. Piermarini, S. Block, J.D. Barnett and R.A. Forman, *J. App. Physics*, **46**(6) 2774 (1975).
22. P.M. Bell, H.K. Mao and K. Goettel, *Science*, **226**, 542 (1984).
23. J.A. Xu, H.K. Mao and P.M. Bell, *Science*, **232**, 1404 (1986).
24. H.K. Mao, P.M. Bell, J.W. Shaner and D.J. Steinberg, *J. App. Physics*, **49**(6), 3276 (1978).
25. L. Grabner, *J. Appl. Phys.*, **49**(2), 580, 1978.
26. A.A. Kaplyanskii and A.K. Przhevuskii, *Dokl. Akad. Nauk SSSR*, **142**, 311 (1962) [Sov. Phys.-Dokl. **7**, 37 (1962)].
27. E. Feher and M.D. Sturge, *Phys. Rev.*, **172**, 244 (1968).
28. D.M. Lipkin and D.R. Clarke, *Fracture Mechanics: 25th Volume, ASTM STP 1220*, Eds. F. Erdogan and R.J. Hartranft, ASTM (Philadelphia), 1994 (in press).
29. J. He and D.R. Clarke, to be published.
30. S.E. Molis and D.R. Clarke, *J. Am. Ceram. Soc.*, **73**(11), 3189 (1991).
31. C. Liang and J. Hutchinson, *Mechanics of Materials*, **14**, 202 (1993).
32. S.L. Wunder and P.E. Schoen, *J. Appl. Phys.*, **52**(6), 3772 (1981).
33. R.G. Munro, G.J. Piermarini, S. Block and W.B. Holzapfel, *J. Appl. Phys.*, **57**(2), 165 (1985).
34. A.A. Kaplyanskii, A.K. Przhevuskii and R.B. Rozenbaum, *Sov. Phys. Solid St.*, **10**, 1864 (1969).
35. D.G. Backman, D. Wei, L.C. Filler, R. Irwin and J. Collins, *Advanced Sensing, Modelling and Control of Materials Processing*, ed. E.F. Mattheys and B. Kushner, p. 3, The Minerals, Metals and Materials Society, Warrendale, PA (1992).
36. M. M. Fejer, J.L. Nightingale, G.A. Magel and R.L. Byer, *Rev. Sci. Instrum.*, **55**(11), 1791 (1984).
37. A.K. Misra, *Met. Trans.*, **22A**, 415 (1991).
38. J.P. Holman, with W.J. Gajda, Jr., *Experimental Methods for Engineers*, 5th ed., p.41-47, McGraw-Hill, Inc. (1989).
39. H. Bufler, *J. Elasticity*, **1**, 125 (1971).

40. W.E. Tefft, S. Res. of NBS, 70, A (4), 277 (1966).
41. *A Manual for Microwave Tubes*, ed. D.L. Thornburg, E.S. Thall, J. Brous, Radio Corp. of America, Harrison, NJ, p. 26, 183 (1960).
42. *Thermophysical Properties of Matter*, v.12, ed. Y.S. Touloukian et al., IFI/Plenum, p. 346 (1975).
43. *Alumina as a Ceramic Material*, W. Gitzen, (1970).
44. *Thermophysical Properties of Matter*, v.13, ed. Y.S. Touloukian et al, IFI/Plenum, (1975).
45. F.E. Schafrik, Met. Trans., 8A(6), 1003 (1977).
46. J.W. Newkirk and G.B. Feldewerth, from *High-Temperature Ordered Intermetallic Alloys III*, v. 133, Mat. Res. Soc. Proc., ed. C.T. Liu et al, p. 681, MRS, Pittsburgh, PA, (1989).
47. D.A. Lukasak and D.A. Koss, Met. Trans., 21A(1) 135 (1990).
48. D.G. Backman, Private Communication (1993)

## **ELASTIC-PLASTIC MODEL PREDICTED STRESSES**

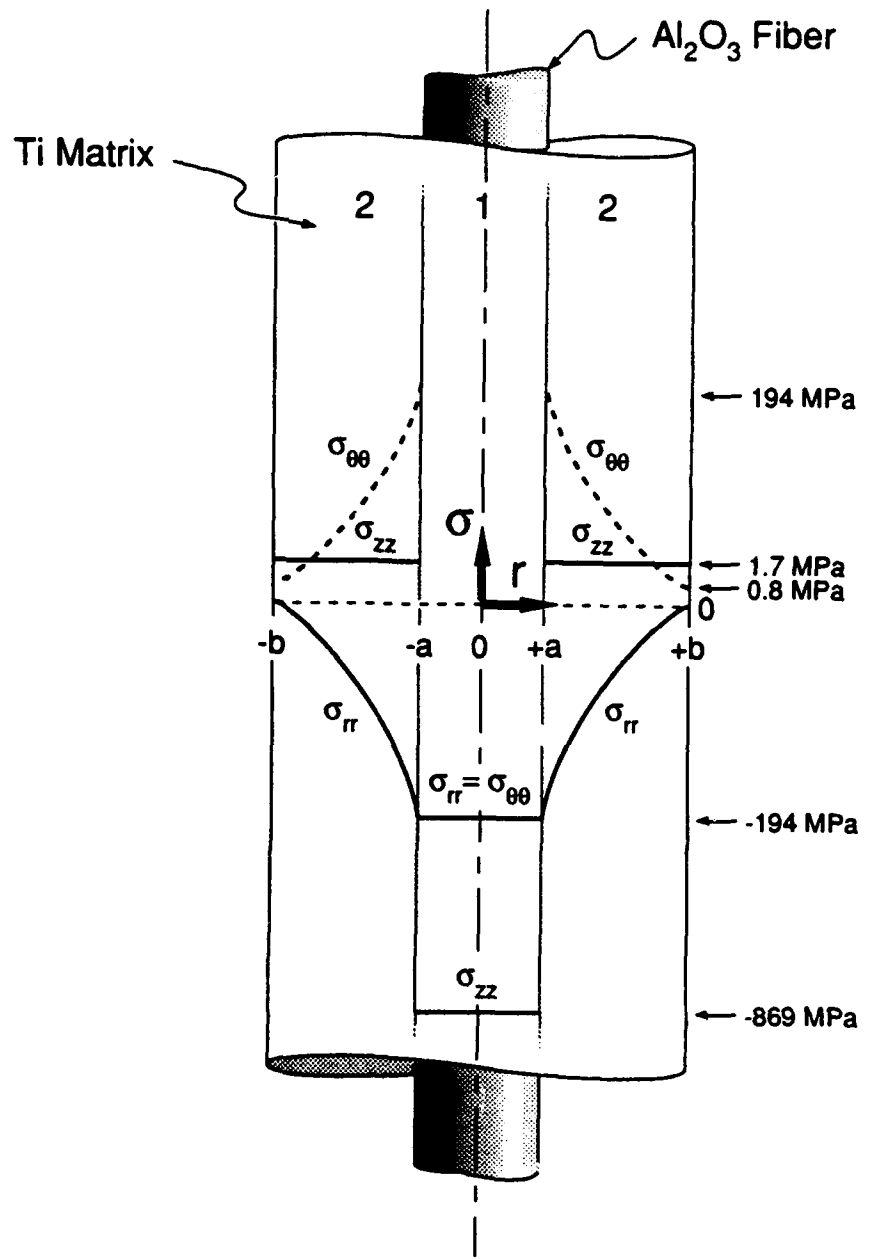


**Figure 1.** Schematic of Pindera-Freed model predictions of stress components in and near a composites fiber.

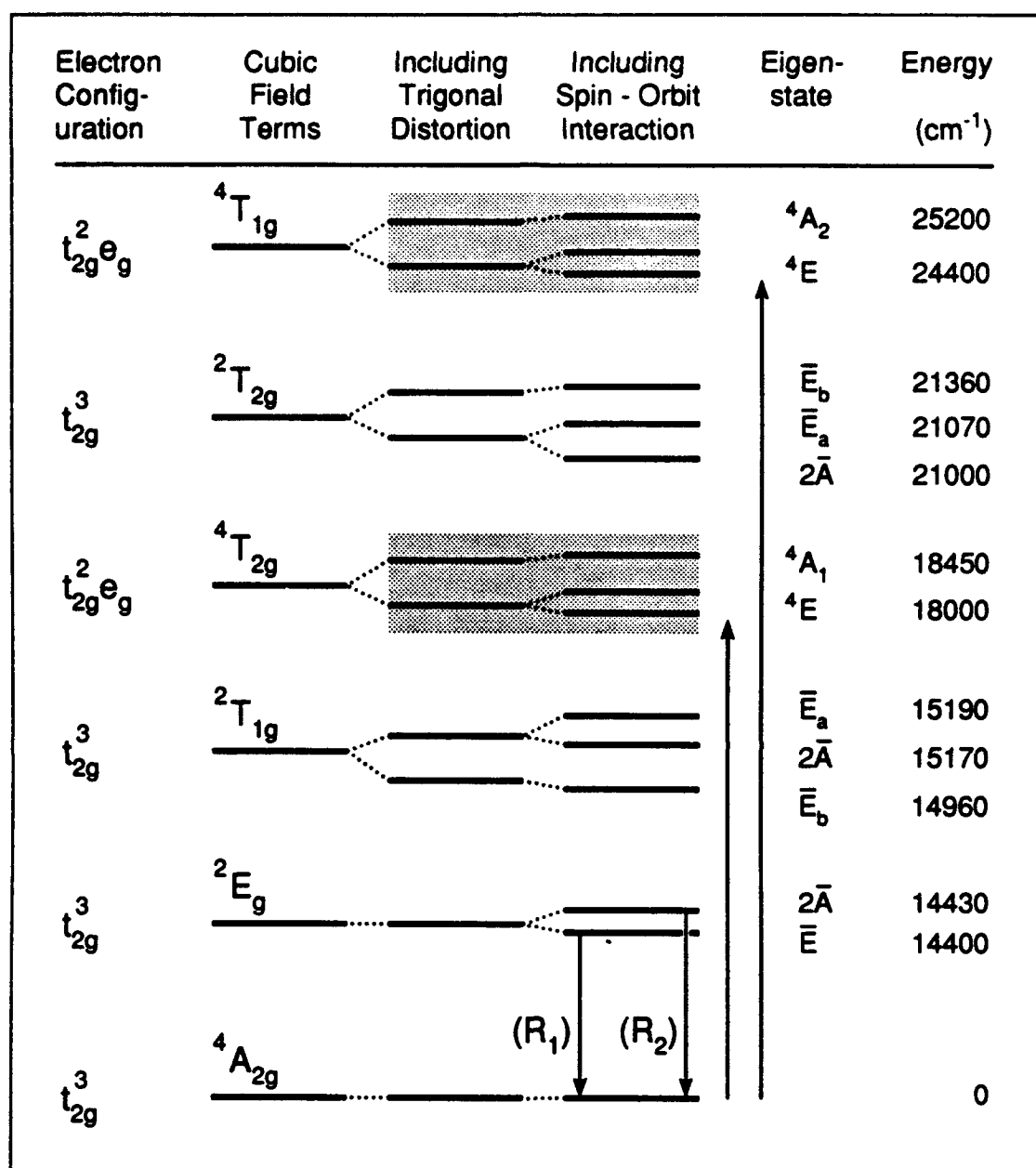


Figure 2. Diagram showing the electronic structure of ruby for those transitions in the visible region and the phenomena that cause the splittings. (Redrawn from [15]).

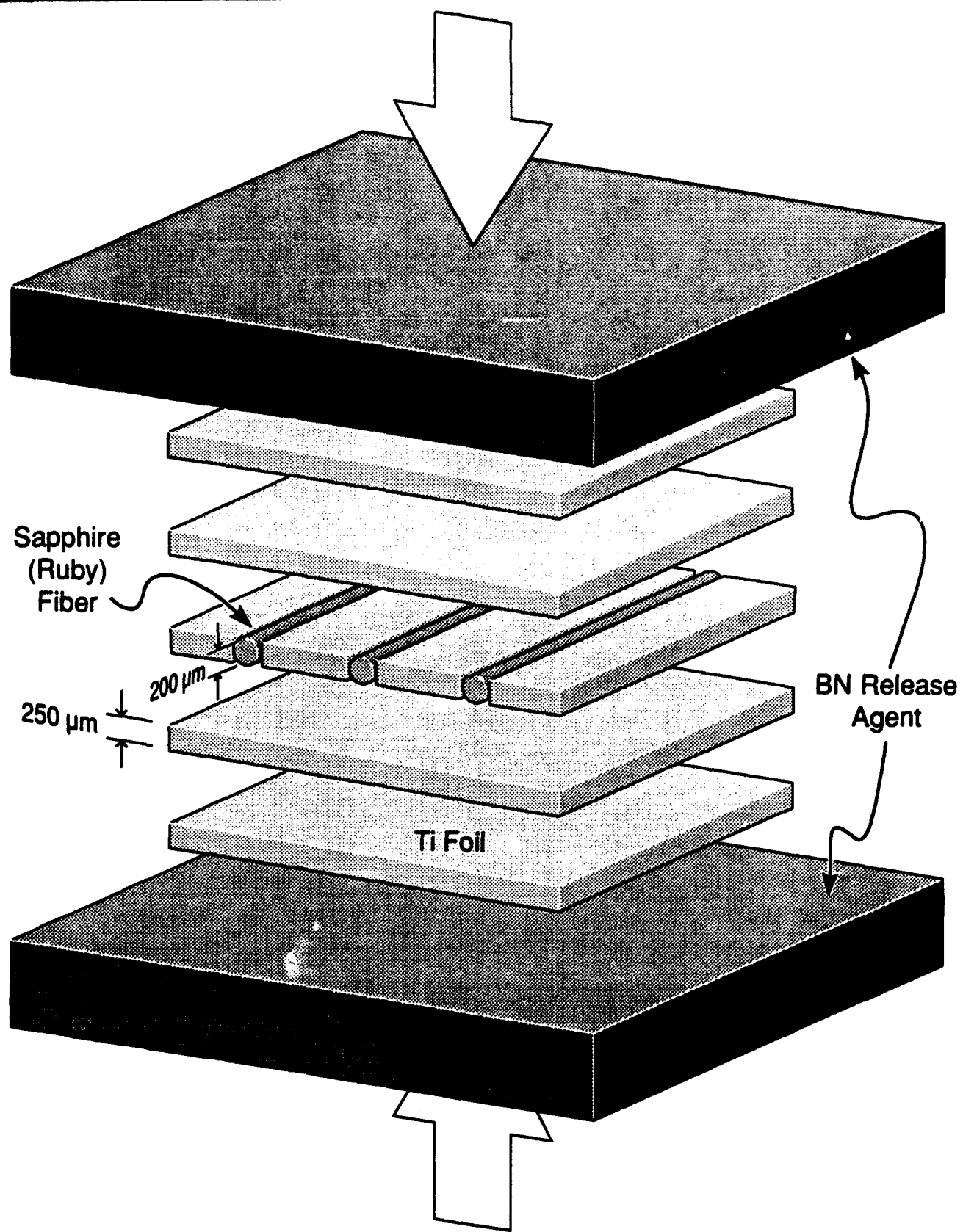


Figure 3. Schematic representation of spatial arrangements of Ti foil and ruby fibers prior to consolidation. (Square stainless steel sheets are shown for simplicity: circular disks of stainless steel were used in practice.)



(a)



(b)

Figure 4. Scanning electron micrograph of the fibers in COMP3: (a) the middle fiber, and (b) closeup of the middle fiber.

## **Luminescence Fiber Stress Determination**

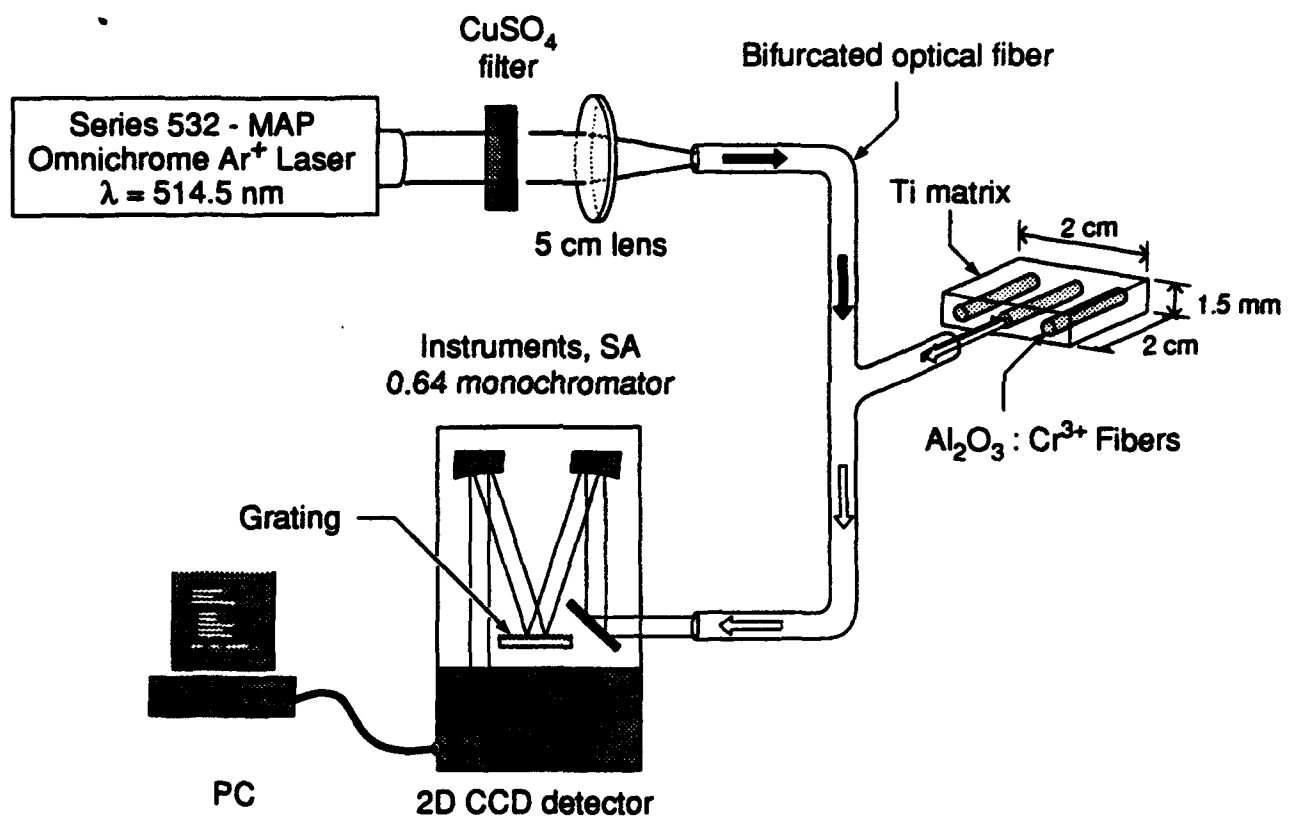


**Figure 5.** Schematic diagram of the spectroscopic system used to fiber optically measure the residual stress in MMC's.

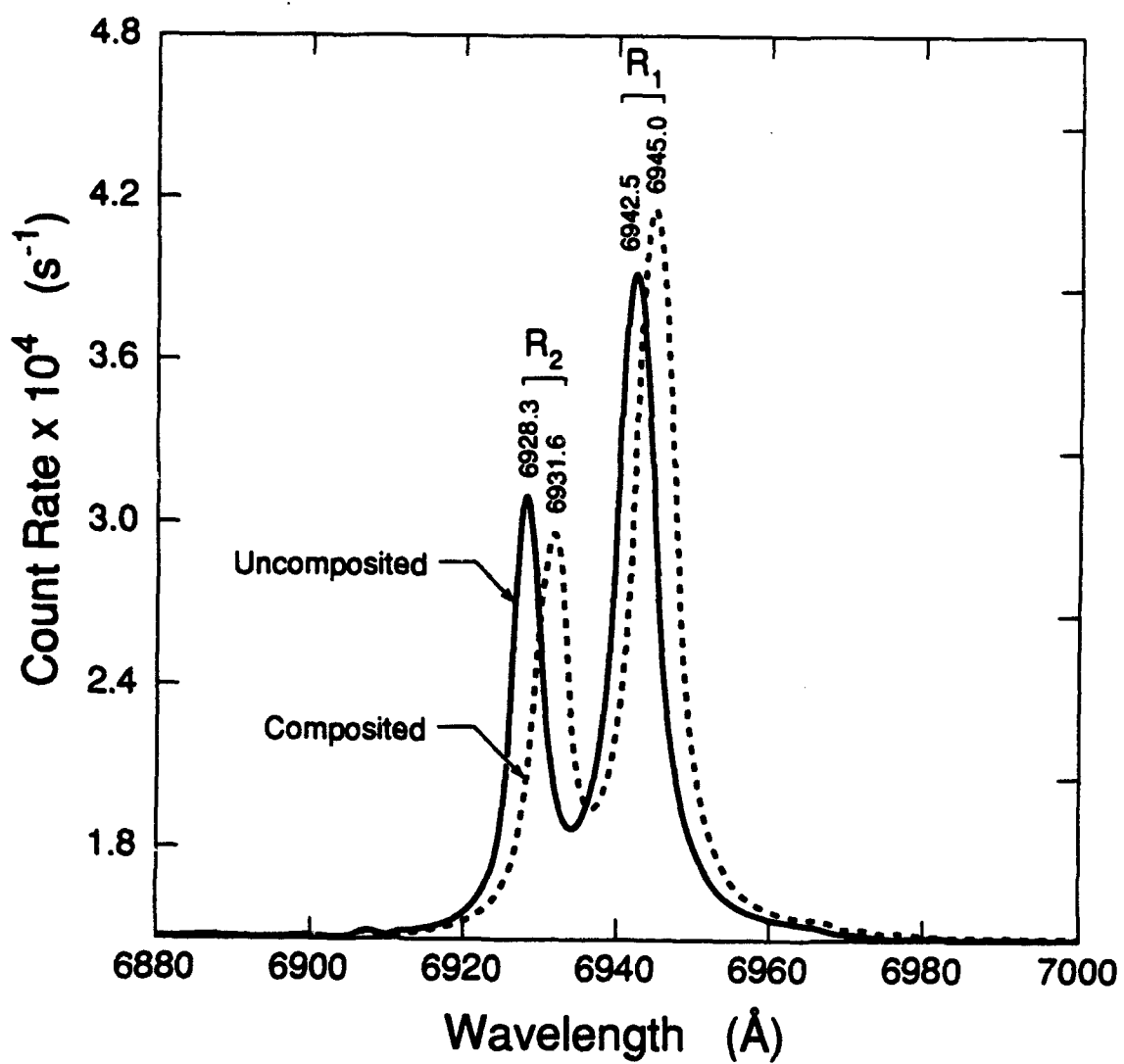


Figure 6. Graph of peak intensity versus wavelength showing a typical peak shift associated with compositing.

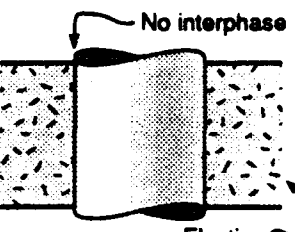
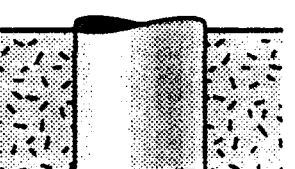
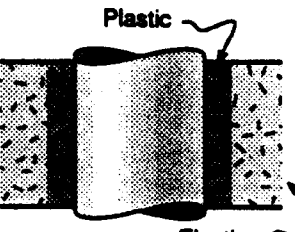
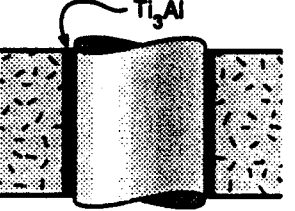
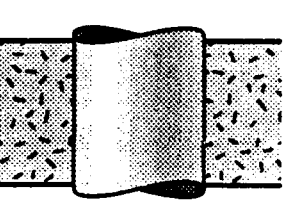
<b>CASE I</b> $\Delta v = -2.92 \text{ cm}^{-1}$		$\alpha_f$ (Saphikon recommended) Isotropic elastic matrix $v_f = 0.2\%$	$\sigma_{rr} (= \sigma_{\theta\theta}) = -194 \text{ MPa}$ $\sigma_{zz} = -869 \text{ MPa}$
<b>CASE II</b> $\Delta v = -2.82 \text{ cm}^{-1}$		$v_f = 1.5\%$	$\sigma_{rr} (= \sigma_{\theta\theta}) = -213 \text{ MPa}$ $\sigma_{zz} = -710 \text{ MPa}$
<b>CASE III</b> $\Delta v = -2.82 \text{ cm}^{-1}$		Elastic / plastic matrix	$\sigma_{rr} (= \sigma_{\theta\theta}) = -193 \text{ MPa}$ $\sigma_{zz} = -869 \text{ MPa}$
<b>CASE IV</b> $\Delta v = -2.93 \text{ cm}^{-1}$		Ti <sub>3</sub> Al interphase	$\sigma_{rr} (= \sigma_{\theta\theta}) = -195 \text{ MPa}$ $\sigma_{zz} = -870 \text{ MPa}$
<b>CASE V</b> $\Delta v = -1.41 \text{ cm}^{-1}$ or $\Delta v = -3.59 \text{ cm}^{-1}$		$\alpha'_f$ (Handbook recommended) or $\alpha''_f$ (Minimum reported values)	$\sigma_{rr} (= \sigma_{\theta\theta}) = -99 \text{ MPa}$ $\sigma_{zz} = -406 \text{ MPa}$ or $\sigma_{rr} (= \sigma_{\theta\theta}) = -244 \text{ MPa}$ $\sigma_{zz} = -1056 \text{ MPa}$

Figure 7. Model predicted R1 line shifts for various sapphire/CP titanium model systems

## OPTICAL FLUORESCENCE FROM CHROMIUM IONS IN SAPPHIRE: A PROBE OF THE IMAGE STRESS

QING MA and D. R. CLARKE

Materials Department, University of California, Santa Barbara, CA 93106, U.S.A.

(Received 7 October 1992)

**Abstract**—The concentration dependent frequency shift of the fluorescence from chromium ions in sapphire is shown to be a direct probe of the image stress produced by the chromium substituting for the smaller aluminium ions in sapphire. Our analysis is based on a comparison of the frequency shift produced when the volume of a sapphire crystal is changed by an external pressure to that produced by a concentration of substitutional solute. The volumetric strain sensed by the fluorescing chromium ion when the lattice is expanded by substitutional solute is approximately one-third of that determined from X-ray lattice parameter measurements, in accord with the Eshelby analysis of the strain field due to a concentration of elastic defects in a finite body.

### 1. INTRODUCTION

The question as to the lattice distortions produced in a crystal by a substitutional solute is of long-standing interest, and has been the subject of considerable intellectual inquiry. Although it has been recognized throughout that the only proper description is one that takes account of the atomic nature of the solute and the appropriate inter-atomic potentials, early investigators did not have available to them this information. In the absence of such information, it was necessary to address the question using continuum descriptions of the solute and its effect on the lattice. One approach, that might be termed the elastic defect model, was to consider a solute as a center of dilatation supplemented by point singularities of higher order. This enabled the methods of continuum elasticity pertaining to centers of pressure to be employed in finding solutions. For example, Bilby modeled an interstitial atom as a misfitting elastic sphere forced into a smaller hole in a material, and derived solutions for the interaction of a solute with a dislocation [1]. Later, Eshelby, in one of the classic papers in materials, provided a rigorous foundation for the elastic defect model by deriving the forces acting on an elastic singularity in a solid [2]. In subsequent seminal papers [3-5], Eshelby set forth a comprehensive framework for the computation of elastic displacements, strains and stresses resulting from the presence of point defects, inclusions, precipitates and transforming regions. By envisaging a series of hypothetical cutting, transforming and welding operations, and the forces and displacements involved, Eshelby formulated analytical expressions for the stresses and strains created by a region transforming but constrained by a surrounding matrix.

Two concepts introduced by Eshelby are of particular importance. One is that inside any finite body

containing defects there exists an additional displacement field, and by extension strain and stress field, that arises from the boundary condition that at the surface of the body the normal stress must be zero. By analogy with electromagnetic fields, Eshelby termed this additional elastic field the image field. The image field is independent of position inside the body and independent of the size of the body. The second key concept was that of the "stress-free" strain, the shape change of the transforming region that would have occurred in the absence of any constraint. (This same strain has been denoted as the "eigenstrain" by Mura [6]. It also appears as the "natural" strain in recent literature on the virtual crystal approximation (VCA) approach to electronic structure calculations [7].) Using the concept of a stress-free transformation strain, Eshelby was able to derive general expressions for the strains produced in the matrix as a result of the transformation as a function of the shape of the ellipsoidal inclusion. The matrix strain is shown to consist of two components, the strain in the matrix if it were of infinite extent and the image strain.

The existence of two components to the strain field in a body containing defects naturally raises the question as to which strains are actually being determined when measuring the lattice parameter by diffraction methods. Although there was, for a period, considerable confusion concerning this question, it now appears resolved that Bragg diffraction methods, using X-rays and neutrons, provide a direct measure of the spatially averaged total strain in the body. (Diffuse scattering provides additional information on the distribution of the lattice distortions but does not include information about average lattice strain.) Since the image strain was shown by Eshelby to be a constant fraction of the total strain, the magnitude of the image strain has been deduced from the concentration dependence of the lattice

parameter. However, there have not been, as far as the authors are aware, any direct measurements of the image strain.

In the course of rather different studies [8–10], directed towards the application of optical fluorescence methods to the measurement of stresses in composite materials, we have, we believe, found that the fluorescence from substitutional solutes of chromium directly probes the image stress in single crystals of sapphire ( $\text{Al}_2\text{O}_3$ ). In this short paper, we describe how we reached this conclusion. It is first necessary, however, to re-examine the data in the literature on the chromium solid solution in aluminum oxide, together with our own experimental data.

## 2. CHROMIUM SUBSTITUTION IN SAPPHIRE

Solid solutions of chromium in aluminum oxide provide a rich data base to re-examine the question of the short-range and long-range distortion induced by the substitution of a mis-fitting solute. In the literature there exist data on the chromium concentration dependence of density [11], lattice parameter determined by X-ray diffraction [11], and frequency of characteristic optical fluorescence lines [12]. In addition, both lattice parameter and fluorescence line shifts as a function of hydrostatic pressure have been reported for selected chromium ion concentrations [13–15]. The system  $\text{Al}_2\text{O}_3$ – $\text{Cr}_2\text{O}_3$  also has the advantage that there is complete solid solution between the two oxide phases [16].

The substitutional nature of the chromium ion has been confirmed by density and X-ray measurements (below). This is consistent with both the existence of the continuous solid solution with  $\text{Cr}_2\text{O}_3$ , the similarity in ionic radius between  $\text{Cr}^{3+}$  (0.064 nm) and  $\text{Al}^{3+}$  (0.057 nm), and the fact that the corundum structure is a rather close-packed structure and does not contain any interstices as large as the chromium ion. Structure analysis as a function of hydrostatic pressure further shows that the corundum structure of sapphire compresses uniformly, with all the distances decreasing equally and all the interatomic angles remaining unchanged [17].

Chromium in sapphire is also a chromophore, giving rise to the characteristic red fluorescence of ruby. The fluorescence originates from electronic transitions in the chromium ion produced by appropriate excitation. Electrons excited from their ground state,  $^4A_2$ , can lose their excess energy by a variety of radiative (and non-radiative) processes. The most pronounced transitions being the  $R$ -fluorescence lines at 1.790 and 1.794 eV in the red. (A recent paper tabulates all the radiative transitions in the visible part of the spectrum [18].) The chromium ion can substitute for any of the aluminum ions in the corundum crystal structure of sapphire with the result that they are octahedrally coordinated to neighboring oxygen and aluminum ions. The octahedron is not regular, but elongated along the  $c$ -axis of the lattice,

resulting in splitting of the  $R$ -fluorescence lines to form the doublet of  $R_1$  and  $R_2$  lines. X-ray refinements [19, 20], in highly doped (4 at.% Cr) sapphire show the chromium ion to be slightly displaced along the  $c$ -axis from the position normally occupied by the aluminum ion so that the chromium site symmetry is further reduced, but nevertheless retains a three fold rotational symmetry about the  $c$ -axis. The effect of an applied stress is to distort the crystal field surrounding the chromium ion, change its potential energy and thereby alter the energies of the radiative transitions.

### 2.1. Optical fluorescence data

The frequencies of the  $R_1$  and  $R_2$ , as well as the extended neighbor fluorescence  $N$  lines, have all been reported to shift with pressure and with chromium concentration. The pressure dependence is well known [13, 14] and continues to be subject to further refinement because of its central importance as a pressure gauge for high pressure studies. The reported pressure dependence of the frequency shift  $\Delta\nu$  may be expressed as

$$\Delta\nu = -(2\Pi_{11} + \Pi_{33})P \quad (1)$$

where  $\Pi_y$  is the piezo-spectroscopic coefficient. The original work of Forman *et al.* [13] is reproduced in Fig. 1(a) for the  $R_1$  line with the sum  $2\Pi_{11} + \Pi_{33}$  having a value of  $7.7 \text{ cm}^{-1} \text{ GPa}^{-1}$ . The results for  $R_2$  line is very similar and therefore not included here. Recent work, examining the fluorescence from beams loaded in four point bending, has shown that the equation is equally valid for tension [8, 9].

The chromium concentration dependence of the fluorescence energy has been the subject of just one previous study [12]. Our own results have proven to be essentially identical to those of Kaplyanskii *et al.* [12], which are reproduced in Fig. 1(b). The data may be expressed by the linear dependence

$$\Delta\nu = 99c_m \quad (2)$$

where  $\Delta\nu$  is measured in wavenumber and  $c_m$  is the chromium concentration (in wt%).

### 2.2. X-ray lattice parameter measurements

X-ray lattice parameter measurements have been made as a function of pressure on rubies with a number of different chromium concentrations [15, 17, 18]. These studies indicate an isotropic compressibility with the interatomic distances decreasing equally with pressure and the interatomic angles remaining unchanged up to at least 4.6 GPa [17]. The results of d'Amour *et al.* [15] is shown in Fig. 1(c), which can be fitted to the following linear relations

$$a = 0.47664(1 - 0.001173P)$$

and

$$c = 1.3007(1 - 0.001332P) \quad (3)$$

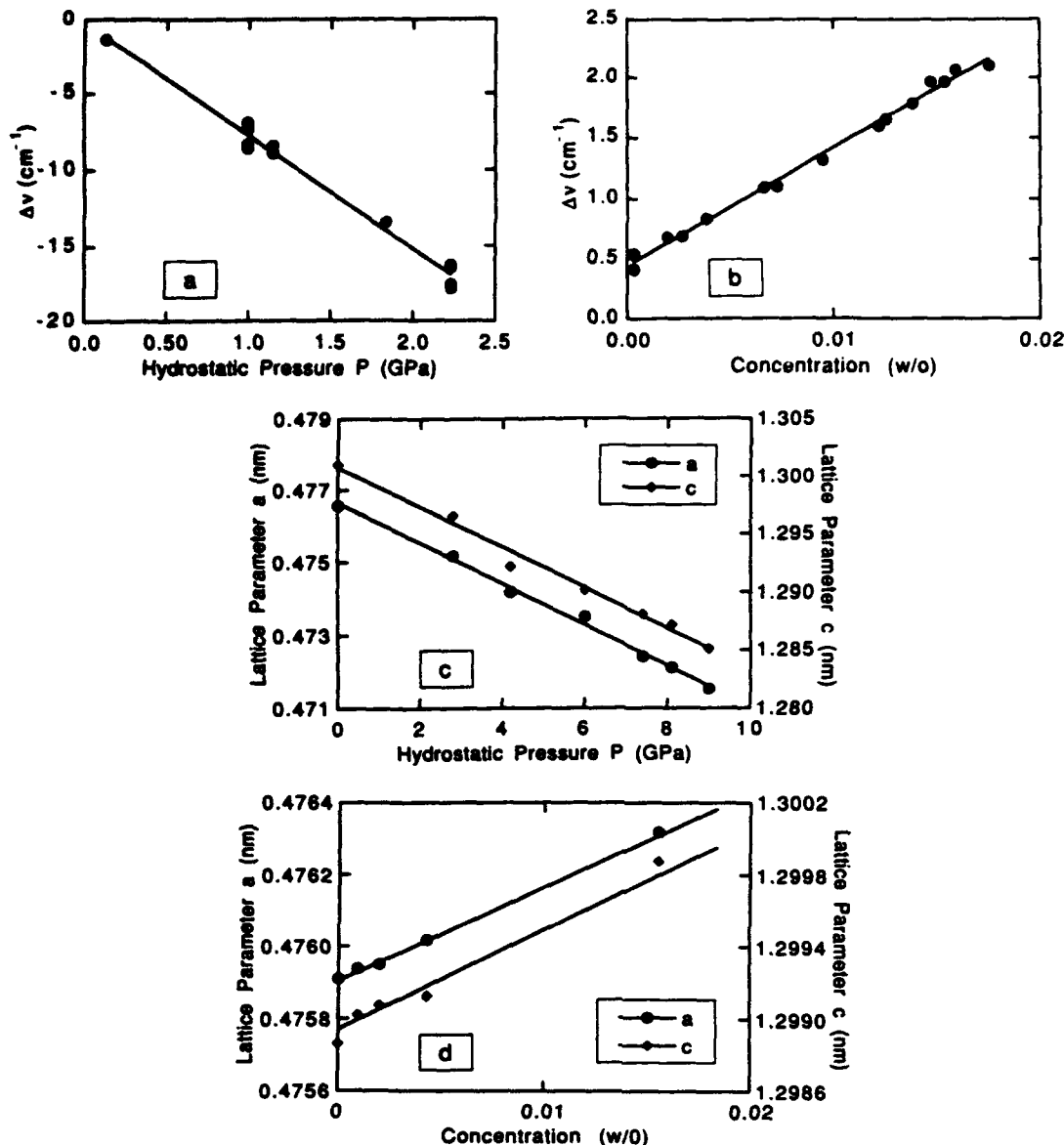


Fig. 1. Data on the chromium solid solution in aluminum oxide. (a) Pressure dependence of frequency shift for the  $R_1$  fluorescence line [13]. (b) Concentration dependence of frequency shift for the  $R_1$  fluorescence line [12]. (c) Pressure dependence of the lattice parameters of sapphire [15]. (d) Concentration dependence of the lattice parameters of sapphire [11].

where the lattice parameters  $a$  and  $c$  are measured in nanometers, and  $P$  is measured in GPa. They also found that the density increased with increasing pressure according to the Murnaghan equation of state.

The X-ray lattice parameter measurements were also made as a function of chromium concentration [11] [Fig. 1(d)], over a range of chromium concentration up to 2 wt% by Jan *et al.* They indicate that the lattice parameters and derived density are given by the linear relationship

$$a = 0.47591(1 + 0.0527c_m)$$

$$c = 1.29894(1 + 0.0452c_m)$$

and

$$\rho_x = 3.9864(1 + 0.340c_m) \quad (4)$$

where the density  $\rho_x$  is measured in g/cm<sup>3</sup>.

### 2.3. Density data

Jan *et al.* have also made precision density measurements [11] using the pycnometry technique. Their results indicate a linear dependence of the density on the chromium concentration given by the relationship

$$\rho = 3.9860(1 + 0.341c_m). \quad (5)$$

The linear dependence, as clearly shown in Fig. 2, is consistent with chromium being a substitutional solute

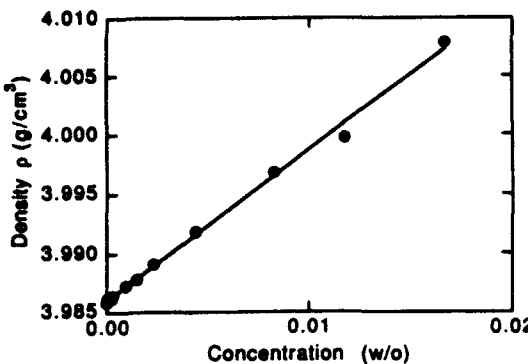


Fig. 2. Linear dependence of the density of alumina oxide on the chromium concentration [11].

[21]. The physical density determined above is, within experimental error, the same as the X-ray density measurements by Jan *et al.* in equation (4). This demonstrates the equivalence of the solute induced macroscopic strain and the mean strain measured by X-ray.

#### 2.4. Frequency shift as a function of mean strain

From the results presented in Fig. 1, the frequency shift can be related to the mean volumetric strain  $\Delta V/V$  by using the following relationship

$$\frac{\Delta V}{V} = 2 \frac{\Delta a}{a} + \frac{\Delta c}{c}.$$

Therefore, from equations (1) and (3), and equations (2) and (4), we obtain the following expressions for the fluorescence shifts

$$\begin{aligned}\Delta v^P &= 2100 \frac{\Delta V}{V} \\ \Delta v^D &= 660 \frac{\Delta V}{V}\end{aligned}\quad (6)$$

depending on whether the strain is produced by an external pressure or by solute doping. The superscripts P and D denote pressure and solute doping respectively.

### 3. ANALYSIS AND DISCUSSION

The intriguing feature of the data assembled in the previous section is that the apparent strain sensed by a fluorescing chromium ion is different depending on whether the lattice is strained by the application of a hydrostatic pressure or internally by the addition of substitutional solute. Specifically, for the same lattice strain measured by changes in the lattice parameter by X-ray diffraction the frequency shift of the chromium line produced by doping is about one-third [equation (6)] that produced by an applied pressure

$$\Delta v^D \sim \frac{1}{3} \Delta v^P \quad (7)$$

We believe that the different pressure and solute concentration effects may be reconciled by postulat-

ing that the frequency shift of the fluorescence lines is sensitive to the image strain whereas X-ray diffraction monitors the average lattice strain. To prove this, we proceed to perform a set of imaginary experiments (Fig. 3), assuming for simplicity that the medium is elastically isotropic and that the concentration of solute is sufficiently small that any solute interaction effects, such as dipolar or higher, can be ignored.

We start with a body of sapphire of volume  $V$ , free of external pressure ( $P = 0$ ), containing only a few  $\text{Cr}^{3+}$  ions to sense the strain, so that the solute concentration  $f \rightarrow 0$ . The frequency of the fluorescence line is

$$v = v(P = 0, f \rightarrow 0). \quad (8)$$

This frequency is expected to be, in a complicated manner, dependent on the local strain in the vicinity of each  $\text{Cr}^{3+}$  ion as it is a substitutional solute, larger than the  $\text{Al}^{3+}$  ion it replaces. Fortunately, by choosing this state as the reference state, a knowledge of the effect of this local strain is unimportant since it is the same for both the state of interest and the reference state and hence cancels out.

In the first experiment, a hydrostatic tensile stress  $-P$  is applied to the body, so that its volume increases by  $\Delta V$ . The strain dependence (due to an applied stress  $-P$ ) of the frequency shift [9] for an isotropic material can be in general expressed as

$$\Delta v = \lambda \epsilon_u \quad (9)$$

where the convention of summation of repeated indices is assumed and where  $\lambda$  is the piezo-spectro-

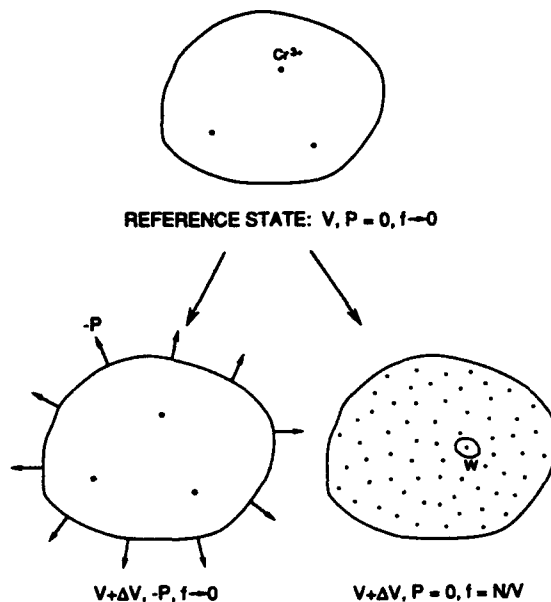


Fig. 3. Illustration of a set of imaginary experiments to produce a volume change by either external stress or solute doping. The region  $W$  is small but finite volume of arbitrary size that contains a single probe ion used to monitor the strain.

scopic volumetric strain coefficient. Therefore, the frequency shift due to the stress  $-P$  is simply

$$\Delta\nu^P = \nu(-P, f \rightarrow 0) - \nu(P = 0, f \rightarrow 0)$$

$$= \lambda \frac{\Delta V}{V}. \quad (10)$$

Alternatively, in the second experiment, we can produce such a volume change by increasing the number of  $\text{Cr}^{3+}$  ions in the body from virtually zero in our reference state to  $N$ , distributed at random. Following Eshelby, the displacement field generated in an infinite body by all the substitutional ions may be written as

$$\mathbf{u}^x(\mathbf{r}) = C \sum_a^N \frac{\mathbf{r} - \mathbf{r}_a}{|\mathbf{r} - \mathbf{r}_a|^3} \quad (11)$$

where  $C$  is the dilatational strength of an individual  $\text{Cr}^{3+}$  ion, proportional to its misfit.

In a finite crystal, the displacements are modified by the existence of the image term, required so that the tractions at the external surface are zero. The additional displacement at position  $\mathbf{r}$  produced by the image force is [3]

$$\mathbf{u}^{\text{im}}(\mathbf{r}) = \frac{8\pi(1-2\sigma)}{3(1+\sigma)} \frac{CN}{V} \mathbf{r} \quad (12)$$

where  $\sigma$  is Poisson's ratio. The total displacement is then the sum of these two displacements

$$\mathbf{u}^{\text{total}}(\mathbf{r}) = C \sum_a^N \frac{\mathbf{r} - \mathbf{r}_a}{|\mathbf{r} - \mathbf{r}_a|^3} + \frac{8\pi(1-2\sigma)}{3(1+\sigma)} \frac{CN}{V} \mathbf{r}. \quad (13)$$

The volume change produced by the solute is then simply the integral of the displacement field over the surface of the body

$$\begin{aligned} \Delta V &= \int_V \mathbf{u}^{\text{total}}(\mathbf{r}) \cdot d\mathbf{s} \\ &= 4\pi CN \frac{3(1-\sigma)}{1+\sigma} = 4\pi CN\gamma. \end{aligned} \quad (14)$$

From this volume change, the mean strain in the body produced by solute doping is

$$\bar{\epsilon}_u = \frac{\Delta V}{V} = 4\pi\gamma C \frac{N}{V} = 4\pi\gamma Cf \quad (15)$$

where  $f$  is the concentration of  $\text{Cr}^{3+}$ .

However, the strain field sensed by an individual substitutional ion is different from that described above as we now show. Consider a small but finite volume element,  $W$ , of arbitrary size but which does not contain any solute ions other than a single probe ion whose fluorescence we may use to monitor the state of this small volume element. The volume expansion (due to doping in the body) of this element of volume may be written as before as

$$\Delta W = \int_W \mathbf{u}^{\text{total}}(\mathbf{r}) \cdot d\mathbf{s} - \int_W \mathbf{u}^{\text{probe}}(\mathbf{r}) \cdot d\mathbf{s}. \quad (16)$$

In this equation, the first term gives the contribution of the total displacement field, which includes the

image term due to all substitutional ions [equation (12)], and the displacement field due to the probing ion itself, since the displacements due to other ions in equation (11) not included in  $W$  do not contribute to the integration. Because the displacements generated by the probing ion are already in the reference state, to which the volume change is being compared, its contribution is subtracted by the second term in the equation (16). So, effectively, only the image displacement field due to the presence of all substitutional ions in the body contributes to  $\Delta W$ . We may then write

$$\Delta W = \frac{8\pi(1-2\sigma)}{1+\sigma} WCf. \quad (17)$$

Therefore, the strain sensed by the solute ion is simply the image strain

$$\epsilon_u^{\text{im}} = \frac{\Delta W}{W} = 4\pi(\gamma-1)Cf. \quad (18)$$

Comparing with equation (15), the corresponding frequency shift of the fluorescence from the sensing solute ion would then be

$$\begin{aligned} \Delta\nu^D &= \nu\left(P = 0, f = \frac{N}{V}\right) - \nu(P = 0, f \rightarrow 0) \\ &= \lambda\epsilon_u^{\text{im}} = \lambda \frac{\gamma-1}{\gamma} \bar{\epsilon}_u = \lambda \frac{\gamma-1}{\gamma} \frac{\Delta V}{V}. \end{aligned} \quad (19)$$

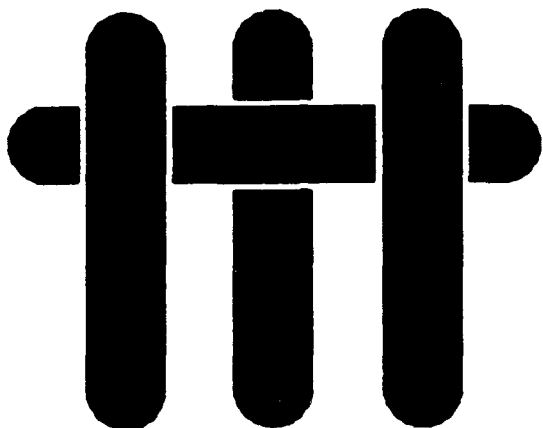
If one assumes that the Poisson's ratio is  $1/3$ , then a comparison of equations (10) and (19) indicates that the effect of solute concentration on the fluorescence shift is about  $1/3$  that produced by an external pressure, as found experimentally [equation (6)]. Since in the case of solute concentration, the strain affecting the shift is entirely due to the image term, we therefore conclude that the fluorescence probes the image strain whereas X-ray diffraction provides a measurement of the total strain.

**Acknowledgements**—This work was supported by the Office of Naval Research under grant N00014-91-J-1875. The authors are grateful to Dr I. Tanaka, Osaka University, for providing a number of the synthetic rubies used in this work.

## REFERENCES

- B. A. Bilby, *Proc. Phys. Soc. A* **63**, 191 (1950).
- J. D. Eshelby, *Phil. Trans. R. Soc. A* **244**, 87 (1951).
- J. D. Eshelby, *J. appl. Phys.* **25**, 255 (1954).
- J. D. Eshelby, in *Solid State Physics* (edited by F. Seitz and D. Turnbull), Vol. 3, p. 79. Academic Press, New York (1956).
- J. D. Eshelby, *Proc. R. Soc. A* **241**, 376 (1957).
- T. Mura, *Micromechanics of Defects in Solids*. Martinus Nijhoff, The Hague (1982).
- J. L. Martin and A. Zunger, *Phys. Rev. B* **30**, 6217 (1984).
- S. E. Molis and D. R. Clarke, *J. Am. Ceram. Soc.* **73**, 3189 (1990).
- Q. Ma and D. R. Clarke, *J. Am. Ceram. Soc.*, in press.
- Q. Ma and D. R. Clarke, *Acta metall. mater.* **41**, 1817 (1993).
- J.-P. Jan, S. Steinemann and P. Dinichert, *Helv. Phys. Acta* **33**, 123 (1960).

12. A. A. Karlyanskii, A. K. Przhevuskii and R. B. Rozenbaum, *Soviet Phys. Solid St.* **10**, 1864 (1969).
13. R. A. Forman, G. J. Piermarini, J. D. Barnett and S. Block, *Science* **176**, 284 (1972).
14. G. J. Piermarini, S. Block, J. D. Barnett and R. A. Foreman, *J. appl. Phys.* **46**, 2774 (1975).
15. H. D'Amour, D. Schiferl, W. Denner, H. Schulz and W. B. Holzapfel, *J. appl. Phys.* **49**, 4411 (1978).
16. *Phase Diagrams for Ceramists*. The American Ceramic Society, Columbus, Ohio (1969).
17. L. W. Finger and R. M. Hazen, *J. appl. Phys.* **49**, 5823 (1978).
18. J. H. Eggert, K. A. Goettel and I. F. Silvera, *Phys. Rev. B* **40**, 5724 (1989).
19. S. C. Moss and R. E. Newnham, *Z. Kristallogr.* **120**, 359 (1964).
20. J. W. McCauley and G. V. Gibbs, *Z. Kristallogr.* **135**, 453 (1972).
21. R. W. Balluffi and R. O. Simmons, *J. appl. Phys.* **31**, 2284 (1960).



## **RESIDUAL STRESSES IN $\text{Al}_2\text{O}_3$ - $\text{ZrO}_2$ COMPOSITES: A TEST OF STOCHASTIC STRESS MODELS**

**Qing Ma, Wolfgang Pompe\*, John D. French\*\* and David R. Clarke**

Materials Department  
University of California, Santa Barbara, CA

\*Materials Science Department, Technical University of Dresden, Dresden, Germany

\*\* Ceramics Division, National Institute of Standards and Technology, Gaithersberg, MD

### **Abstract**

In cooling sintered composites of  $\text{Al}_2\text{O}_3$ - $\text{ZrO}_2$  from their fabrication temperature residual stresses are created as a result of both the difference in thermal expansion between the two phases and the crystallographically anisotropic thermal expansion of the  $\text{Al}_2\text{O}_3$  phase. In this work the first and second moments of the residual stress distribution have been measured as a function of volume fraction of zirconia from 0.01 to 0.90. The measurement technique used is piezo-spectroscopy based on the optical fluorescence from  $\text{Cr}^{3+}$  dopants in the alumina phase. For zirconia volume fractions up to 0.35 the average stress accurately fits the predictions given by the upper Hashin bound and this fit provides a value of the average thermal strain in the composites. Using this value, the effective medium approximation produces an excellent description of the average stress over the entire volume fraction. It is also shown that the fluorescence broadening due to stress fluctuations lies close to the predicted upper and lower Hashin bounds modified by the restrictions imposed by the principle of maximum entropy. The measured moments and those predicted by stochastic stress analysis compare well suggesting that the stochastic analysis provides a reliable method of calculating residual stresses in composites.

## 1 Introduction

The determination of the average elastic properties of composite and polycrystalline materials is one of the classical problems in the mechanics of materials. Over the years a variety of bounds on the elastic modulus have been established, ranging from the early Voigt and Reuss bounds [1], to the Hashin-Shtrikman bounds [2] and more recently a variety of generalized effective medium equations [3]. Whilst much of the attention has been focused on predicting the elastic modulus of two- (or multi-) phase materials from the elastic properties of the constitutive phases, the models also allow, in principle, the calculation of the stress distribution in the phases [3,4,5]. However, since the calculation of residual stresses can be complex, three quite distinct approaches have been adopted depending on the type of information about the residual stresses desired. One is the approach embodied in the Eshelby calculation of the strain field due to a misfitting inclusion [4,6]. Once a stress free transformation strain and the shape of the inclusion is specified, the stress field throughout the material can be calculated in detail. The analysis can then be extended to a composite containing other inclusions by the linear superposition of stresses using assumptions about the distribution of the inclusions [4]. The second approach is to presume some particular geometry of the inclusions and their arrangement and compute the detailed stress distribution by application of large-scale finite element methods [7]. The third approach is to describe the spatial distribution of stresses by statistical methods [3]. The stress field is described by an appropriate probability functional from which the average value of the stresses (in the various phases) are expressed in terms of the first moments of the stress distribution. Similarly, the spatially varying stresses are expressed in terms of the second moment of the distribution. In the framework of these stochastic models, the morphology of the microstructure and the spatial variation of phases are described in terms of appropriate correlation functions. By applying the maximum entropy principle, further restrictions can be placed on the properties of the statistical distribution and

hence on the first and second moments of the stress distribution.

Although it might be expected that such a statistically-based approach might be most appropriate in describing the average stresses in a polycrystalline, two- (or multi-) phase material the predictions have yet to be critically tested by experiment. In this contribution we attempt to provide such a test using measurements of the optical fluorescence shifts from the alumina phase (A) in a series of  $\text{Al}_2\text{O}_3$ - $\text{ZrO}_2$  composites in which the volume fraction of the cubic zirconia phase (Z) is varied. The composites were prepared by sintering of alumina and cubic zirconia particles and as a result the spatial distribution of grains is essentially disordered (figure 1). In this material system residual stresses form on cooling due to both the thermal mismatch between the alumina and zirconia phases and the crystallographic thermal contraction anisotropy of the alumina material. Since both phases have very high yield stresses, the residual stresses are believed to be accommodated elastically to a large extent. Furthermore, the yttrium doping of the zirconia ensures that it remains cubic and no phase transformation can occur on cooling.

The technique of optical fluorescence is used to determine the stress distribution in the alumina grains in the composite. The particular fluorescence used is the  $\text{R}_2$  fluorescence line from electronic transitions of  $\text{Cr}^{3+}$  substitutional dopants in the alumina, excited by an optical probe. The theoretical basis of the fluorescence technique has been described in detail in an earlier publication [8]. Briefly, the frequency shift of a characteristic fluorescence line is stress dependent and is given by:

$$\Delta\nu = \Pi_{ij} \sigma_{ij}^* \quad (1)$$

where  $\Pi_{ij}$  are the piezo-spectroscopic coefficients relating the frequency shift to the stress, and  $\sigma_{ij}^*$  is the stress tensor represented in the crystallographic coordinate frame. As shown earlier, for a polycrystalline material, the shift in fluorescence frequency  $\langle \Delta\nu \rangle$  is a measure of the first moment of the stress distribution and the broadening of the fluorescence peak  $\sqrt{\langle \Delta\nu^2 \rangle}$  is

dependent on the second moment of the stress distribution. By using a probe large compared to the grain size and by utilizing the extensive multiple scattering of the light within the composite, the fluorescence signal is obtained from a very large number of grains. Thus, by measuring the fluorescence peak the first and second moments of the stress distribution from the material can be obtained directly and compared with the predictions of the stochastic stress analysis.

## 2 Stochastic Analysis of Residual Stresses In Two-Phase

### Materials

In this section we outline the principal results of the stochastic analysis of the stresses in two-phase materials appropriate to a composite of  $\text{Al}_2\text{O}_3$ - $\text{ZrO}_2$  [3]. The underlying assumptions being that the stress distribution in the composite can be described by a probability functional and that the spatial and angular distributions of the zirconia and alumina grains are random. The emphasis is on the first and second moments of the stress distribution since they are those that are measured directly by the fluorescence technique.

To apply the stochastic stress analysis, a series of restrictions can be imposed so as to successively refine the predictions. The first step is a general statement of the first and second moments of the stress distribution in terms of the elastic strain energy,  $u$ , stored in the stress field. As will be described below, the elastic strain energy,  $u$ , depends on the effective elastic modulus of the composite, which in turn depends on the topological distribution of the constituent phases. By considering two extreme topologies corresponding to the upper and lower bounds on the elastic moduli, limits on the magnitude of the residual stress distribution can be established. The Hashin bounds are used in this work as the microstructure appears to be random. Lastly, a further restriction on the stress distribution is imposed by invoking the principle of maximum entropy. The values for the resulting stress distribution depend on the topological nature of the phase distri-

bution, but for the  $\text{Al}_2\text{O}_3$ - $\text{ZrO}_2$  system the upper and lower bounds appear to be close to one another.

To begin, the residual stress field needs to be defined and from it the stored elastic strain energy expressed. In the  $\text{Al}_2\text{O}_3$ - $\text{ZrO}_2$  material, the residual stresses are a result of both the anisotropic thermal expansion of the alumina grains and the difference in thermal expansion between the alumina and zirconia phases. The residual stress in any particular alumina grain, whose crystallographic axes are oriented at an angle  $\Omega$  to a fixed coordinate, can then be written as the linear superposition of two parts:

$$\sigma_{ik}(x) = \sigma_{ik}^i(x) + \sigma_{ik}^a(x|\Omega) \quad (2)$$

where  $\sigma_{ik}^i(x)$  denotes the stress in the alumina averaged over all possible crystallographic orientations of the grains and therefore corresponds to the isotropic component (*i*) due to the presence of  $\text{ZrO}_2$  grains, and  $\sigma_{ik}^a$  gives the orientation dependent part, corresponding to the anisotropic component (*a*) of the stress distribution due to the thermal anisotropy. These two components can be considered separately in the following.

Given the residual stress, the elastic strain energy can be expressed [3] by the relationship:

$$2u = - \langle \sigma_{ik}\epsilon_{ik}^T \rangle = 2u^i + 2u^a \quad (3)$$

with

$$2u^i = (\epsilon_Z^T - \epsilon_A^T)(S_A - S_Z)^{-1}(\epsilon^* - \bar{\epsilon}^T) \quad (4)$$

where  $S_A$  and  $S_Z$  are the elastic compliance tensors,  $\epsilon_A^T$  and  $\epsilon_Z^T$  are the average stress free strain tensors of the  $\text{Al}_2\text{O}_3$  and  $\text{ZrO}_2$  phases,  $\epsilon^*$  is the macroscopic stress free strain tensor, and  $\bar{\epsilon}^T = v_A\epsilon_A^T + v_Z\epsilon_Z^T$  ( $v_A$  and  $v_Z$  are the volume fractions of  $\text{Al}_2\text{O}_3$  and  $\text{ZrO}_2$ ) [3]. The anisotropic component

of strain energy is given by

$$2u^a = 3 \frac{(e^* - e^T)(e_c^T - e_a^T)}{S_a - S_c} \quad (5)$$

where  $e^T = \frac{1}{3}(2e_a^T + e_c^T)$  is the hydrostatic component of  $e_A^T$ , and  $e_a^T$  and  $e_c^T$  are the stress free strains in the alumina grains in the directions of transversal isotropy, and in the 3-direction (corresponding to the  $a$ - and  $c$ - crystallographic axes of the trigonal lattice of sapphire). The terms  $S_a = S_{11kk}$ ,  $S_c = S_{33kk}$  are sums of components of the elastic compliance tensor and  $e^*$  is the isotropic macroscopic stress free strain (assuming no texture).

According to the work of Kreher and Molinari [9], the first and second moments of the stress distribution in a heterogeneous solid can be quite generally expressed in terms of the stored elastic strain energy in the stress field by the following relationships:

$$v_r < \sigma_r > \delta(\epsilon_{ik}^T)_r = -\frac{\partial u}{\partial(\epsilon_{ik}^T)_r} \delta(\epsilon_{ik}^T)_r \quad (6)$$

$$v_r < \sigma_r \delta S_r \sigma_r > = -2 \frac{\partial u}{\partial(S_{iklm})_r} \delta(S_{iklm})_r \quad (7)$$

where  $\delta(\epsilon_{ik}^T)_r$ , and  $\delta S_r$ , describe virtual variations of the stress free strain and elastic compliance tensor of the particular phase  $r$ .

For clarity of exposition, the evaluation of the first and second moments of the stress distributions are considered separately below.

## 2.1 Average Stress

The average stress in the alumina grains can be expressed as the stresses in equation 2 averaged over all the alumina grains in the material. This is given by the first moment of the stress distribution over the ensemble of grains:

$$< \sigma_{ik} >_A = < \sigma_{ik}^i >_A + < \sigma_{ik}^a | \Omega >_A \quad (8)$$

where  $\langle \sigma_{ik}^i \rangle_A$  is the first moment of the isotropic stress field and  $\langle \sigma_{ik}^a | \Omega \rangle_A$  is the first moment of the distribution for orientation-dependent part of the stress field due to anisotropy of  $\text{Al}_2\text{O}_3$ .

The isotropic part of the average stress in  $\text{Al}_2\text{O}_3$  is simply given in terms of the effective modulus by the expression:

$$\langle \sigma_{ik}^i \rangle_A = s_A \delta_{ik} \quad (9)$$

$$s_A = -\frac{3}{v_A} \frac{K_A K_Z}{K_A - K_Z} \left( v_Z - \frac{K_Z}{K^*} \frac{K_A - K^*}{K_A - K_Z} \right) (\alpha_A - \alpha_Z) \Delta T \quad (10)$$

with

$$\alpha_A = \frac{2\alpha_a + \alpha_c}{3} \quad (11)$$

$\Delta T$  is the temperature drop over which the residual stresses are created on cooling. From force balance condition, the average stress in the zirconia grains is given by

$$v_Z \langle \sigma_{ik}^i \rangle_Z + v_A \langle \sigma_{ik}^i \rangle_A = 0 \quad (12)$$

Since the zirconia phase is cubic,  $\langle \sigma_{ik}^i \rangle_Z$  is the total average stress in zirconia grains. The effective modulus  $K^*$  is a function of the elastic constants of the two phases, and their volume fractions as well as the topological arrangement.

Assuming that the microstructure is statistically isotropic, the effective bulk modulus  $K^*$  is restricted to lie between the upper and lower Hashin limits,  $K^+ > K^* > K^-$ . The upper limit corresponds to a self-similar composite sphere topology in which  $\text{ZrO}_2$  inclusions are embedded within a  $\text{Al}_2\text{O}_3$  matrix. The lower limit corresponds to  $\text{Al}_2\text{O}_3$  inclusions embedded within  $\text{ZrO}_2$ . The Hashin limits may be expressed in terms of the volume fraction of  $\text{Al}_2\text{O}_3$  by the equations [3]:

$$K^+ = v_A K_A + v_Z K_Z - v_A v_Z \frac{(K_A - K_Z)^2}{v_A K_Z + v_Z K_A + 4/3 G_A} \quad (13)$$

$$K^- = v_A K_A + v_Z K_Z - v_A v_Z \frac{(K_A - K_Z)^2}{v_A K_Z + v_Z K_A + 4/3 G_Z} \quad (14)$$

where  $K$  and  $G$  are the bulk and shear moduli of the constituent phases. Whereas the effective Young's moduli for the different topologies differ by less than 5 percents, the predicted average stresses corresponding to the alternative topologies differ considerably more. Using the upper and lower Hashin limits for the effective modulus in equation 10, the average stress can be rewritten as

$$\sigma_A = -3v_Z K (\alpha_A - \alpha_Z) \Delta T \quad (15)$$

with (a) for the upper Hashin limit,

$$K^+ = (v_Z/K_A + v_A/K_Z + 3/4G_A)^{-1} \quad (16)$$

(b) for the lower Hashin limit,

$$K^- = (v_Z/K_A + v_A/K_Z + 3/4G_Z)^{-1} \quad (17)$$

As will be shown in figure 5, the two topologies are characterized by significantly different average internal stresses.

The upper and lower Hashin limits for the effective modulus are related to the so-called effective field approximation (EFA) for the internal stress field. In this approximation, one of the components is the matrix phase while the other is the inclusion phase. For a microstructure of random distribution of the two phases, the effective medium approximation (EMA) often describes the topology more satisfactorily [3]. In contrast to the Hashin topologies, interconnecting networks of grains are a feature of topologies for intermediate volume fractions in the EMA method. The effective bulk modulus of a composite according to the effective medium approximation (EMA)

fulfills the following condition:

$$K^+ > K^{EMA} > K^-$$

and it normally has to be evaluated numerically, as is done later. As will be shown figure 5, the average stress calculated by EMA is shown to have values intermediate between the two Hashin bounds.

The first moment of the anisotropic part of the stress field, that due to the thermal misfit between the differently oriented alumina grains, can be expressed as:

$$\langle \sigma_{11}^a | \Omega \rangle = \langle \sigma_{22}^a | \Omega \rangle = \frac{2}{3} G_E (\alpha_c - \alpha_a) \Delta T \equiv \langle \sigma_a^a \rangle \quad (18)$$

$$\langle \sigma_{33}^a | \Omega \rangle = -\frac{4}{3} G_E (\alpha_c - \alpha_a) \Delta T \equiv \langle \sigma_c^a \rangle \quad (19)$$

with

$$G_E = \frac{G_A (9K_A + 8G_A)}{5(3K_A + 4G_A)} \quad (20)$$

This expression is valid provided the alumina grains are randomly oriented and the elastic anisotropy of alumina is small, which it is [10].

Thus, combining the above equations, the average stress in the alumina grains along the *a*- and *c*- crystallographic directions can be written as:

$$\langle \sigma_a \rangle_A = -3v_Z K (\alpha_A - \alpha_Z) \Delta T + \frac{2}{3} G_E (\alpha_c - \alpha_a) \Delta T \quad (21)$$

$$\langle \sigma_c \rangle_A = -3v_Z K (\alpha_A - \alpha_Z) \Delta T - \frac{4}{3} G_E (\alpha_c - \alpha_a) \Delta T \quad (22)$$

where *K* has the value given in equations 16 and 17, appropriate to the topological description of the material microstructure.

## 2.2 Stress Fluctuations

The second moment of the stress distribution describes the spatial fluctuation of the residual stresses, and as described in reference [8] is characterized by the width of the fluorescence peak. Using the separation of stresses described by equation 2, the second moment can be expressed [3] as:

$$\langle \sigma_{ik} \sigma_{ik} \rangle = \langle \sigma_{ik}^i \sigma_{ik}^i \rangle + 2 \langle \sigma_{ik}^i \sigma_{ik}^a \rangle + \langle \sigma_{ik}^a \sigma_{ik}^a \rangle \quad (23)$$

If the cross-correlation of the two stress fields is small relative to the other two terms, it can be neglected and the second moment becomes:

$$\langle \sigma_{ik} \sigma_{ik} \rangle = \langle \sigma_{ik}^i \sigma_{ik}^i \rangle + \langle \sigma_{ik}^a \sigma_{ik}^a \rangle \quad (24)$$

In order to derive an expression for the second moment of a particular stress component, we assume that the second order stress invariant equals the sum of the second order moments of the three principle stresses defined in the lattice coordinate of a given crystal. This ignores any possible correlation between the second order moments of the shear stresses with the surroundings. By making the further assumption that the magnitude of the fluctuations in each of the three isotropic principle stresses is the same, then the second order moments may be written as:

$$\langle \sigma_{11}^{i2} \rangle = \langle \sigma_{22}^{i2} \rangle = \langle \sigma_{33}^{i2} \rangle = \langle \sigma_{11} \rangle^2 + \sigma_w^{i2} \quad (25)$$

These values of the second order moments for the isotropic components  $\sigma_{ik}^i$  can now be obtained explicitly by imposing limits to the phase topology using the Hashin bounds on the modulus. Using equation 4 and 7, the upper limit is given by the upper Hashin bound, namely

$$\sigma_w^{i+} = 3\left(\frac{t_z}{2}\right)^{1/2} K^+ (\alpha_A - \alpha_Z) \Delta T \quad (26)$$

The lower bound corresponds to  $\text{Al}_2\text{O}_3$  as the embedded inclusion. Since in this geometry the stress in the inclusion is purely hydrostatic, the stress fluctuations are necessarily zero, i.e.,

$$\sigma_w^{I-} = 0 \quad (27)$$

Both limits are shown in figure 6.

The second order moments for the isotropic stress can be refined by application of the maximum entropy principle of the information theory [3]. The calculation takes into account of all possible topologies which are compatible with a given set of macroscopic thermal-elastic properties, i.e., effective modulus and stress free stain. Under the assumption of the effective medium approximation, i.e., only one phase forms a continuous network (composite sphere topology), two functions corresponding to the upper and lower Hashin bounds are derived

$$\sigma_w^{I+} = \frac{3}{2}(v_A v_Z)^{1/2} \left( \frac{3K_A + 4G_A}{6G_A} \right)^{1/2} \mathcal{K}^+(\alpha_A - \alpha_Z) \Delta T \quad (28)$$

$$\sigma_w^{I-} = \frac{3}{2}(v_A v_Z)^{1/2} \left( \frac{3K_A + 4G_A}{6G_Z} \right)^{1/2} \mathcal{K}^-(\alpha_A - \alpha_Z) \Delta T \quad (29)$$

These two functions, evaluated for the  $\text{Al}_2\text{O}_3\text{-ZrO}_2$  composite, are plotted in figure 6, where they are compared with our experimental data.

A further restriction can be imposed by applying the maximum entropy principle to the stress variation and using the macroscopic thermal-elastic properties derived from the effective medium approximation, rather than those given by the Hashin bounds. It can be shown [3] that the function calculated this way lies between the Hashin bounds, i.e.,

$$\sigma_w^{I+} > \sigma_w^{EMA} > \sigma_w^{I-}$$

As indicated by the curves in figure 6, the differences between these predictions are small.

The second order moment of the orientation dependent stress component can be calculated applying the derivative of the stored elastic energy as well. Under some mild assumptions concerning the neglected elastic anisotropy and correlation between the different grains for polycrystalline single phase materials, an analytical expression for the density of the elastic stored energy  $u$  can be derived [9]. The second order stress moments follow immediately by derivatives with respect to the bulk modulus  $K_A$  and the shear modulus  $G_A$  of the isotropic polycrystal:

$$\langle \sigma_{ij}^a \sigma_{ij}^a \rangle = 3 \langle s^{a2} \rangle + \langle s_{ik}^a s_{ik}^a \rangle \quad (30)$$

with

$$\langle s^{a2} \rangle = 2K_A^2 \frac{\partial}{\partial K_A} u^a = \frac{2}{90} \frac{(12K_A G_A)^2}{(3K_A + 4G_A)^2} (\alpha_c - \alpha_a)^2 \Delta T^2 \quad (31)$$

$$\langle s_{ik}^a s_{ik}^a \rangle = 4G_A^2 \frac{\partial}{\partial G_A} u^a = \frac{8}{15} G_A^2 \frac{27K_A^2 + 48K_A G_A + 32G_A^2}{(3K_A + 4G_A)^2} (\alpha_c - \alpha_a)^2 \Delta T^2 \quad (32)$$

$$\sigma_{ik}^a = s^a \delta_{ik} + s_{ik}^a, \quad s_{kk}^a = 0 \quad (33)$$

$$\sigma_w^a = \frac{1}{3} (\langle \sigma_{ik}^a \sigma_{ik}^a \rangle - \frac{3}{2} \langle \sigma_c^a \rangle^2)^{1/2} \quad (34)$$

Thus, the first and second moments of the residual stress distribution are dependent only on the elastic constants of the constitutive phases, their volume fractions, their thermal expansion coefficients and the stress-free temperature ( $\Delta T$ ). In practice, the last is the parameter that is generally unknown.

### 3 Experimental Details and Results

#### 3.1 Materials

Nineteen composite samples with  $ZrO_2$  volume fraction  $v_Z$  ranging from 0.01 to 0.9 were measured. The samples were all sintered with the exceptions that the three with  $v_Z=0.025$ , 0.05

and 0.9 which were hot pressed in order to attain full density. All samples were subsequently air-annealed at 1650° for 10 hours after desification. The grain size of both the  $\text{Al}_2\text{O}_3$  phase and the  $\text{ZrO}_2$  phase were measured for all the samples and the results are plotted in figure 2.

### 3.2 Measurement

The techniques used in fluorescence measurement and analysis have been described in detail in [8]. Briefly, an unmodified optical microprobe<sup>1</sup> was used to both excite the fluorescence and to collect and analyze the resulting fluorescence spectrum using an attached spectrometer. The 514 nm line of an argon ion laser was used to excite the fluorescence. The fluorescence signals were collected from a region of about  $30\mu\text{m}$  diameter in size as defined by the laser beam so as to probe many grains simultaneously. The intensity of the  $R_1$  and  $R_2$  fluorescence lines were typically scanned by integrating over 0.5 second intervals at a spacing of 0.2 wavenumbers, with the intensities being recorded under computer control. The collected data was subsequently analyzed with curve fitting algorithms, included in the LabCalc software package<sup>2</sup>, to identify the position of the fluorescence peaks. All the measurements were made with the samples at room temperature. The peak shift due to temperature fluctuation was corrected using the temperature dependence coefficient of  $\sim 0.14 \text{ cm}^{-1}/^\circ\text{C}$  [11]. Local heating due to the incident laser beam was avoided by using a small laser power of  $\sim 0.5 \text{ mW}$  at the sample. The instrumental shift due to variations in room temperature was also corrected by simultaneously monitoring a characteristic Neon line at  $14564 \text{ cm}^{-1}$ , close to the  $R$  lines.

### 3.3 Analysis

Several spectra were taken at different spots on each sample. The resulting peak shift and broadening are plotted as a function of  $\text{ZrO}_2$  volume fraction  $v_Z$  in figures 3 and 4. Both the

---

<sup>1</sup>Instruments SA, Raman Microprobe Model T64000.

<sup>2</sup>Galactic Industries Corp.

shift and broadening were measured using a strain free sapphire as the zero shift and broadening standard.

From equation 1, the frequency shift of the R<sub>2</sub> line from a volume element with constant stress distribution within a Al<sub>2</sub>O<sub>3</sub> grain is

$$\Delta\nu = 2\Pi_a \sigma_a + \Pi_c \sigma_c \quad (35)$$

where  $\Pi_a$  and  $\Pi_c$  are the piezo-spectroscopy coefficients for the *a* and *c* directions. They have been measured recently at room temperature to have values of 2.75 and 2.10 cm<sup>-1</sup>GPa<sup>-1</sup>, respectively [12]. A positive shift implies tension and a negative one implies compression. Following the assumption of section 2, we can write the residual stress in Al<sub>2</sub>O<sub>3</sub> as the sum of the contribution from the thermal mismatch between the two phases and from the anisotropy of Al<sub>2</sub>O<sub>3</sub> itself. The fluorescence shift can similarly be decomposed:

$$\Delta\nu = \Delta\nu^a + \Delta\nu^i \quad (36)$$

and we assume that the stress due to thermal expansion anisotropy is independent of the volume fraction of ZrO<sub>2</sub>. Using the piezospectroscopic relationship in equation 35, we have

$$\langle \Delta\nu^a \rangle = \Pi_c \langle \sigma_c^a \rangle + 2\Pi_a \langle \sigma_a^a \rangle = -(\Pi_a - \Pi_c) \langle \sigma_c^a \rangle \quad (37)$$

Thus, the intercepts of figure 3,  $\langle \Delta\nu^a \rangle$ , gives directly the average stress along the *c*-direction due to the thermal expansion anisotropy above.

The shift due to the average stress caused by ZrO<sub>2</sub> inclusion  $\langle \sigma^i \rangle$  is

$$\langle \Delta\nu^i \rangle = (\Pi_c + 2\Pi_a) \langle \sigma^i \rangle \quad (38)$$

A least square fitting of the data upto  $v_Z = 0.8$  using a second order polynomial gives  $\langle \Delta\nu^a \rangle = -0.037 \text{ cm}^{-1}$  and  $\langle \Delta\nu^i \rangle = -6.0v_Z + 2.2v_Z^2 \text{ cm}^{-1}$ . The shift is independent of zirconia volume fraction from 0.8 to 0.9 and have an average value of  $-3.4 \text{ cm}^{-1}$ . Therefore, using equation 37, the anisotropic components of the average stress along the  $a$  and  $c$  directions of  $\text{Al}_2\text{O}_3$  grains are -28 and 56 MPa, respectively. The average isotropic stress component in the  $\text{Al}_2\text{O}_3$  phase as a function of  $v_Z$  is also derived from data in figure 3 using equation 38

$$\langle \sigma^i \rangle_A = -790v_Z + 290v_Z^2 \text{ MPa for } v_Z \leq 0.8 ; \quad \langle \sigma^i \rangle_A = -450 \text{ MPa for } v_Z > 0.8 \quad (39)$$

The average stress in the  $\text{ZrO}_2$ phase,  $\langle \sigma^i \rangle_Z$ , is obtained by using the force balance requirement (equation 12), thus

$$\langle \sigma^i \rangle_Z = 790v_A - 290v_Av_Z \text{ MPa} \quad (40)$$

The peak broadening is directly related to the width of stress distribution. To obtain an explicit relationship, we assume again that  $\sigma_a$  and  $\sigma_c$  are (a) independent of each other, (b) independent of  $\sigma^i$ , and (c) they all follow Gaussian distribution:

$$p(\sigma_a^a)p(\sigma_c^a)p(\sigma^i) = N \exp \left[ -\frac{(\sigma_a^a - \langle \sigma_a^a \rangle)^2}{2\sigma_w^a} \right] \exp \left[ -\frac{(\sigma_c^a - \langle \sigma_c^a \rangle)^2}{2\sigma_w^a} \right] \exp \left[ -\frac{(\sigma^i - \langle \sigma^i \rangle)^2}{2\sigma_w^i} \right] \quad (41)$$

where  $\sigma_w^a$  and  $\sigma_w^i$  are the breadths of the distribution in stresses  $\sigma_a^a$  (or  $\sigma_c^a$ ) and  $\sigma^i$  respectively. The peak broadening can then be shown [8] to consist of two parts

$$\sqrt{\langle \Delta\nu^2 \rangle} = \sqrt{\langle \Delta\nu^{a2} \rangle + \langle \Delta\nu^{i2} \rangle} \quad (42)$$

where

$$\sqrt{\langle \Delta\nu^{a2} \rangle} = \sqrt{4\Pi_a^2 + \Pi_c^2} \sigma_w^a \quad (43)$$

$$\sqrt{\langle \Delta\nu^{i2} \rangle} = (2\Pi_a + \Pi_c) \sigma_w^i \quad (44)$$

where  $\sqrt{\langle \Delta\nu^{a2} \rangle}$  is the broadening due to thermal anisotropy, which is independent of  $v_Z$ , and  $\sqrt{\langle \Delta\nu^{i2} \rangle}$  is due to the thermal mismatch of the two phases.

Fitting of the data (for sintered materials only) in figure 4 using parabolic dependence of  $\sigma_w^{i2}$  on  $v_Z$  gives  $\sqrt{\langle \Delta\nu^{a2} \rangle} = 0.89 \text{ cm}^{-1}$  and  $\langle \Delta\nu^{i2} \rangle = 5.09 v_Z - 5.16 v_Z^2 \text{ cm}^{-2}$ . Therefore, from equation 43, 44, the widths of the distributions are

$$\sigma_w^a = 153 \text{ MPa} ; \quad \sigma_w^i = \sqrt{669 v_Z - 679 v_Z^2} \text{ MPa} \quad (45)$$

## 4 Discussion

The data of figures 3 and 4 provides a basis for a detailed comparison between the experiment and the predictions of the stochastic stress analysis outlined in section 2 for both the average stress in the alumina phase and the width of the stress distribution as a function of the volume fraction of the zirconia phase.

The observed frequency shift of the fluorescence peak (figure 3), and the corresponding average stress (figure 5) calculated using equation 38, exhibit a number of interesting characteristic features as a function of volume fraction of zirconia. For volume fractions up to  $\sim 0.35$  the data is approximately linear, then its curvature becomes evident until  $v_Z \sim 0.8$  it becomes independent of volume fraction of zirconia. Although the values of the average stress can be fitted very accurately to a linear dependence on zirconia volume fraction upto  $\sim 0.35$ , they can equally well be fitted over the same range to equation 15, the prediction of the effective field approximation for the average stress in the alumina phase in terms of the effective modulus and the thermal expansion mismatch strain. This is shown in figure 5 by the lower dashed line corresponding to the upper Hashin bound on the effective modulus and for a temperature change  $\Delta T$  of  $-1210^\circ\text{C}$ . The excellent

correspondence between the data and the upper Hashin bound upto at least 35% zirconia is consistent with the microstructural observations of zirconia particles embedded in an alumina matrix. This is despite the fact that the percolation limit for randomly distributed zirconia particles is ~ 17% [13], suggesting that alumina may actually “wet” the zirconia phase. The departure of the data at the intermediate volume fractions from the prediction based on the upper Hashin bound indicates that the interconnecting networks of grains start to dominate the microstructure, and the effective modulus increases with increasing  $ZrO_2$  volume fraction. At high volume fractions, zirconia becomes the matrix and alumina grains become inclusions. It is therefore expected that the average stress dependence should follow the lower Hashin bound. To better describe the stress dependence over the entire volume fractions, the effective medium approximation (EMA) is also included since it takes into account all possible topologies, providing intermediate values between the two Hashin bounds in the intermediate volume fractions, but approaching the two bounds at the extreme volume fractions. This function, calculated numerically, is plotted in figure 5, and provides a close fit to the experimental data, except at the highest volume fractions where the stress becomes independent of volume fraction instead. This plateau region cannot readily be explained in terms of elasticity. One possible explanation is that at the high volume fractions of zirconia the stress-free temperature is significantly lower than that for the alumina-rich composites. An approximately linear dependence on volume fraction would nevertheless be expected. The other possible explanation is that the residual stress exceeds that for plastic yielding in the zirconia surrounding the individual alumina grains. From figure 5, the average stress in the alumina grains in this plateau region is ~ 450 MPa, which would correspond to a resolved shear stress for plastic flow of ~ 640 MPa in the zirconia phase. It is difficult to know whether this is reasonable, since the complete information on the yield strength of cubic zirconia in the entire cooling temperature range is not available. This is consistent, however, with the measurements of Cheong *et al.* [14] of the yield stress in cubic zirconia single crystals at temperatures above 1200°C. They found the

yield stress of cubic zirconia drops significantly as the temperature increases due to activation of secondary slip systems.

The value of the temperature change used to fit the average stress in figure 5 is of some interest. First, since the materials were sintered at 1650°C, the calculated temperature change over which thermal stresses developed indicates that diffusional relaxation accommodated any stresses for the first 400 degrees of cooling. This is consistent with the observation that zirconia is an effective densification aid for alumina, lowering the temperatures necessary for densification. Secondly, using this temperature change the anisotropic stress components in  $\text{Al}_2\text{O}_3$  are evaluated using equations 18 and 19 to be 88 and -44 MPa along the  $c$  and  $a$  axis, respectively. These values are comparable to those directly obtained from the intercept in figure 3 (section 3.3).

The thermal strain  $\Delta\alpha\Delta T$  calculated from the linear portion of the data in figure 5 provides, in principle, the information necessary to evaluate the predicted values of the second moment of the stress distributions (equations 26-29). Comparison of these stress fluctuations with the measured broadening data involves the addition of terms quadratically using equation 42. To do this, the data in figure 4 is replotted in figure 6 together with the upper and lower Hashin bounds on the broadening calculated using equations 28 and 29, and 43 and 44. The lower Hashin bound on the broadening is independent of the zirconia volume fraction because, as mentioned in section 2.2. this would correspond to isolated alumina grains embedded in  $\text{ZrO}_2$  matrix in which case the stress resulting from the phase mismatch would be purely hydrostatic. The fluctuations are then the same as in a polycrystalline alumina matrix. The upper Hashin bound on the broadening, whilst also bounding the data, evidently does not fit the data well. Much closer to the data are the bounds on the broadening calculated by imposing the additional restriction of the maximum entropy principle (equations 28, 29). This is particularly so if the data from the hot-pressed materials (the open data points) is ignored. (The hot-pressed materials have exceptional grain sizes compared to the sintered materials.) Although the fit between the data from the sintered

materials and the bounds is good, more detailed comparisons are not possible at the present time. This is primarily because the observed variation in peak broadening from place to place within the materials, especially at the lower and higher volume fractions of zirconia, is larger than the difference between the bounds. The experimental variation is real and is believed to be due to the difficulty in sampling a sufficiently large region that is statistically homogeneous at the extreme volume fractions.

The above comparison can also be carried out in terms of the stress fluctuation caused by the phase mismatch component,  $\sigma_w^i$ , alone. Plotted in figure 7 are the bounds on the second moment of the stress distribution calculated using the thermal strain derived from the first moment of the stress distribution. The upper and lower Hashin bounds, and their modifications obtained by applying the restriction of maximum entropy are indicated. Also shown is the curve corresponding to the least square fit to the experimental broadening data from figure 4 (equation 45), which has values close to but smaller than both of the bounds from the information theory. This is not entirely surprising because the difference between the two bounds are extremely small, hence any systematic error in the experimental data and of the theory introduced by simplifications of model can easily cause discrepancies large compared to the spacing between the two maximum entropy bounds.

Having analyzed the experimental data it is now possible to offer an assessment of the validity of the stochastic stress analysis. The agreement between the average stress determined from the fluorescence frequency shift and that calculated using the stochastic analysis based on the upper Hashin bound is, up to about 35% zirconia, excellent. However, this by itself is not a particularly stringent test of the analysis since the same prediction can be made by a variety of other approaches. For instance, according to Eshelby's calculations [15] the interaction energy between centers of dilatation is dependent only on their volume fraction and the effective elastic modulus. On the other hand, by using the thermal strain obtained from the upper Hashin bound

fitting at relatively low volume fractions, the effective medium approximation produces a close fit to the data through out the entire volume fraction. This suggest that the stochastic analysis can predict the first moment of the stress distribution accurately, provided that a realistic model for the microstructural topology is used. A more exacting test of the stochastic analysis is the second moment of the stress distribution. The experimental data, although showing greater variability from place to place in the material than for the first moment, is consistent with the predictions of the stochastic analysis that they closely fit the maximum entropy limit of the Hashin bounds. With the exception of the hot-pressed composites, the majority of the data exhibits the characteristic convex dependence on volume fraction. Since the only data used in predicting the second moment of the stress distribution are the single crystal elastic constants, the zirconia volume fraction, and the thermal strain obtained from the data for the average stress, the agreement represents a further validation for the stochastic analysis.

## 5 Concluding Remarks

The thrust of the majority of studies of the elastic behavior of composite materials has hitherto been in the determination of the elastic moduli, or equivalently, the thermal conductivity, as a function of volume fraction. From such investigations, bounds on the elastic moduli have been established and compared with experiment. By contrast, in this work we have determined the residual stress distribution in a series of two-phase  $\text{Al}_2\text{O}_3$ - $\text{ZrO}_2$  composites, rather than the moduli, and compared it with the predictions of a stochastic stress analysis. This has proven possible by using the technique of optical fluorescence spectroscopy, which provides a measure of both the first and second moments of the stress distribution from the frequency shift and broadening of the characteristic R-line fluorescence from  $\text{Cr}^{3+}$  dopants in aluminum oxide. The predictions of the stochastic stress analysis, outlined in section 2, are in good agreement with the measurements.

made by fluorescence spectroscopy indicating that confidence can be placed on the predictions. These are expressed in terms of the single crystal elastic and thermal expansion constants, the second phase volume fraction and the thermal strain. The last is obtainable from the volume fraction dependence of the average stress, determined from the shift in the fluorescence frequency as a function of volume fraction. More stringent tests of the stochastic analysis than that presented here can be envisaged but they will require both a better method of experimentally averaging over large volumes of material in order to establish statistically significant data as well as methods of making random composites in which scale-dependent stress relaxation processes do not occur. In the absence of such developments, the experimental measurements of the first and second moments of the residual stress distributions compare exceptionally favorably with the predictions of the stochastic stress analysis.

## ACKNOWLEDGMENT

This work was supported by the Office of Naval Research under grant N00014-91-J-1875 (QM) and the DARPA URI program at UCSB under contract N00014-92-J-1808 (DRC). The authors would like to thank Dr. W. Kreher for valuable discussions and supporting calculations.

## References

1. I.C. Noyan and J.B. Cohen, "Residual Stress - Measurement by Diffraction," Springer-Verlag, New York, 1987.
2. Z.J. Hashin., Appl.Mech. 29, 143 (1962).
3. W. Kreher and W. Pompe, "Internal Stresses in Heterogeneous solids," Akademie-Verlag, Berlin, 1989.
4. T. Mura, "Micromechanics of Defects in Solids", Martinus Nijhoff, Boston (1982).
5. M. Ortiz and A. Molinari, J. Mech. Phys. Solids, 36, 385 (1988).
6. J.D. Eshelby, Proceedings of the Royal Society, A241, 376 (1957).
7. Y. Fu and A.G. Evans, Acta metall. et Mater., 33, 1515 (1985).
8. Q. Ma and D.R. Clarke, J. Am. Ceram. Soc., 76, 1433 (1993).
9. W. Kreher and A. Molinari, Proceedings of the Third International Conference on Residual Stresses, Elsevier Science Publishing, Barking, 1992.
10. J.B. Wachtman, Jr., W.E. Teft, D.G. Lam, Jr., and R.P. Stinchfield, J. Research National Bureau Standards, 64A, 213 (1960).
11. Q. Ma and D.R. Clarke, Experiments in Smart Materials and Structures, ASME Winter Annual Meeting Symposium Proceedings, New Orleans, 1993.
12. J. He and D.R. Clarke, in preparation, 1993.
13. R. Zallen, "The Physics of Amorphous Solids," Wiley, New York, 1983.
14. D.S. Cheong, A. Dominguez-Rodrguez and A.H. Heuer, Phil. Mag., 63, 377 (1991).
15. J.D. Eshelby, Acta Metall. et Mater., 14, 1306 (1966).

## Figure Captions

1. Scanning electron micrograph of three of the alumina-zirconia materials studied to illustrate the distribution of the two phases. The top is 10% zirconia, the middle is 50% and the bottom 85%. The zirconia phase appears as the brighter of the two phases due to its higher atomic number.
2. The average grain size of the  $\text{Al}_2\text{O}_3$  and  $\text{ZrO}_2$  phases as a function of zirconia volume fraction.
3. Observed shift in  $R_2$  fluorescence frequency as a function of the volume fraction of the cubic zirconia phase. The full data points are from the sintered materials whereas the open data points are from the hot-pressed materials. The line through the data corresponds to a least squares fit to the fluorescence data (section 3.3).
4. Observed broadening of the  $R_2$  fluorescence peak as a function of the volume fraction of zirconia phase.
5. The data for the average stress from figure 3 compared with the predictions of the upper and lower Hashin bounds, and the EMA on the first moment of the stress distribution. The upper Hashin bound is given by equation 15 with the modulus function  $K$  of equation 16 and an effective freezing temperature of  $-1210^\circ\text{C}$ . The data for the entire volume fraction range is plotted in the top, the lower volume fraction part, from which the thermal strain was obtained, is replotted in the bottom for more detailed comparison.
6. Comparison of the observed fluorescence peak broadening and the predictions of the broadening based on bounds derived from the stochastic stress analysis. The broadening is related to the stress distributions using the piezo-spectroscopic equations 42-44.  $H+$  and  $H-$  are the upper and lower Hashin bounds.  $I+$  and  $I-$  are the upper and lower bounds obtained by

**applying the principle of maximum entropy.**

**7. Bounds on the second moment of the stress distribution calculated using the thermal strain derived from fitting the first moment of the stress distribution in figure 5. Also shown as the solid curve is the second moment derived from the least squares fit to the experimental data for the observed broadening of the fluorescence peak (equation 45).**

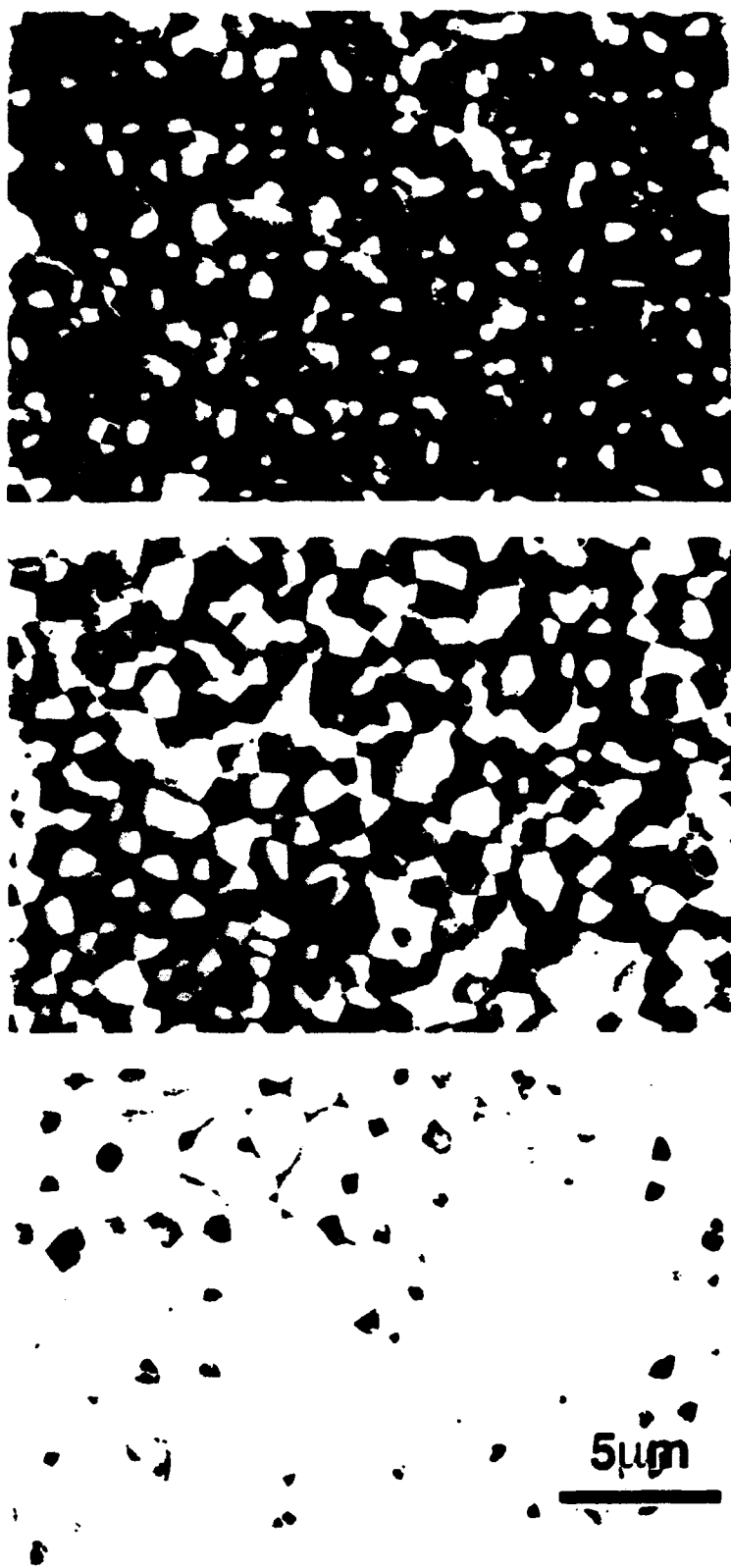


Fig. 1

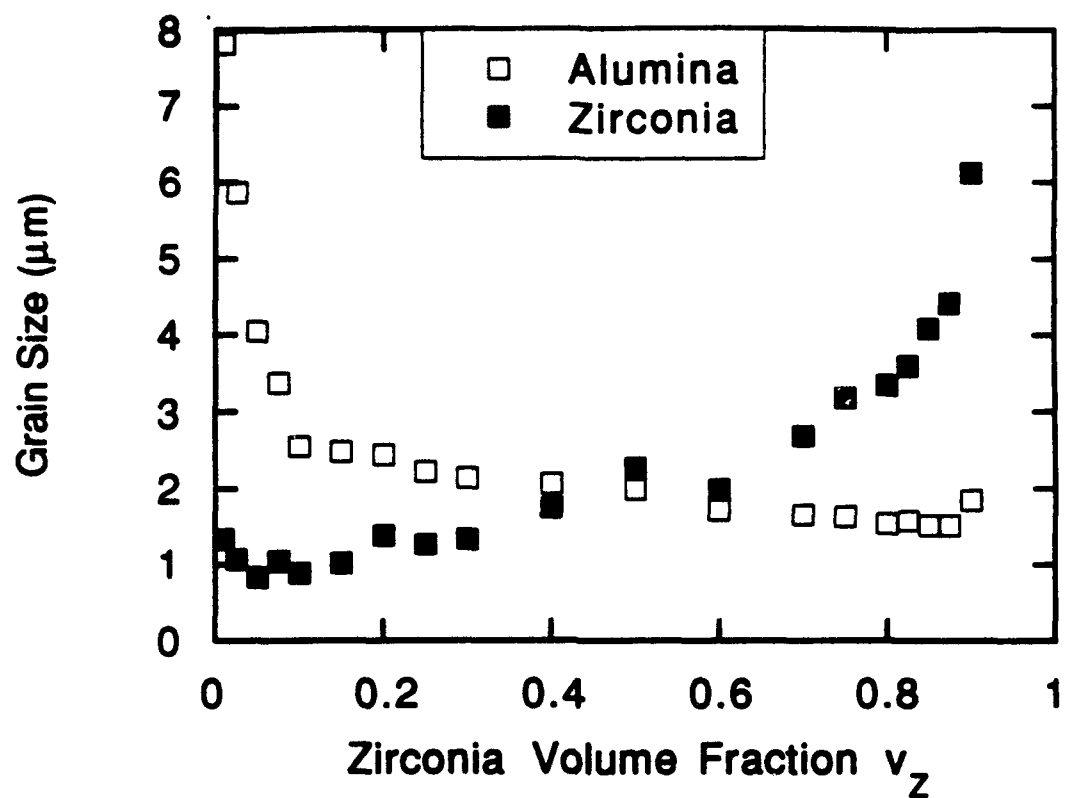


Fig. 2

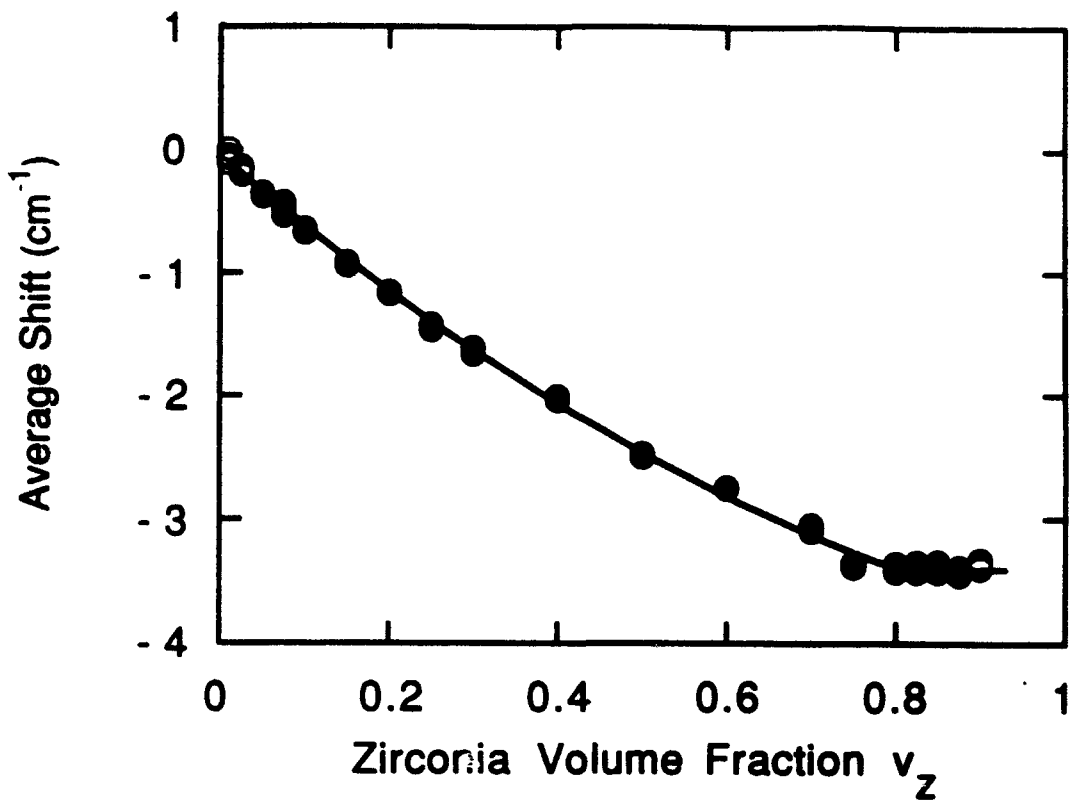


Fig. 3

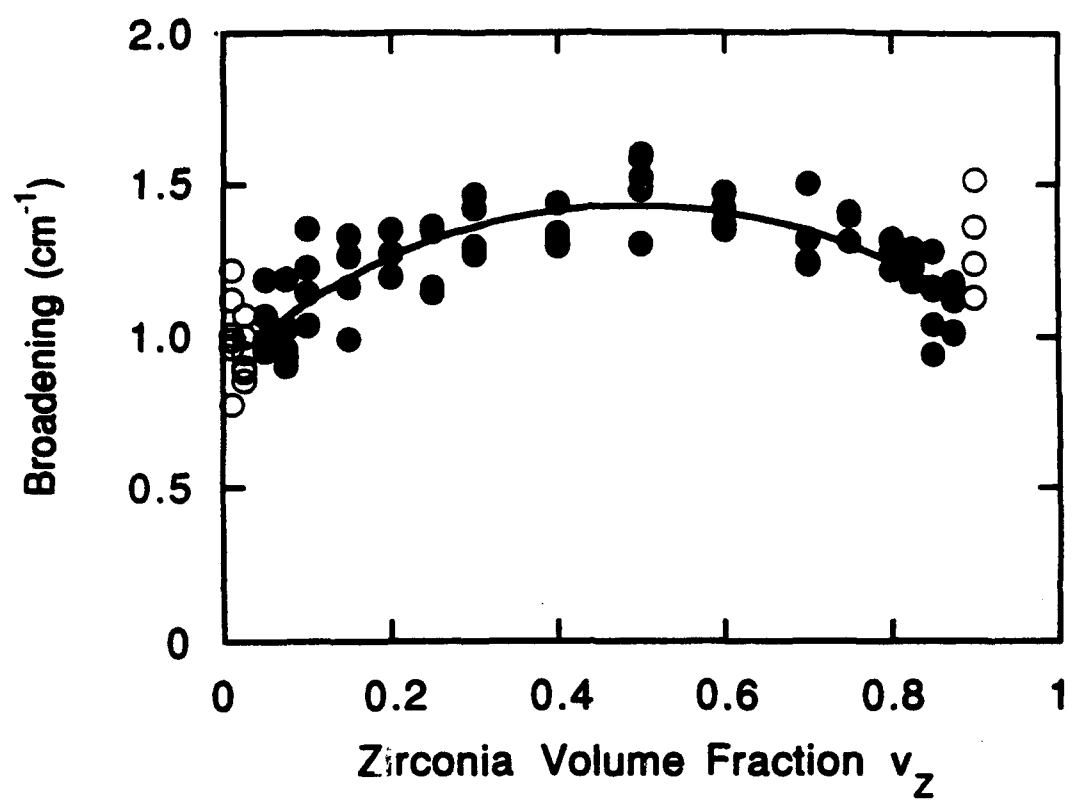


Fig. 4

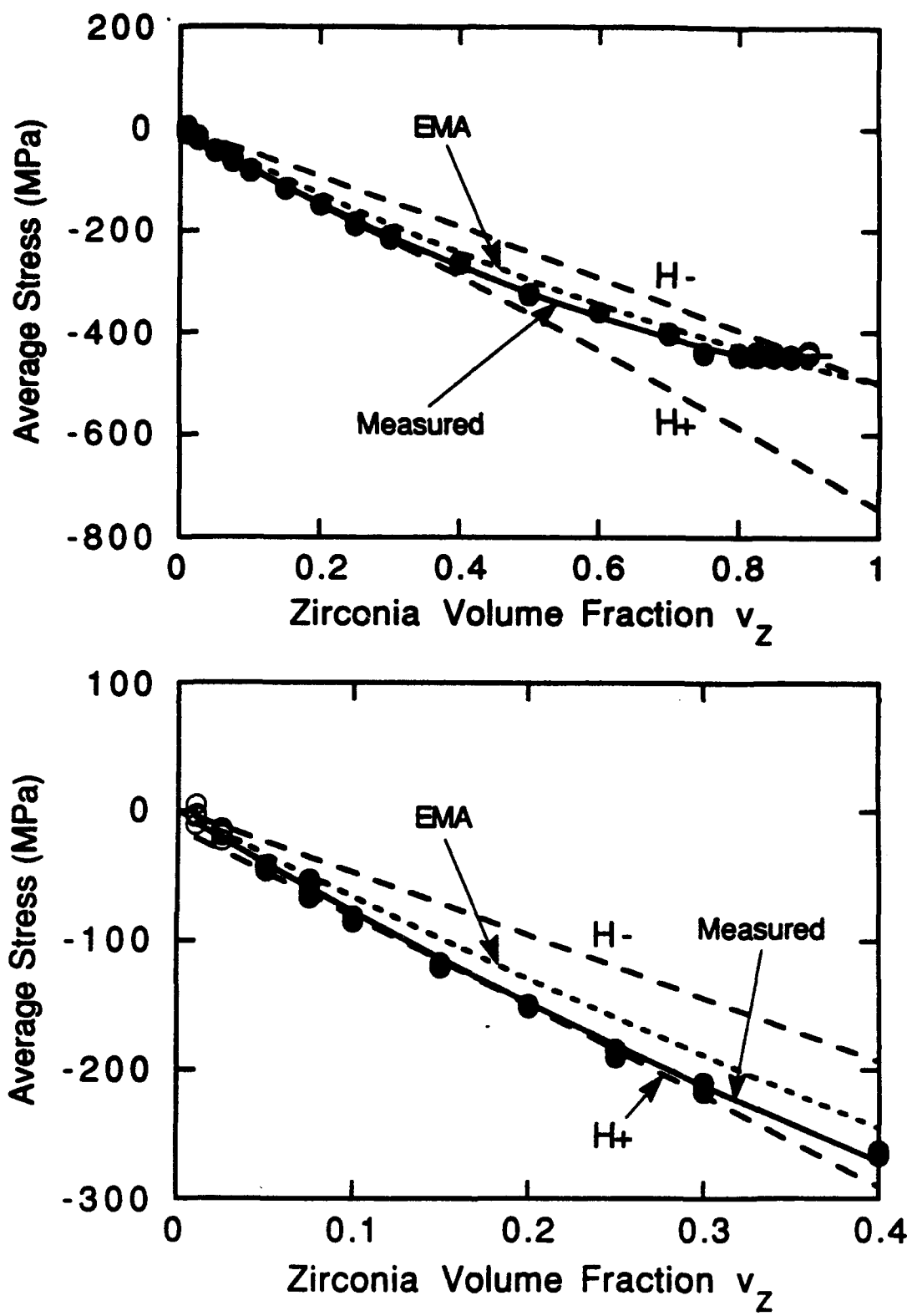


Fig. 5

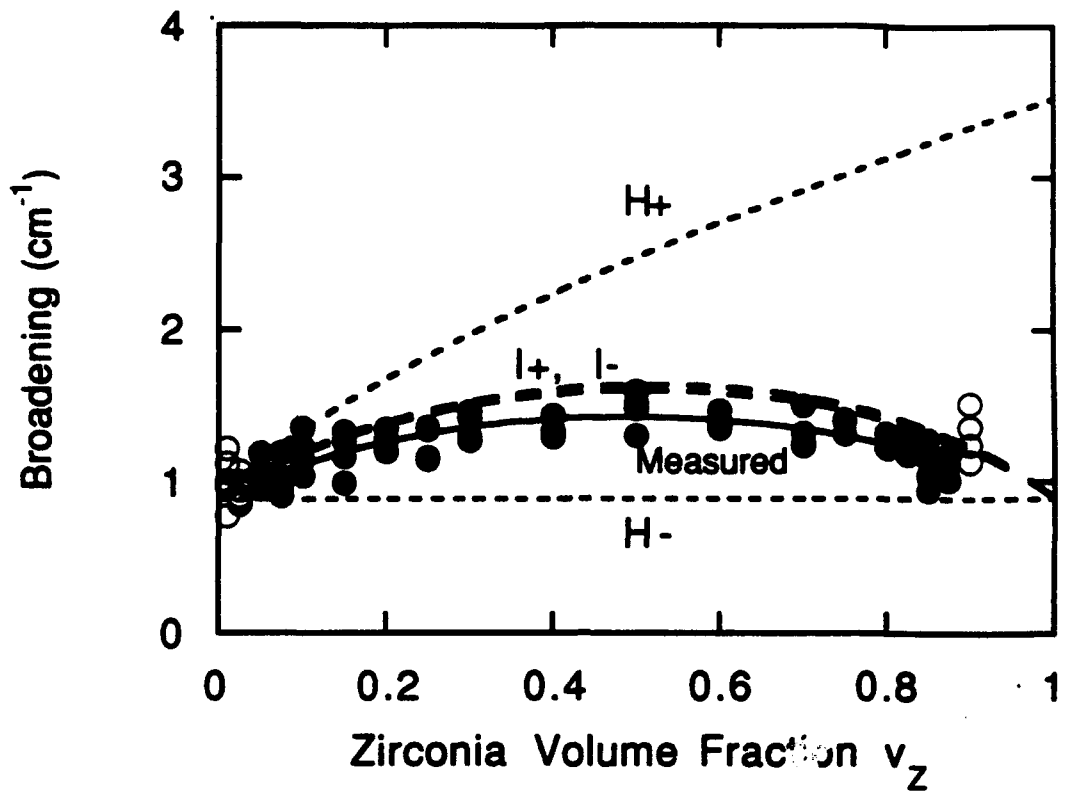


Fig. 6

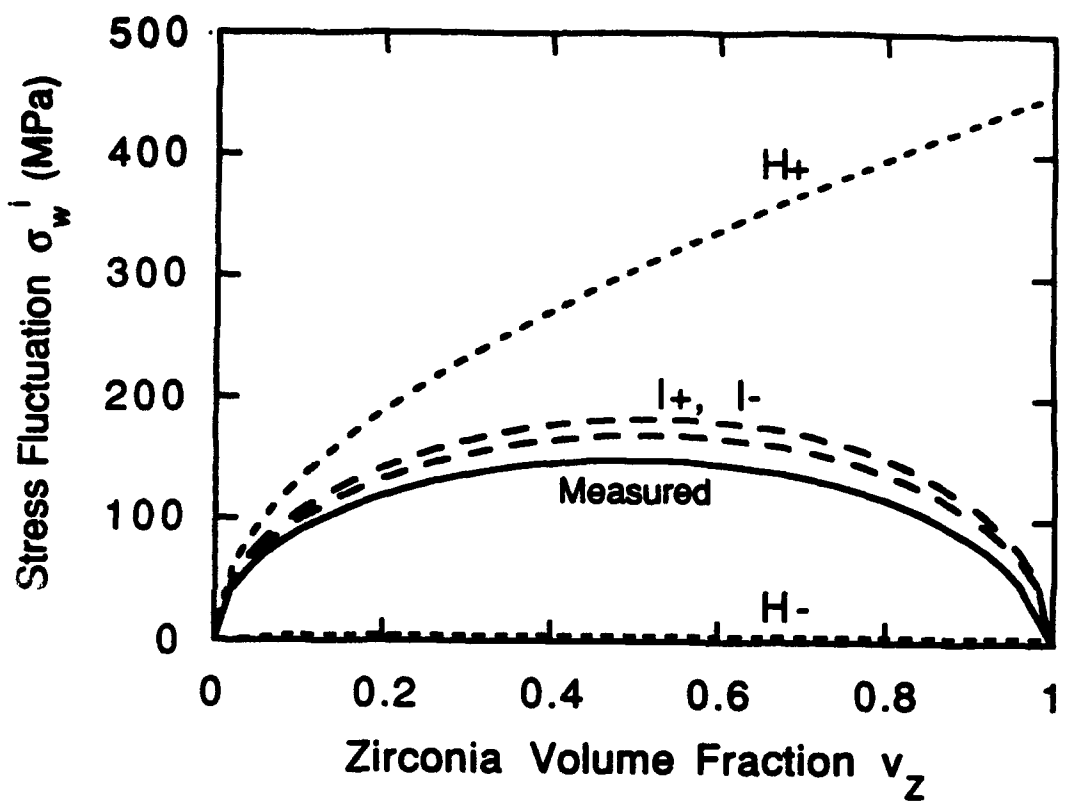


Fig. 7



## STRESS MEASUREMENT USING OPTICAL FLUORESCENCE

Qing Ma and David R. Clarke

Department of Materials  
University of California  
Santa Barbara, California

### Abstract

*A general methodology for determining stresses in materials and structures is developed based on the piezo-spectroscopic properties of crystals. General relationships between the measured fluorescence line shifts and the stress state are presented. An experiment measuring the residual stresses in an embedded sapphire fiber is used to illustrate some of the advantages of the optical method and its use for probing microscopic features. The experiment also shows that stress tensor can be determined despite the fact that the fluorescence shift is a scalar quantity.*

### 1 Introduction

As technology enables the development of more advanced, and often more complicated materials and structures, it also demands new stress measurement techniques. Very often, it is also required to measure the stress state with high spatial resolution. For example, it is desirable to know the localized stresses associated with the domain structure and their variations due to domain switching in ferroelectric materials, because these stresses can affect the device reliability by inducing crack formation and growth under electrical/mechanical loads. Conventional stress measurement techniques based on diffraction methods, such as X-ray and neutron diffraction, although accurate, are incapable of such selective measurements, which usually requires both an imaging capability and high spatial resolution.

The development of the optical fluorescence method was partially motivated by such demands. Many materials, especially ceramics, are known to possess fluorescence if containing appropriate dopant ions. The characteristic fluorescence lines shift systematically with stresses (piezo-spectroscopic effect), and therefore can be employed for stress measurement. In fact, the frequency shifts of the fluorescence lines of ruby, generated by the Cr<sup>3+</sup> impurities, have been used to monitor the pressure in diamond cells since the early 1970s (Forman, 1972).

Recently, we have significantly extended this technique and applied it for studying the mechanical properties of ceramics and composites (Ma and Clarke, 1993a, b, Ma et al., 1993a, b).

By using an optical microscope to inspect the sample, and to focus a laser beam on a small region of interest to excite the fluorescence signals, selective measurement of stresses can be easily achieved with spatial resolution determined essentially by the diffraction limit of the laser beam. In this paper, we will first review the basic aspects of the fluorescence method and then illustrate its utility with an experiment in which the residual stress in a sapphire fiber embedded in a cubic zirconia matrix was measured.

## 2 Fluorescence Method

### 2.1 General Formulations

Fluorescence lines of materials are usually generated from the electronic transitions of impurity ions. When a stress is applied to a material, the resulting strain changes the crystal field around a impurity ion and therefore shifts the electronic levels of the ion. A fluorescence line shifts if the corresponding initial and final electronic levels of the radiative transition shift with different amount of energies. The relationship between the applied stress and the resulting frequency shift depends on the detailed electronic structure of the ion in the particular lattice, and therefore is complicated. However, for the purpose of stress measurement, it is sufficient to establish phenomenological relationships and calibrate them experimentally.

Consider a crystal subject to a homogeneous stress  $\sigma_{ij}^*$  (in crystallographic frame of reference), the frequency shift of a fluorescence line of a impurity ion,  $\Delta\nu$ , as a function of the applied stress, can be expanded:

$$\Delta\nu = \Pi_{ij}\sigma_{ij}^* + \Lambda_{ijkl}\sigma_{ij}^*\sigma_{kl}^* + \dots \quad (1)$$

Since the second and higher order terms are usually much smaller than the linear terms for most applications when the stress levels are not unusually high, they are often neglected from the analysis, therefore,

$$\Delta\nu = \Pi_{ij}\sigma_{ij}^* \quad (2)$$

Here  $\Pi_{ij}$  are the piezo-spectroscopic coefficients relating shift to the stress  $\sigma_{ij}^*$  in the crystallographic frame of reference. As previously pointed out by Grabner (1978),  $\Pi_{ij}$  form a second rank tensor because the above relationship must be covariant, and due to the symmetry of the stress tensor,  $\sigma_{ij} = \sigma_{ji}$ , the  $\Pi$  tensor is also symmetric. A major limitation of piezo-spectroscopy is evident from this equation. Unless the fluorescing species emits at several different frequencies, so that a set of simultaneous equations (one for each transition) can be generated, there may be an insufficient number of equations to solve for each of the maximum of six independent stress components needed to completely describe the stress state. Further, the site symmetry of the fluorescing ion, which governs the symmetry properties of the  $\Pi$  tensor, may also preclude the determination of all the independent stress components.

With the exceptions that the site point symmetry group belongs to either monoclinic or triclinic systems, the  $\Pi$  matrix is diagonal in the orthogonal crystallographic frame of reference (Nye, 1967). Consequently, the frequency shift is insensitive to pure shear stress as far as the linear terms are concerned. Further, if the site symmetry belongs to one of the uniaxial systems (tetragonal, hexagonal or trigonal), we have  $\Pi_{11} = \Pi_{22}$  (axes 1 and 2 are perpendicular to the principle symmetry axis), as in the case of  $\text{Cr}^{3+}$  in sapphire, only the summation  $\sigma_{11}^* + \sigma_{22}^*$  can be determined, not  $\sigma_{11}^*$  and  $\sigma_{22}^*$  individually, even with multiple fluorescence lines available. If the symmetry is cubic, such as for substitutional ions in  $\text{MgO}$ , the  $\Pi$  matrix reduces further,  $\Pi_{11} = \Pi_{22} = \Pi_{33}$ , hence only the trace of the stress tensor can be obtained.

While the piezo-spectroscopic coefficients,  $\Pi_{ij}$ , are usually calibrated in the crystallographic coordinates, it is sometimes more convenient to represent the stress in other coordinates (e.g., sample coordinates). The stress on the crystal structure will then be given by the applied stress components resolved onto the crystallographic axes, i.e., through an orthogonal coordinate transformation:

$$\sigma_{ij}^* = a_{ik}a_{jl}\sigma_{kl} \quad (3)$$

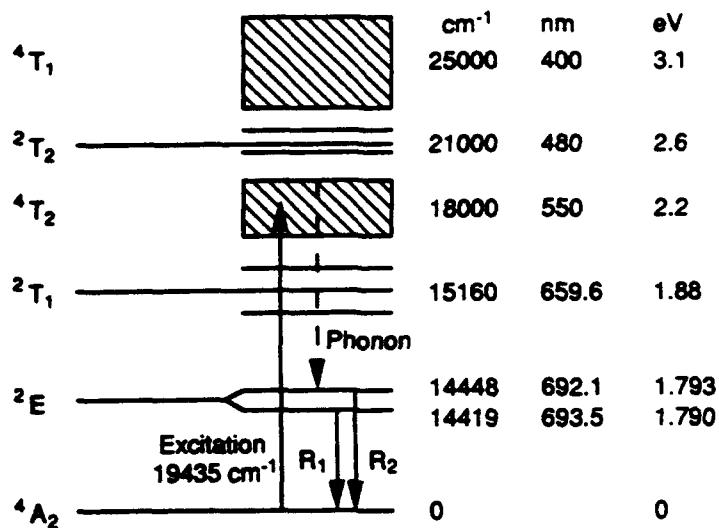


Figure 1: Lower electronic energy levels of a  $\text{Cr}^{3+}$  ion in sapphire (Nelson and Sturge, 1965), designated by their representations in the  $O_8$  group.

where  $a_{ij}$  is the transformation matrix relating the frame of reference in which the applied stresses are defined with respect to the crystallographic axes of the lattice. Thus, the frequency shift of a fluorescence line in a fluorescing crystal oriented at an arbitrary angle to a superimposed stress is given by the following tensorial relation:

$$\Delta\nu = \Pi_{ij} a_{ik} a_{jl} \sigma_{kl} \quad (4)$$

For certain site symmetries described above, the  $\Pi$  matrix is diagonalized, and the above equation can then be expressed explicitly:

$$\begin{aligned}
 \Delta\nu = & \Pi_{11}(\sigma_{11} + \sigma_{22} + \sigma_{33}) \\
 & + (\Pi_{22} - \Pi_{11})(a_{21}^2 \sigma_{11} + a_{22}^2 \sigma_{22} + a_{23}^2 \sigma_{33}) \\
 & + (\Pi_{33} - \Pi_{11})(a_{31}^2 \sigma_{11} + a_{32}^2 \sigma_{22} + a_{33}^2 \sigma_{33}) \\
 & + 2(\Pi_{22} - \Pi_{11})(a_{21}a_{22} \sigma_{12} + a_{21}a_{23} \sigma_{13} + a_{22}a_{23} \sigma_{23}) \\
 & + 2(\Pi_{33} - \Pi_{11})(a_{31}a_{32} \sigma_{12} + a_{32}a_{33} \sigma_{23} + a_{31}a_{33} \sigma_{31})
 \end{aligned} \quad (5)$$

## 2.2 Fluorescence of Chromium Ions in Sapphire

Chromium in sapphire is a well known chromophore, giving rise to the characteristic red fluorescence of ruby. The fluorescence originates from electronic transitions in the chromium ion produced by appropriate excitation as illustrated in figure 1. Electrons excited from their ground state,  $^4\text{A}_2$ , can jump to the  $^2\text{E}$  level by emitting phonon. The chromium ion can substitute for any of the aluminum ions in the corundum crystal structure of sapphire with the result that they are octahedrally coordinated to neighboring oxygen and aluminum ions. The octahedron is not regular, but elongated along the  $c$ -axis of the lattice, resulting in splitting of the  $^2\text{E}$  energy levels by 0.004 eV, in turn giving rise to the two distinct radiative transition lines in ruby,  $R_1$  and  $R_2$  at 1.790 and 1.794 eV respectively. Since the  $\text{Cr}^{3+}$  ion site has 3-fold rotational axis about the  $c$ -axis,  $\Pi_{11} = \Pi_{22} \neq \Pi_{33}$ . For simplicity, we will use the notations  $\Pi_{11} = \Pi_{22} = \Pi_e$  and  $\Pi_{33} = \Pi_c$  for both the  $R_1$  and  $R_2$  lines. The piezo-spectroscopic coefficients  $\Pi_e$  and  $\Pi_c$  were

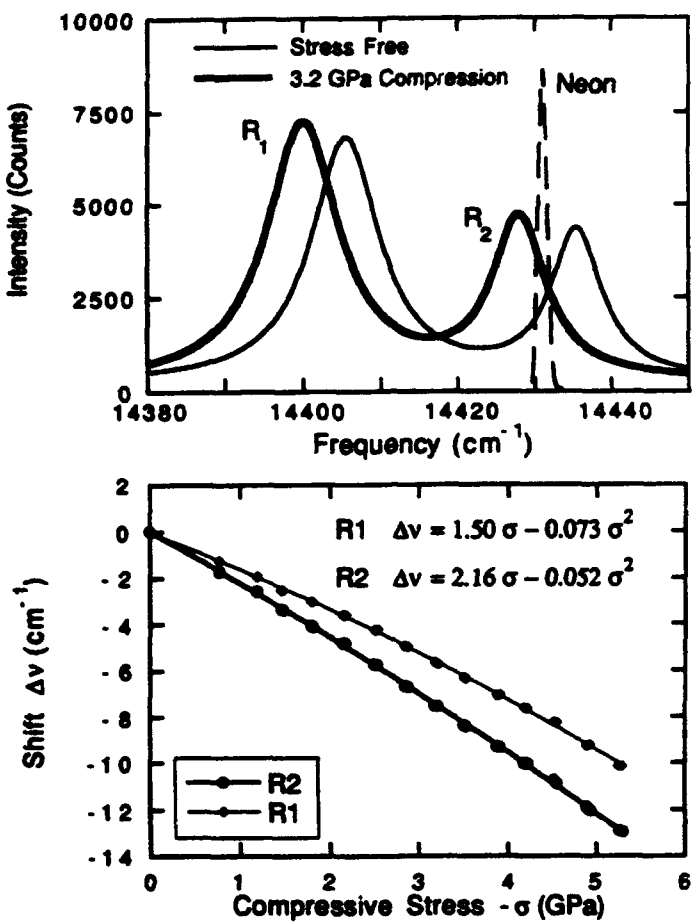


Figure 2: Frequency shifts of the  $R_1$  and  $R_2$  lines under uniaxial compression along  $c$ -axis of a sapphire sample. The Neon line is used for calibration. (a) Comparison of the peaks at 3.2 GPa and at stress free state; (b) The frequency shifts as a function of stress.

previously measured (Feher and Sturge, 1968, Kaplyanskii and Przhevuskii, 1962) for  $R_1$  to be  $3.2$  and  $1.4 \text{ cm}^{-1}\text{GPa}^{-1}$ , and for  $R_2$  to be  $2.7$  and  $2.15 \text{ cm}^{-1}\text{GPa}^{-1}$ , respectively<sup>1</sup>. A positive shift implies tension and a negative shift implies compression. For illustration, the shifts of the  $R_1$  and  $R_2$  peaks when a single crystal sapphire was compressed along its  $c$ -axis are shown in figure 2. The sharp neon line is used for frequency calibration.

### 2.3 Procedures for Optical Fluorescence Measurement

We use an unmodified optical microprobe<sup>2</sup> to both excite the fluorescence and to collect and analyze the resulting spectrum using an attached spectrometer. The optics of the microprobe is illustrated in figure 3. An argon ion laser with a number of possible line frequencies is used to excite the fluorescence. To start a measurement, a region of interest on the sample is first

<sup>1</sup>A recent measurement (Ho and Clarke, 1983) essentially verified these values, but also revealed small differences when stress was applied in two perpendicular directions in the basal plane indicating that the 3-fold symmetry may be broken. However, for the sake of simplicity, these refinements are not included here.

<sup>2</sup>Instruments SA, Optical Microprobe Model T64000.

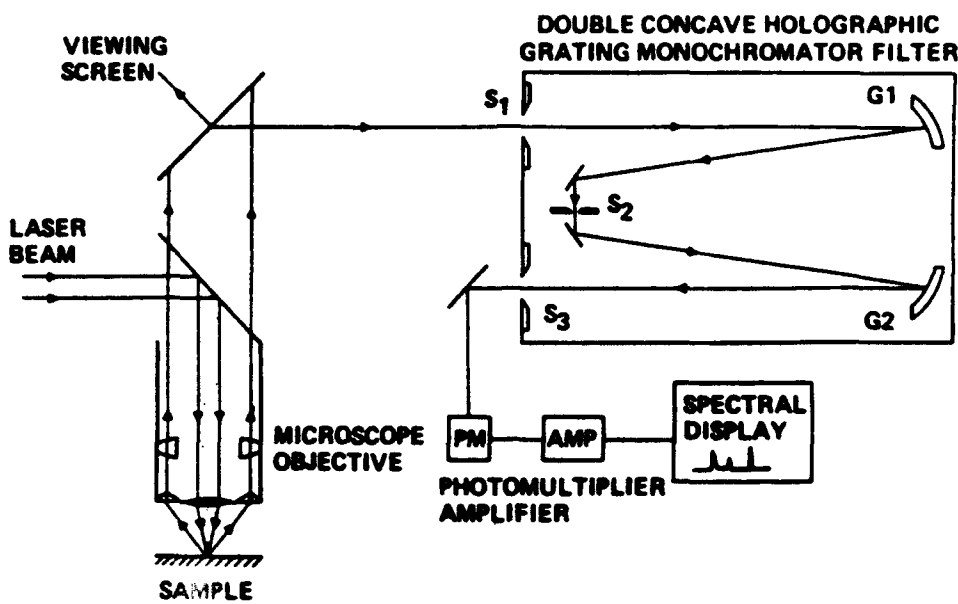


Figure 3: Schematic diagram of the optical microprobe.

selected with the attached optical microscope, then the laser beam is focused to a spot on the selected feature and the fluorescence produced is collected and analyzed. The intensity of the fluorescence lines are typically scanned by integrating over 0.5 second intervals at a spacing of 0.2-0.4 wavenumbers, with the intensities being recorded under computer control. The collected data are subsequently analyzed with curve fitting algorithms, included in the LabCalc software package<sup>3</sup>, to identify the position of the fluorescence peak. By using objective lenses of 50 $\times$  and 100 $\times$  magnifying powers minimum spot sizes of  $\sim 5\mu\text{m}$  and  $\sim 1 - 2\mu\text{m}$  can be produced. Larger probe sizes can be formed by using lower magnification lens or by partial defocusing. Also, by appropriate choice of the collection aperture size, the attainable axial resolution could be varied by the collection optics from  $\sim 10\mu\text{m}$  to  $\sim 200\mu\text{m}$ .

It is known that fluorescence lines shift systematically with the change of temperature (Wunder and Schoen, 1981). For the R<sub>1</sub> and R<sub>2</sub> lines of ruby, their frequencies shift to smaller wavenumbers with increasing temperature as shown in figure 4<sup>4</sup>. The linear fitting coefficients are  $-0.138$  and  $-0.132 \text{ cm}^{-1}/^\circ\text{C}$  for the R<sub>1</sub> and R<sub>2</sub> lines, respectively. Therefore, local heating due to the laser excitation beam has to be avoided. This is achieved by using low laser intensity such that no line shift can be measured when the spot size is systematically decreased (thereby increasing the power density incident on the sample), indicating that no significant heating of the probed volume occurred. Variations were, however, noted with variations in room temperature and so corrections were made to the peak shifts. This involved corrections for the change in room temperature using the above temperature dependence of line frequency and changes of the spectrometer dimensions as a result of thermal expansion. The latter can be corrected by simultaneously monitoring a characteristic neon calibration line close to the fluorescence lines of interest, as illustrated in figure 2.

<sup>3</sup>Geltec Industries Corp.

<sup>4</sup>Data obtained in collaboration with J. He, UCSB.

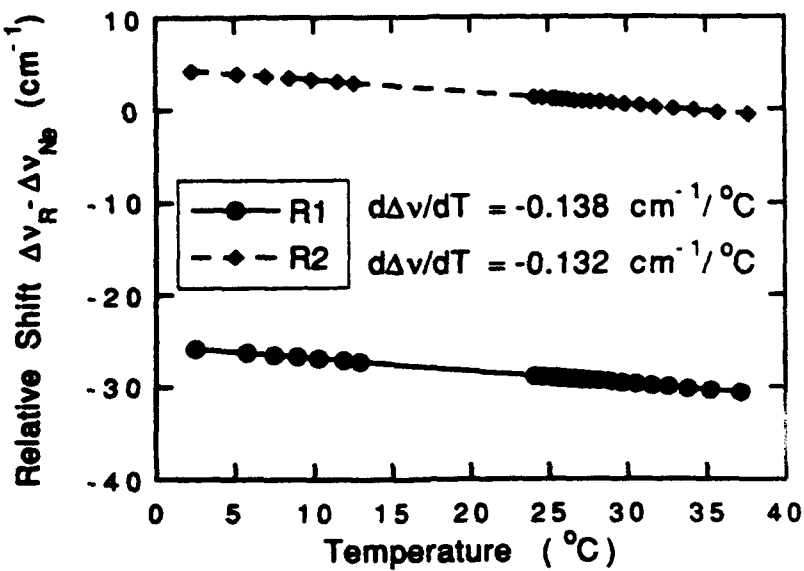


Figure 4: Frequency shifts of  $R_1$  and  $R_2$  lines as a function of temperature.

### 3 Determination of Residual Stresses in a Embedded Sapphire Fiber

To illustrate the application of the fluorescence method we have measured the residual stresses in Saphikon sapphire fibers embedded in a cubic zirconia matrix. The fibers have sufficient levels of chromium impurity to produce sufficiently intense fluorescence lines  $R_1$  and  $R_2$  of ruby when excited by an argon ion laser. For the problems of a  $c$ -axis fiber embedded perpendicular to the composite surface, the axisymmetric stress field in the fiber is diagonalized with the radial stress equal to the tangential stress. Therefore, the two independent stress components, the radial stress  $\sigma_r$  and the axial stress  $\sigma_z$ , can be determined by solving the following two simultaneous equations from the  $R_1$  and  $R_2$  lines:

$$\Delta\nu_1 = 2\Pi_{e1}\sigma_r + \Pi_{e1}\sigma_z \quad (6)$$

$$\Delta\nu_2 = 2\Pi_{e2}\sigma_r + \Pi_{e2}\sigma_z \quad (7)$$

where the subscripts 1 and 2 denote  $R_1$  and  $R_2$  lines, respectively.

#### 3.1 The Through-Focus Depth Profiling Method

The method of measuring subsurface stresses in a transparent fiber was developed in a earlier work (Ma and Clarke, 1993b) and is described briefly in the following. As illustrated in figure 5, the fluorescence from depth  $z$  below the top surface is collected by focusing a laser beam through the fiber top surface. By focusing to successively greater depths and measuring the frequency shift, a profile along the length of the fiber is obtained. Because of the small depth of field of the lens, the fluorescence excited will be collected from only a small volume on either side of the focal plane. The measured frequency shift  $\Delta\nu(z)$  is hence a weighted average of that within the effective excitation volume. Therefore, the actual depth profile of the frequency shift has to be deconvoluted from that measured by using the depth of field function of the microprobe. As described previously (Ma and Clarke, 1993b), the depth of field function near the top surface can be measured by systematically moving the plane of focus from a position above the top

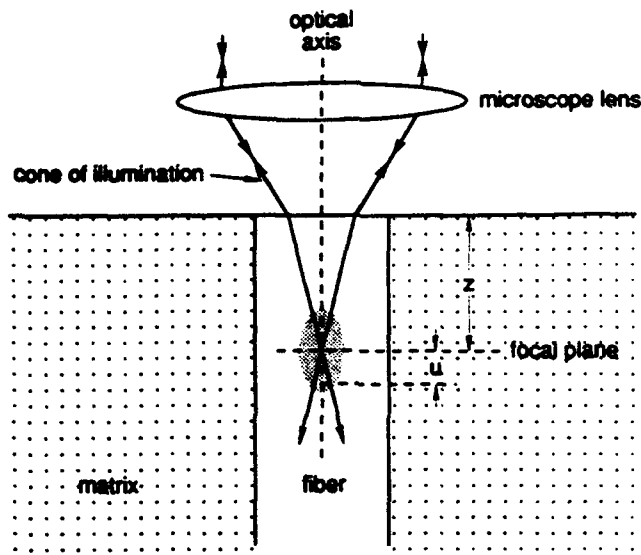


Figure 5: Schematic diagram of the optical arrangement used to collect fluorescence from a region in an embedded, transparent fiber below its surface. When the excitation laser is focused at a distance  $z$  below the top surface, only the signal generated in a small volume above and below the focal plane is effectively collected.

surface to a position below the surface while recording the fluorescence intensity  $I(z)$ . The depth of field function near the top surface is then:

$$g(z) = \frac{dI(z)}{dz} \quad (8)$$

For illustration, the depth of field function is plotted in figure 6 for our optical microscope using a 40/0.55 water immersion lens and a 50 $\mu\text{m}$  collection aperture.

Having established the depth of field function, the measured shifts can then be related to the true shift profile  $\Delta\nu(z)$  by:

$$\overline{\Delta\nu(z)} = \frac{\int_{-z}^{\infty} \Delta\nu(z+u) g(u) du}{\int_{-z}^{\infty} g(u) du} \quad (9)$$

In order to evaluate the deconvolution it was assumed that the true shift  $\Delta\nu(z)$  is a polynomial function of  $z$  but with unknown coefficients. By fitting the polynomial function convoluted with the depth of field function using equation 9 to the measured distribution, the values of the coefficients were obtained. The initially assumed function, with the coefficients obtained by fitting, is then regarded as the deconvoluted shift  $\Delta\nu(z)$ . The accuracy of this method has been previously demonstrated (Ma and Clarke, 1993b) and can be judged later in this paper by viewing figure 7, where the dashed curves are the true shift  $\Delta\nu$  (the solid curves) convoluted by the depth of field function. They have excellent fit with the measured data in general.

### 3.2 Shift and Stress Profiles Along Embedded Sapphire Fibers

Applying the depth profiling method, the residual stresses along a c-axis sapphire fiber embedded in a cubic zirconia matrix were measured. The diameter of the fiber is about 130 $\mu\text{m}$ . The

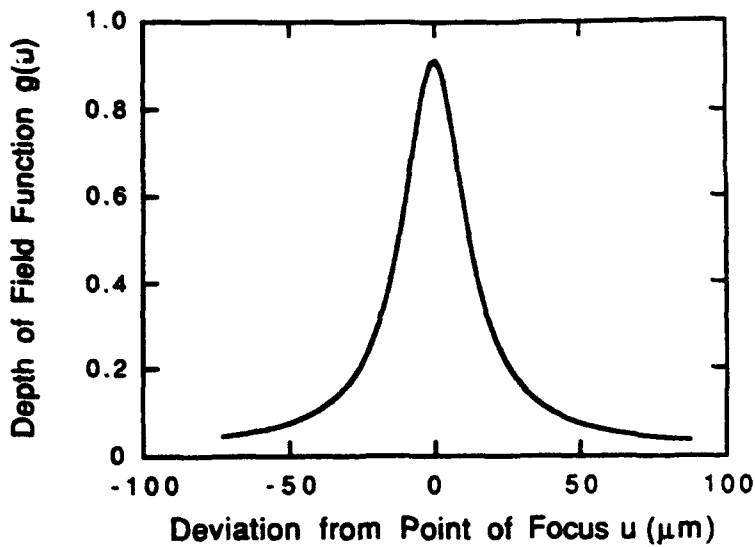


Figure 6: The depth of field function of the microprobe used. It describes the relative collection efficiency as a function of distance from the focal plane. Details are given in the text.

sapphire fiber was perpendicular to the composite top surface, which was polished to obtain an optical finish at the fiber end.

The measured and the deconvoluted frequency shift as a function of depth into a sapphire fiber, as well as the convoluted function are plotted in figure 7. Since cubic zirconia has thermal expansion coefficient larger than that of sapphire (Table I), the residual stress developed by thermal mismatch in the fiber should be compressive in both radial and axial directions. This is consistent with the large negative shifts observed when the probe is focused deep in the interior of the specimen.

Table I. Properties of Fiber and Matrix.

Property	Sapphire Fiber	$\text{ZrO}_2\text{-Al}_2\text{O}_3$ Matrix
$E$ (GPa)	434	220
$\alpha$ ( $10^{-6}/^\circ\text{C}$ )	8.3 (a), 9.0 (c)	11.0

The stress distributions calculated from the equations 6 and 7 are plotted in figure 8. The axial and the radial stresses approach constant values of 1180 and 440 MPa, respectively, toward the interior of the composite. The axial stress is close to zero near the top surface as force balance condition requires. We recognize that equations 6 and 7 are not strictly valid near the fiber end, so that the stress values derived are not reliable within distances to the surface comparable to the fiber diameter. This apparently gives rise to the small positive values for the axial stress near the surface. The radial stress also decreases its magnitude approaching the fiber end, due to the bending effect associated with the end.

It is interesting to compare the interior residual stress values obtained above with those calculated using elastic solutions. Since the sapphire fiber has relatively large thermal expansion anisotropy, exact expressions for the stresses are lengthy and not particularly informative. However, since the matrix is considerably more compliant than the fiber, Poisson's effect can

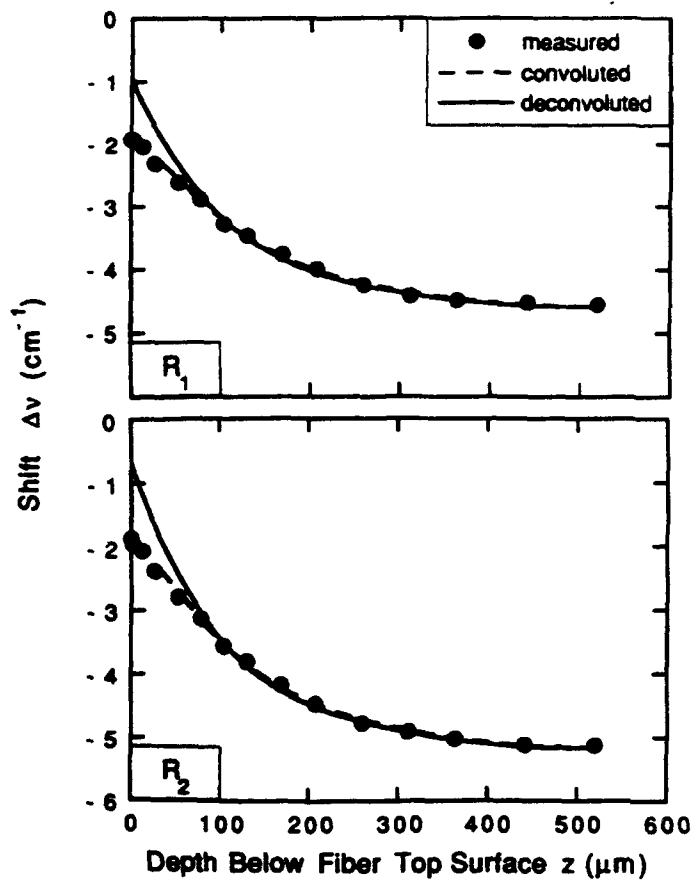


Figure 7: The line shift depth profiles for the (a)  $R_1$  and (b)  $R_2$  lines ( $z = 0$  at the surface) in a  $c$ -axis sapphire fiber embedded in a cubic zirconia matrix.

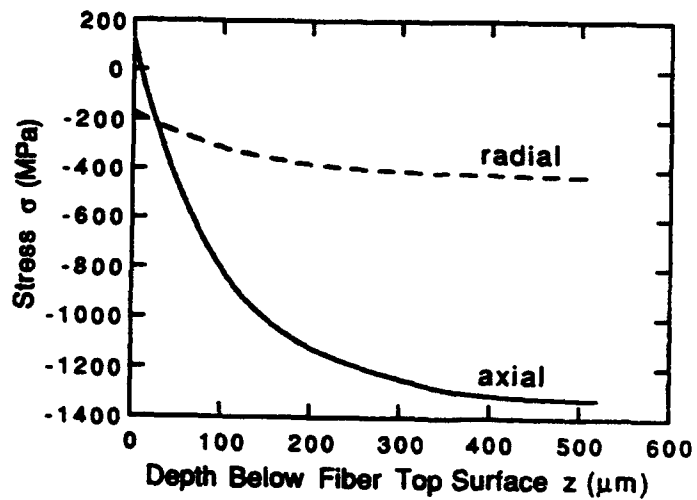


Figure 8: The radial and axial stresses as a function of depth along the sapphire fiber determined from the fluorescence data.

be neglected and the following relations are obtained:

$$\sigma_r = -E_f(\alpha_m - \alpha_e)\Delta T \frac{1}{1 + E_f/E_m} \quad (10)$$

$$\sigma_z = -E_f(\alpha_m - \alpha_e)\Delta T \quad (11)$$

Using the materials parameters listed in Table I, the effective temperature difference calculated using the radial and axial stresses are  $\Delta T_r = 1120^\circ\text{C}$  and  $\Delta T_z = 1360^\circ\text{C}$ . The difference between  $\Delta T_r$  and  $\Delta T_z$  indicates that the system did not behave elastically during the cooling period from the processing temperature. It is conceivable that the stress relaxation in the axial direction is less effective because the fiber can not slide over long distances, so that the temperature difference calculated from the axial stress is closer to the processing temperature of  $1500^\circ\text{C}$ .

#### 4 Concluding Remarks

The preceding analyses and experiments illustrate how the technique of fluorescence spectroscopy can be used to make measurements of commonly arising types of stresses in materials. This is possible, despite the fact that the fluorescence shift is a scalar quantity whereas the complete stress state is tensorial, because considerable simplification of the equations (equation 4) can be made in many practical situations. For instance, it was demonstrated (Ma and Clarke, 1993a, c, Ma et al., 1993c) that by taking advantage of the random orientation of polycrystalline ceramics, simplifications can often be made concerning both applied stresses and residual stresses. In other cases, stresses can be applied at prescribed orientations to the crystallographic axes of single crystals, where the symmetry of the stress field provides additional relationships between stress components and therefore enables determination of the stress tensor. This was illustrated in the case of residual stress in embedded fibers, where two independent stress components, the axial and radial stress were determined by two piezo-spectroscopic relations from R<sub>1</sub> and R<sub>2</sub> lines. This experiment also provides an excellent example of the advantage of an optical method. A single fiber can be easily located and inspected by optical microscope, and probed using piezo-spectroscopy. In addition, taking advantage of the fact that sapphire is transparent optically, it was able to measure stresses from the deep interior of the sample and therefore obtaining the true values of the residual stress in the bulk.

#### ACKNOWLEDGMENT

This work was supported by the Office of Naval Research under grant N00014-91-J-1875 (QM) and the DARPA URI program at UCSB under contract N00014-92-J-1808 (DRC). The authors are grateful to C. Hillman, UCSE, for providing the composite samples used in this work.

#### References

- Feher, E. and Sturge, M.D., 1968, "Effect of Stress on the Trigonal Splittings of d<sup>3</sup> Ions in Sapphire ( $\alpha$ -Al<sub>2</sub>O<sub>3</sub>)", Physical Review, 172, 244-249.  
Forman, R.A., Piermarini, G.J., Barnett, J.D. and Block, S., 1972, "Pressure Measurement Made by the Utilization of Ruby Sharp Line Luminescence", Science, 176, 284-285.  
Grabner, L, 1978, "Spectroscopic Technique for the Measurement of Residual Stress in Sintered Al<sub>2</sub>O<sub>3</sub>", Journal of Applied Physics, 49, 580-583.

- He, J. and Clarke, D.R., 1993, "Determination of Piezo-Spectroscopic Coefficients for Fluorescence from Chromium Doped Sapphire," in preparation.
- Kaplyanskii, A.A. and Przhevuskii, A.K., 1962, DAN SSSR, 142, 313 [Sov. Phys.-Dokl., 7, 37].
- Ma, Q. and Clarke, D.R., 1993a, "Stress Measurement in Single-Crystal and Polycrystalline Ceramics Using Their Optical Fluorescence", Journal of American Ceramic Society, 76, 1433-1440.
- Ma, Q. and Clarke, D.R., 1993b, "Measurement of Residual Stresses in Sapphire Fiber Composites Using Optical Fluorescence", Acta Metallurgica et Materialia, 41, 1817-1823.
- Ma, Q. and Clarke, D.R., 1993c, "Piezo-Spectroscopic Determination of Residual Stresses in Polycrystalline Alumina," submitted to Journal of American Ceramic Society.
- Ma, Q., Cao, H., Clarke, D.R. and Evans, A.G., 1993a, "Stress Redistribution around Cracks in a Fiber-Reinforced Aluminum Matrix Composite," in preparation.
- Ma, Q., Liang, L.C., Clarke, D.R. and Hutchinson, J.W., 1993b, "Mechanics of the Push-out Process from *in situ* Measurement of the Stress Distribution along Embedded Sapphire Fibers," in preparation.
- Ma, Q., Pompe, W., French, J.D. and Clarke, D.R., 1993c, "Residual Stresses in  $\text{Al}_2\text{O}_3\text{-ZrO}_2$  Composites: a Test of Stochastic Stress Models," submitted to Acta Metallurgica et Materialia.
- Nelson, D.F. and Sturge, M.D., 1965, "Relation between Absorption and Emission in the Region of the R lines of Ruby," Physical Review, 137, 1117-1130.
- Nye, J.F., 1967, "Physical Properties of Crystals," Oxford University Press, Oxford.
- Wunder, S.L. and Schoen, P.E., 1981, "Pressure Measurement at High Temperatures in the Diamond Anvil Cell", Journal of Applied Physics, 52, 3772-3775.